

Ultrasonic Flow Metering with Highly Accurate Jitter and Offset Compensation

vorgelegt von
Dipl.-Ing.
Assia Hamouda
geb. in Batna, Algerien

von der Fakultät IV
- Elektrotechnik und Informatik –
der Technischen Universität Berlin
zur Erlangung des akademischen Grades

Doktor der Ingenieurwissenschaften
- Dr.-Ing. -
genehmigte Dissertation

Promotionsausschuss

Vorsitzender: Prof. Dr.-Ing. Friedel Gerfers
1. Gutachter: Prof. Dr. rer. nat. Otto Manck
2. Gutachter: Prof. Dr.-Ing. Roland Thewes
3. Gutachter: Prof. Dr.-Ing. Nour-Eddine Bouguechal

Tag der wissenschaftlichen Aussprache: 12. Mai 2016

Berlin 2017

Acknowledgements

First and foremost, all thanks and praises are to God the Almighty for his blessing which made this work possible and allowed for it to be completed.

I would like to express my deepest and most sincere gratitude to my supervisor Prof. Dr. rer. nat. Otto Manck for his unconditional support, valuable and continuous advice, guidance and assistance throughout my Ph.D. program, and his very active part in initiating this work. I am especially thankful for his help with reviewing and his constructive comments and continuous support during the preparation of this thesis. Without his strong support and endless patience I would have never been able to complete this research work.

I would like to thank Prof. Nour-Eddine Bouguechal at the University of Batna, Algeria, for his kind support, helpful suggestions, and encouragement.

I would like to thank Prof. Roland Thewes, Head of the Institute of Sensor and Actuator Systems at TU-Berlin for reviewing my Ph.D. work. He has offered many helpful suggestions and remarks.

I am indebted to Mr. Helmut Manck, the Senior Manager of eonas GmbH, for funding this research and his commitment to support the development of this project.

I would like to acknowledge Dr. Ruediger Arnold, Boris Joesaar, Dr. Mohamed Lamine Hafiane and Redouane Djeghader with whom I had interesting conversations.

I also wish to thank Hadjer, Khadra, Souad, and Latifa for their great friendship and for helping me with various mathematical issues.

I would like to give special thanks to Dr. Peter Grametbauer and Dr. Sabine Seydel for proofreading my thesis and helpful suggests and comments.

I would like to give my special thanks to my family, my lovely mother, my father, my brother, my sisters, my mother in law, my brothers in law, and sisters in law. My warmest thanks go to my dearest husband for his encouragement and patient love that inspired me to complete this work and also to my little angel Zinedine.

Kurzfassung

Diese Dissertation schlägt eine neue Methode zur Messung des Wasserdurchflusses mit einem Durchlaufzeit-Ultraschall-Durchflussmessgerät vor. Die entwickelte Methode ermöglicht einem Ultraschall-Durchflussmesser eine genauere Erfassung von sehr niedrigen Durchflussraten. Flüsse von weniger als zwei Liter pro Stunde (2 l/h) in einem typische Haushaltswasserzähler sind möglich. Der Fluss einer gegebenen Flüssigkeit in einem Rohr wird durch die Laufzeitdifferenzmessung von Ultraschallsignalen mit und gegen den Fluss ermittelt. Je geringer der Durchfluss ist, desto kleiner ist die Laufzeitdifferenz. Die Differenz liegt bei niedrigen Durchflussraten im Bereich von wenigen Pikosekunden. Die vorgeschlagene Methode erlaubt das Messen der Differenz im Bereich von wenigen Pikosekunden und überwindet technische Schwierigkeiten anderer Messmethoden.

Die piezoelektrischen Wandler sind die kritischen Komponenten des Ultraschall-Durchflussmessers. Sie können die Genauigkeit der Ultraschall-Durchflussmesser erheblich beeinträchtigen. Die Wahl einer geeigneten analytischen Funktion für die Beschreibung des Verhaltens des piezoelektrischen Wandlers (Transducers) ist notwendig zur Ermittlung eines geeigneten Durchflussmessverfahrens, welches in der Lage ist, genaue und robuste Messergebnisse zu liefern. Im Ersatzschaltbild wird ein Transducer durch einen Oszillator mit parallel geschalteter Kapazität dargestellt. Die einfachste analytische Lösung der entsprechenden Differentialgleichung ergibt sich, wenn der Transducer mit einer Sinusfunktion angeregt wird. Im ersten Moment reagiert der Transducer mit einer Schwingung bei seiner eigenen Resonanzfrequenz, die aber nach einiger Zeit abklingt. Danach schwingt der Transducer nur noch mit der aufgezwungenen Frequenz. Wartet man also lange genug, dann wird der transiente Teil abklingen und man wird den stationären Zustand erreichen, wo der Transducer nur noch mit der Zwangsfrequenz schwingt.

Das vorgeschlagene Verfahren beruht darauf, die Differenz der Laufzeiten indirekt zu messen, indem die Phasendifferenz zwischen den stationären Teilen der empfangenen Signale in der stromaufwärtigen und der stromabwärtigen Richtung berechnet wird und indem eine Sinus-Fitting-Technik mit kleinstem quadratischen Fehler verwendet wird. Dies verringert den Effekt des Jitters in der Laufzeit. Der Jitter begrenzt die Messgenauigkeit bei sehr geringer Strömungsgeschwindigkeit.

Der letzte Teil der Arbeit untersucht das Offset-Verhalten. Der Offset ist die Abweichung der Differenz der Laufzeiten von Null bei nicht-fließendem Wasser. Er ist u. a. temperaturabhängig. Auch einige Parameter der Transducer sind temperaturabhängig, in erster Linie die Resonanzfrequenz selbst. Bei einer Erwärmung von 20°C auf 80°C verändert sich der Offset entsprechend und z.B. erreicht Werte um 300 ps, wenn er vorher bei 20°C auf „Null“ abgeglichen wurde. Die Messanordnung erlaubt eine neue, bisher in der Literatur nicht bekannte Art des Offset-Abgleichs durch Anpassung der Zwangsfrequenzen bezogen auf die Temperatur des Mediums. Die Langzeitstabilität der zur Einstellung der Offssetdrift verwendeten Zwangsfrequenz wurde bei verschiedenen Temperaturen experimentell nachgewiesen.

Die erhaltenen Messergebnisse verdeutlichen die Genauigkeit und Robustheit des vorgeschlagenen Verfahrens: die Differenz der Laufzeiten zeigt im Temperaturbereich von 20°C bis 80°C bei nicht-fließendem Wasser einem Peak-to-Peak-Jitter von nur 15 ps und einen Offset von weniger als 5 ps. Dadurch kann man im Vergleich zu früheren Techniken kleinere Durchflüsse messen.

Diese Arbeit liefert Ansätze für mögliche zukünftige Ultraschall-Durchflussmesser mit hoher Genauigkeit. Um die Ansätze kommerziell gut in zukünftigen Durchflussmessern nutzen können, bedarf es einer Integration der Messtechnik in einem integrierten Schaltkreis.

Abstract

This thesis proposes a new method for measuring water flow with a transit time ultrasonic flow meter device. The developed method allows the ultrasonic flow meter to reach a better performance than currently available commercial flow meters by accurately detecting very low flow rates of less than two liters per hour (2 l/h) in a typical household water meter. In principle, the flow velocity of a given liquid is obtained by measuring the transit times of an ultrasonic signal in the upstream and downstream directions. The difference between the transit times is directly proportional to the flow velocity. However, the fainter the flow is, the smaller the transit time difference (TTD) is. This difference can be as low as a few picoseconds, which gives rise to many technical difficulties in measuring such a small time difference with a given accuracy.

The piezoelectric transducers are critical components in ultrasonic flow meters since they can significantly affect the accuracy of the ultrasonic flow meters. Choosing an appropriate analytic function that describes the behavior of the basic part of a piezoelectric transducer proved to be essential for defining a suitable flow measurement method that yields accurate and robust measurement results. The electrical equivalent circuit of a transducer is represented by an oscillator connected to a parallel capacitance. The simplest analytical solution of the corresponding differential equation is obtained when the transducer is excited by a sinus function. First, the transducer oscillates at its own resonant frequency, and its oscillations die away after some time. If we wait long enough, the transient part dies out and what is left is the steady-state part, where the transducer oscillates at the forced frequency. The proposed method relies on measuring the TTD indirectly by computing the phase difference between the steady-state parts of the received signals in the upstream and downstream directions and by using the least squares sine-fitting technique. This reduces the effect of the TTD-jitter of the measurement, which limits the measurement accuracy at very low flow velocity.

The last part of the work addresses the issue of the TTD-offset, which refers to any deviation of the TTD from zero at no-flow conditions. The behavior of the TTD-offset is investigated over a temperature range. Some parameters of the transducer, such as resonance frequency, are temperature-dependent. When the temperature of the medium around the transducers increases by 80°C from ambient temperature, the TTD-offset (adjusted to zero at ambient temperature) changes accordingly and reaches approximately 300 ps. The novel proposed approach allows the compensation of the TTD-offset by adjusting the forced frequency with respect to the temperature of the medium. The long-term stability of the driving frequency used to adjust the TTD-offset drift has been experimentally proved at different temperatures. The obtained measurement results illustrate the accuracy and robustness of the proposed method since the TTD is measured at no-flow conditions, with a peak-to-peak TTD-jitter as low as 15 ps and the TTD-offset less than 5 ps within a temperature range from ambient temperature to 80°C. This allows to reach a smaller minimum detectable flow in comparison to previously developed techniques.

This work offers some suggestions to design an ultrasonic flow meter with high accuracy in the future. However, the commercial aspect of the future flow meter requires an integration of the proposed measurement technique in an integrated circuit.

Abbreviations and Symbols

Abbreviations

<i>ADC</i>	Analog-to-Digital Converter
<i>CSV</i>	Comma-separated values
<i>LSSF</i>	Least Squares Sine-Fitting
<i>OPAMP</i>	Operational Amplifier
<i>SNR</i>	Signal-to-Noise Ratio
<i>STD</i>	Standard Deviation
<i>TR</i>	Transducer
<i>TTD-offset</i>	Transit Time Difference-offset
<i>TTD-jitter</i>	Transit Time Difference-jitter

Symbols

<i>A</i>	Pipe cross section [m^2]
<i>c</i>	Speed of sound [m s^{-1}]
<i>C</i>	Spring compliance [m N^{-1}]
<i>C_s</i>	Serial capacitance [F]
<i>C_p</i>	Parallel capacitance [F]
<i>d</i>	Viscous damping coefficient [N s m^{-1}]
<i>D</i>	Pipe inner diameter [m]
<i>DR</i>	ADC dynamic range [dB]
<i>f_p</i>	Parallel frequency [Hz]
<i>f_s</i>	Serial frequency [Hz]
<i>f_r</i>	Resonance frequency [Hz]
<i>f_{dr}</i>	Driving frequency [Hz]
<i>f_f</i>	Forced frequency [Hz]
<i>F₀</i>	Applied force [N]
<i>I</i>	Current [A]
<i>k</i>	Stiffness coefficient [N m^{-1}]
<i>K</i>	Water compressibility [$\text{m}^2 \text{N}^{-1}$]
<i>L</i>	Transducer separation [m]
<i>L_s</i>	Serial inductance [H]
<i>m</i>	Mass [Kg]

N	Sample size
N_{bit}	ADC resolution [bits]
Q	Flow rate [$\text{m}^3 \text{s}^{-1}$]
q	Charge [C]
$qh(t)$	Homogeneous solution [C]
$qp(t)$	Particular solution [C]
R_s	Serial resistance [Ω]
R	Pipe Radius [m]
t_{up}	Upstream traveling time (against the flow) [s]
t_{down}	Downstream traveling time (with the flow) [s]
T	Disk thickness [m]
TTD	Transit time difference [s]
$Temp$	Temperature [$^{\circ}\text{C}$]
v	Flow velocity [m s^{-1}]
v_{min}	Minimum flow velocity [m s^{-1}]
V	Voltage [V]
V_{FRS}	Full scale voltage range [V]
V_{LSB}	Least significant bit [V]
$VRD1$	First direction receiver voltage [V]
$VRD2$	Second direction receiver voltage [V]
$VTD1$	First direction transmitter voltage [V]
$VTD2$	Second direction transmitter voltage [V]
x	Displacement [m]
ρ	Water density [Kg m^{-3}]
ϕ_{up}	Upstream phase [rad]
ϕ_{down}	Downstream phase [rad]
σ	Standard deviation of the transit time difference [s]
$\sigma_{\bar{x}}$	Standard deviation error of the transit time difference [s]
ζ	Damping coefficient
ω_f	Angular forced frequency [rad s^{-1}]
ω_r	Angular resonance frequency [rad s^{-1}]

Content

Chapter 1: Introduction	1
1.1. Motivation	1
1.2. State of the Art	2
1.3. Main Work Objective	3
1.4. Thesis Outline	3
Chapter 2: The Principles of Ultrasonic Flow Meter	5
2.1. Introduction	5
2.2. Doppler Flow Meter	5
2.3. Transit Time Flow Meter	6
2.3.1. Transit Time Flow Meter Configuration	6
2.3.2. The Principle of Transit Time Flow Meter	8
Chapter 3: Ultrasonic Piezoelectric Transducer Theory and Modeling.....	10
3.1. Introduction	10
3.2. Piezoelectric Effect	10
3.3. Ultrasonic Piezoelectric Transducer.....	11
3.3.1. Piezoelectric Disk.....	12
3.3.2. Piezoelectric Backing and Matching Layer.....	13
3.4. Piezoelectric Transducer Modeling.....	13
3.5. Butterworth-Van Dyke Model.....	18
3.6. Transmitted and Received Signals Modeling.....	24
3.6.1. Transmitter.....	26
3.6.2. Receiver.....	27
3.7. Quiet Region Aspect	29
3.8. Characteristic Frequencies of Piezoelectric Transducer	32

Chapter 4: Determination of the Transit Time Difference (TTD)	33
4.1. Introduction	33
4.2. Experimental Setup for Measuring the TTD.....	34
4.3. Methodology for the Calculation of TTD	36
4.4. Least Squares Sine-Fitting	37
4.5. Estimation of the Quiet Region	38
4.6. Algorithm for Computing the TTD	40
Chapter 5: TTD-jitter Reduction	42
5.1. Introduction	42
5.2. The Effect of the Sampling Jitter on TTD.....	43
5.3. Sources of TTD-jitter	44
5.4. TTD-jitter Reduction Technique	45
Chapter 6: TTD-Offset Cancellation	50
6.1. Introduction	50
6.2. Sources of TTD-offset.....	50
6.3. The Impacts of Temperature on the Transducer Resonance Frequencies	51
6.4. Zero Flow TTD-offset Correction.....	53
6.5. Temperature Dependence of the TTD-offset Calibration.....	57
Chapter 7: Results and Analyses	60
7.1. Introduction	60
7.2. Hardware Design.....	61
7.3. Software Algorithm.....	62
7.3.1. Transmission of the Sinusoidal Burst	63
7.3.2. Digitizing of the Two Direction Signals.....	63
7.3.3. TTD-offset Cancellation Algorithm	64
7.4. TTD-offset Compensation Evaluation	66
7.5. The Effect of Temperature on TTD-offset Measurements	68
7.6. Discussion	70
Chapter 8: Conclusion	72

Chapter 1

Introduction

1.1. Motivation

Flow measurement is often critical in the household sector of the domestic economy [1]. Therefore, in order to make a profit rather than run at a loss, it is imperative to accurately measure what flows through the measuring pipe under all circumstances.

Ultrasonic flow meters have been used successfully in industrial applications for several decades [2-3]. They have gained approbation in wide metering applications such as dirty or clean water, petrochemical products, natural gas, and so on. This is due to the significant operational and economic advantages that the ultrasonic flow meters offer in contrast to conventional meters. From the economic point of view, they are easy to install, inexpensive, and require less maintenance than other meters such as mechanical flow meters, which need to be checked periodically [2]. In terms of operation, ultrasonic flow meters can be highly sensitive and accurate, and they typically have a broader flow rate range, good measurement repeatability, and bi-directional flow capability.

As any other measurement technology, ultrasonic flow meters have their measuring limitations, which are mostly caused by changes in the temperature of the medium and several other factors, such as water viscosity and compressibility [4-7]. If there is no flow in the measuring pipe (i. e., still water in the pipe), the upstream and downstream transit times of such meters are equal and the difference between the two transit times should be negligible. However, this may not always be the case since the transit time difference (TTD) can be influenced by jitter and offset. Therefore, any delay offset between the upstream and downstream transit times directly translates into a zero flow error. This zero flow TTD-offset limits measurement accuracy at low flow velocities. The lower this error, the higher the accuracy of the flow meter.

1.2. State of the Art

Following [7], the accuracy of the ultrasonic flow meter at no-flow conditions - for water or gas applications - depends essentially on the reciprocity of the electro-acoustic measurement system. This reciprocity can be achieved by perfect transducer symmetry or perfect electrical symmetry in the ultrasonic flow meter system. This means that either the impedances of the electric loads for both transmitting and receiving transducers are equal or both transducers are identical. The electro-acoustical reciprocity principle as referenced by Per Lunde's paper [8-16] provides possibilities for reducing or even neglecting the need for the zero flow calibration of ultrasonic flow meters for both liquid and gas applications.

In 2010, Borg Johan presented in his Ph.D. thesis "On electronics for measurement systems" [17-18] a new methodology based on driving the transducer with a current source rather than a voltage source in order to achieve good impedance matching between transmitting and receiving circuits. This method achieved a significant improvement in reducing the zero flow error compared to Lunde's work.

What followed was the state-of-the-art publication of Yang Bo in March 2011 [19], when he presented a new approach to improve the accuracy and the stability of ultrasonic transducer flow metering over a wide temperature range under non-reciprocal operation conditions. This approach is based on driving both transducers at a specific frequency outside their resonance frequencies through a sinus burst in order to eliminate the effect of temperature dependence of the resonance frequency and therefore reduce the long-term drift of the transit time difference measurements, which is caused by temperature variations. The drawbacks of this method are, on the one hand, the reduced signal-to-noise ratio (SNR) caused by working outside the resonance frequency of the transducer and, on the other hand, the fact that the excitation voltage level must be high even in the presence of an amplifier. This results in a high power consumption of the whole measurement system which presents a big disadvantage in battery applications. Nevertheless, this approach achieved improved results compared with the two previously mentioned methods.

1.3. Main Work Objectives

The main objective of this work is to develop a new methodology, which combines hardware with appropriate digital evaluation software algorithms and which can overcome the effect of the TTD-jitter noise and the TTD-offset drift. This methodology reduces the false flow detection and improves the accuracy of the ultrasonic flow meter at low and no-flow conditions. The first part of this research work focuses on the analytical modeling or the mathematical presentation of the piezoelectric transducer, which is based on the driven damped harmonic oscillator system. This model provides a better understanding of the behavior of the piezoelectric transducer and provides the necessary concepts that allow to measure the TTD very accurately.

The main contribution of this work is summarized by the two main steps that were undertaken to minimize the effect of zero flow error and TTD-jitter on the measurement results:

- Develop a software algorithm on the basis of the proposed approach, which would be capable to effectively reduce the TTD-jitter.
- Develop another software algorithm on the basis of the proposed approach, which would be capable to continuously correct the zero flow TTD-offset.

1.4. Thesis Outline

A significant amount of the current research focuses on ultrasonic flow meters, especially in the field of measuring of flow rate in the transmission of gas through pipelines, in order to develop more accurate measurement methodologies. We will elaborate and refer to the appropriate theoretical background when describing our experiments. This dissertation is organized as follows:

1. Chapter 1 outlines the motivation behind this work and positions our work amongst the recent research efforts in ultrasonic flow meter measurement methodologies currently available.
2. Chapter 2 describes the available ultrasonic flow meters used for measuring the flow rate of a flowing fluid.

-
3. Chapter 3 presents the theoretical background of a piezoelectric transducer. We address the relevant theories to derive an analytic model of the transducer that can describe its behavior in both cases, transmitter and receiver.
 4. Taking into account the analytic transducer model and all the aspects derived through the mathematical representation of the transducer presented in Chapter 3, Chapter 4 presents the analysis and evaluation of our proposed method can be used to calculate the transit time difference. It also presents a detailed description of each of the measurement setup system's blocks.
 5. Chapter 5 describes the applied TTD-jitter analysis and methodology used to understand the causes of TTD-jitter. The proposed TTD-jitter reduction technique is also described.
 6. The zero flow TTD-offset correction technique is the main subject of Chapter 6, starting with a study of the TTD-offset sources and ending with the proposed approach to mitigate this TTD-offset.
 7. In Chapter 7, the experimental results are presented and analyzed.
 8. Finally, conclusions are drawn in Chapter 8.

Chapter 2

The Principles of Ultrasonic Flow Meter

2.1. Introduction

Most ultrasonic flow meters use one of the two main principles: Doppler effect or Transit Time Difference. When a fluid is in motion with a certain velocity, the flow meter measures the flow of this fluid either by calculating the difference between the two traveling times of an ultrasonic signal propagating with and against the flow direction or by measuring the frequency shift using the Doppler principle.

2.2. Doppler Flow Meter

This type of flow meter is based on the Doppler principle discovered in 1842. Typically, one transducer is fitted in the pipe wall as shown in Figure 2.1. It continuously transmits an ultrasonic signal at a constant frequency f_1 into the flowing fluid. The particles inside the fluid reflect the transmitted signal, and their movement shifts the frequency of the ultrasonic signal to a frequency f_2 . The frequency shift is proportional to the speed v of the particles and hence to the flow. It is given by the following equation [20-22]:

$$\Delta f = f_2 - f_1 = \frac{2vf_1 \cos \theta}{c}, \quad (2.1)$$

where Δf is the frequency shift (the difference between transmitted and received frequencies), θ is the angle of the transmitter and receiver crystal axis with respect to the pipe axis, c is the sound velocity, and v is the flow velocity.

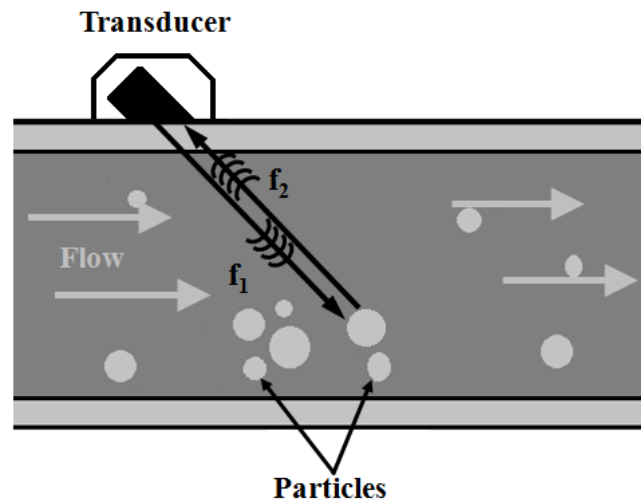


Fig. 2.1: Doppler flow meter

Due to many drawbacks and limitations of ultrasonic Doppler flow metering, this method is now used only in a few specific applications such as for waste water that contains dirt particles or gas bubbles. It has been replaced by the transit time ultrasonic flow metering because in addition to flow rate measurement this method can also provide information on the type of liquid and the working temperature on the basis of sound velocity measurement [20].

2.3. Transit Time Flow Meter

2.3.1. Transit Time Flow Meter Configuration

The ultrasonic transit time flow meter consists of one pair of transducers facing each other, which are separated by a known distance. The transducers are mounted according to different geometries depending on the application. For instance, the in-line configurations shown in Figures 2.2 and 2.3, as well as the configuration with reflectors shown in Figure 2.4, are most often used in applications where the diameter of the pipe is less than 25 mm, whereas the diagonal configuration shown in Figure 2.5 is used in applications where the diameter of the pipe is up to 10 meters [4].

Two flow meter pipes have been used in this work. The configuration of the first flow meter pipe contains one pair of 4 MHz ultrasonic transducers (Figure 2.2). The distance between the two transducers and the inner radius of the flow meter body are $L = 42.2$ mm and $R = 4$ mm, respectively. The configuration of the second flow meter pipe contains one pair of 1 MHz ultrasonic transducers with $L = 49.5$ mm (Figure 2.3). All experimental work has been performed using these meters.

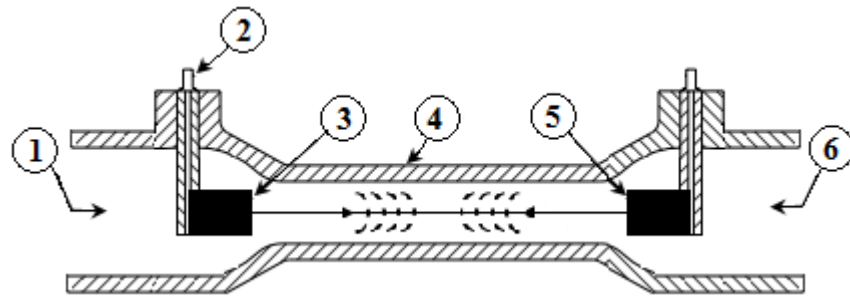


Fig. 2.2: Flow meter pipe with in-line transducers: (1) inlet, (2) cable connector, (3) the upstream transducer, (4) flow meter body, (5) the downstream transducer, (6) outlet

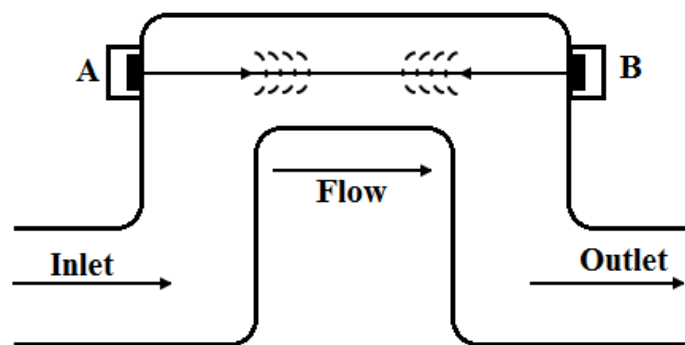


Fig. 2.3: Flow meter pipe with in-line transducers

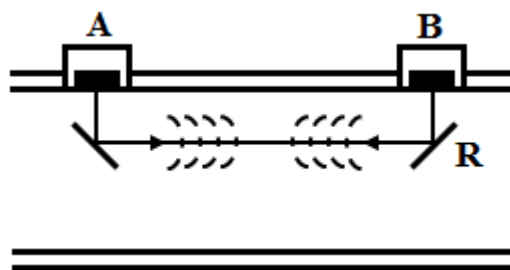


Fig. 2.4: Flow meter pipe with reflectors

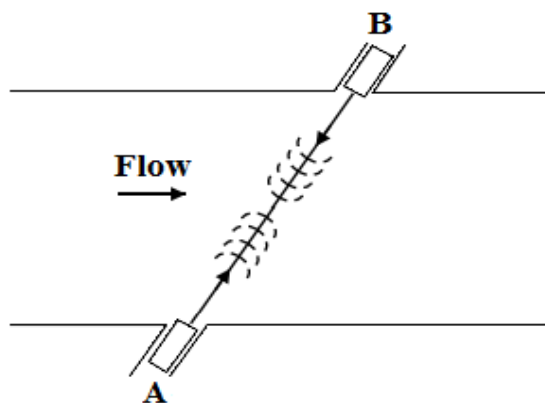


Fig. 2.5: Flow meter pipe with diagonal transducers

2.3.2. The Principle of Transit Time Flow Meter

The transit time flow meter is based on the transit time difference (TTD) principle and uses two transducers. Each transducer can alternately transmit and receive an ultrasonic signal. This signal is generated when a piezoelectric crystal is subjected to an alternating voltage. Conversely, the piezoelectric crystal generates voltage when the ultrasonic signal impacts the transducer. In the case of simultaneous excitation, the two transducers emit and receive the ultrasonic signals at the same time. One ultrasonic signal travels through the pipe in the direction of the flow (downstream direction) and the other against the flow (upstream direction). Every signal needs a certain period of time (called transit time) passes before the signal is received by the opposite transducer. This transit time depends on three parameters: the speed of sound c , the ultrasonic path length L , and the flow velocity v as illustrated by the following equations [23-24]:

$$t_{up} = \frac{L}{c-v}, \quad (2.2)$$

$$t_{down} = \frac{L}{c+v}, \quad (2.3)$$

where t_{up} is the upstream transit time, and t_{down} is the downstream transit time.

If there is no flow, then:

$$t_{up} = t_{down} = t_0 = \frac{L}{c}. \quad (2.4)$$

At no-flow conditions the transit times are equal. Once the fluid starts to flow, the sound wave moving with the flow travels faster than the sound wave moving against the flow. The difference between the two transit times is directly proportional to the flow velocity. This can be mathematically expressed as follows:

$$\Delta t = t_{up} - t_{down} = \frac{2vL}{c^2-v^2} \cong \frac{2vL}{c^2}. \quad (2.5)$$

Since flow velocity v is much smaller than the speed of sound c , it can be derived from (2.5) as follows:

$$v \cong \frac{c^2 \Delta t}{2L}. \quad (2.6)$$

Since the internal cross-section of the pipe is known, the volume flow rate Q is determined by the following formula:

$$Q = v \cdot A = v\pi R^2, \quad (2.7)$$

where A is the inner circular cross-section, and R is the inner radius of the flow meter pipe. The ratio of Δt to the traveling time t_0 measured at no-flow conditions is given by:

$$\frac{\Delta t}{t_0} = \frac{2v}{c}. \quad (2.8)$$

Equation (2.8) can be used to calculate the needed measurement accuracy. For instance, the minimum flow v_{\min} calculated for a given flow rate of two liters per hour (2 l/h) and pipe diameter of 0.8 cm is about $v_{\min} = 10$ mm/s, or approximately 7 ppm compared to the sound velocity (the speed of sound in pure water and room temperature is about $c = 1500$ m/s). Therefore, according to Equation (2.5), this minimum flow variation of 10 mm/s produces a transit time difference value of about $\Delta t = 380$ ps, provided that the travelling time of the used flow meter pipe is $28 \mu\text{s}$ (calculated for $L = 42.2$ mm using Equation (2.4)). Therefore, to achieve an accuracy of 5 %, the desired ultrasonic flow meter must be able to accurately measure the transit time difference of at least 20 ps (which then would be its minimum measured value).

This thesis focuses on the transit time flow meter mostly because of its extensive industrial usage [5]. Besides, it has the highest cost efficiency and, unlike the Doppler flow meter, does not require the fluid to contain particles or air bubbles in order to reflect the ultrasonic sound.

Chapter 3

Ultrasonic Piezoelectric Transducer Theory and Modeling

3.1. Introduction

An accurate description of the behavior of ultrasonic transducer's active element requires a detailed investigation of the transmitted acoustic wave, which travels through the pipe, and of the received acoustic wave, which is picked up by the opposite transducer after a predetermined time.

This chapter starts with an overview of the piezoelectric effect, which is followed by a description of the real transducer geometry and its different composite layers. Thereafter, an analytical approach of the piezoelectric transducer developed through the solution of the differential equation of driven damped harmonic oscillator, is analyzed in detail.

In the remainder of this chapter, the emulated transmitted and received waveforms, which are generated using Matlab, are compared to the real signals obtained experimentally. We show that a full agreement between the theoretical description and experimental signals can be achieved with an appropriate choice of only three model parameters: resonance frequency, damping factor, and excitation frequency.

3.2. Piezoelectric Effect

The word "piezo", of Greek origin, means "push". According to [25], the effect known as piezoelectricity is a property exhibited by certain classes of crystalline materials that consist of polarized molecules. It was discovered by the brothers Pierre and Jacques Curie in 1880. When a piezoelectric material is subjected to a mechanical stress, it generates an electrical charge, which is proportional to the applied stress. This behavior is called the direct piezoelectric effect. Inversely, when the piezoelectric material is subjected to an

electric field, it changes dimension and becomes strained [25]. This strain is again proportional to the applied field. These two effects are shown in Figure 3.1.

Besides quartz and Rochelle salts, many other piezoelectric materials are available nowadays, such as Barium Titanate (BaTiO_3), Lead Metaniobate (PbNb_2O_3) and Lead Zirconate Titanate (PZT) [26-27].

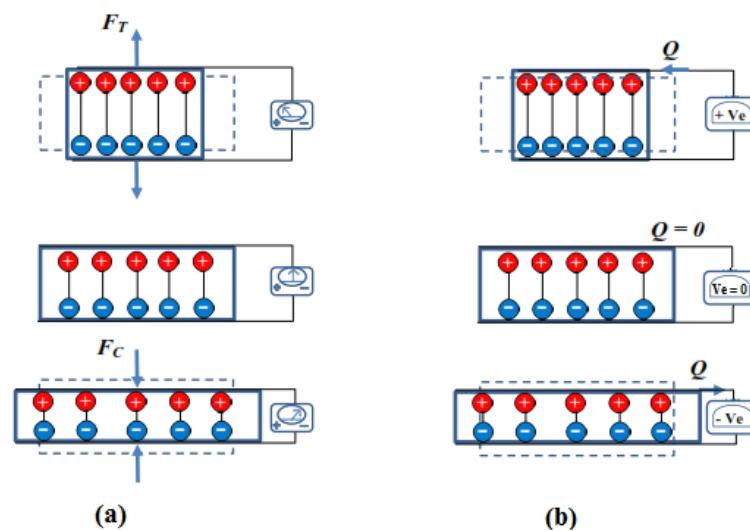


Fig. 3.1: Piezoelectric effects: (a) direct, (b) inverse [25]

3.3. Ultrasonic Piezoelectric Transducer

The ultrasonic piezoelectric transducer is employed to convert electrical energy into mechanical energy (sound wave) and vice versa. The piezoelectric material has the following three properties [25]:

- the elasticity property which defines the mechanical aspect of the material
- the piezoelectric property which defines the electromechanical aspect of the material
- the dielectric property which defines the electrical aspect of the material.

An ultrasonic transducer consists of three main parts as shown in Figure 3.2: piezoelectric disk, the rear part or backing layer, and front or matching layer [28-29]. Many factors determine the performance of ultrasonic transducers, the most important of them being the material properties of the transducer components, including housing and connections, the external mechanical, and electrical load conditions and damping.

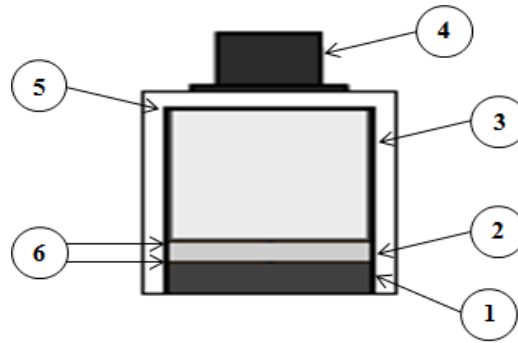


Fig. 3.2: Typical construction of an ultrasonic transducer [29]:
(1) matching layer, (2) piezoelectric disk, (3) backing layer,
(4) cable connector, (5) transducer housing, (6) electrodes

3.3.1. Piezoelectric Disk

The piezoelectric disk is the main component for generating and receiving the ultrasonic wave and the active element of the ultrasonic transducer. The angle at which the piezoelectric crystal is cut in relation to its crystallographic axes defines its vibration mode and the type of the generated ultrasonic wave, which can be a longitudinal or a shear wave (Figure 3.3), depending on the application. For instance, in our application, the ultrasonic wave propagates through the water by a longitudinal motion (compression/expansion) as the fluid does not support the shear motion [30]. The surface of the disk moves up and down, and the water has to follow this movement directly.

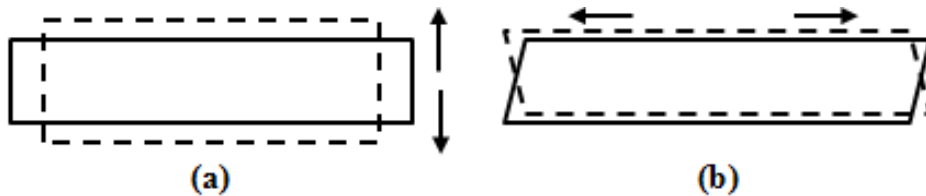


Fig. 3.3: Response of a piezoelectric element to an AC voltage:
(a) compression motion generating longitudinal waves,
(b) transverse motion generating shear waves

The active element of the transducer shows a typical resonance frequency whose value is precisely related to the size and shape of the piezoelectric transducer according to Equation (3.1).

$$f_r = \frac{c}{2T}, \quad (3.1)$$

where f_r is the resonance frequency, T is the disk thickness (see Figure 3.4), and c represents the wave velocity of the longitudinal vibration inside the disk and depends on the acoustic properties of the disk.

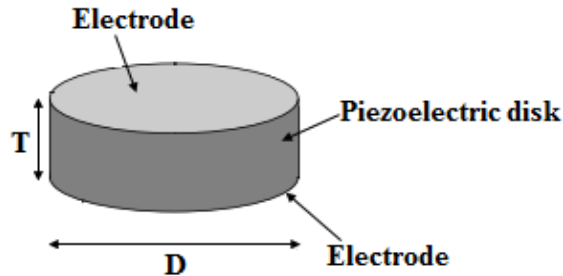


Fig. 3.4: Piezoelectric disk with thickness T and diameter D [29]

3.3.2. Piezoelectric Backing and Matching Layer

The backing layer consists of a high-density material and is used to control the vibration by absorbing the energy radiating from the back face of the active element. The piezoelectric materials are characterized by high acoustic impedance in comparison to water and air. Consequently, the bandwidth of the response function of the disk is low. The acoustic impedance mismatch can be overcome by adding a matching layer to enhance the bandwidth and source sensitivity. More reliable wide bandwidth transducers are obtained by adding a quarter-wave matching layer [31-33].

3.4. Piezoelectric Transducer Modeling

The transducer may be driven by a voltage burst consisting of a finite number of sinus cycles with a well-defined frequency, which is chosen near the resonance frequency of the transducer. Vibrating at the same frequency as the applied voltage, the piezoelectric material generates a wave, which propagates through the water. In order to understand exactly how this waveform is generated, in particular the "transient behavior" and "steady-state behavior", an analytical description is needed to emulate the excitation process.

The transducer, like many oscillators, can be modeled as a harmonic oscillator, which is characterized by its "resonance frequency" and "damping coefficient". The excitation of the harmonic oscillator by a voltage causes the oscillator to vibrate at the same frequency as the applied voltage. It vibrates with greater amplitude if the frequency of the excited voltage corresponds to the resonance frequency of the oscillator.

In the case of a harmonic excitation, three basic parameters dominate the behavior of the oscillator's response: angular resonance frequency ω_r , damping coefficient ζ , and angular forced frequency ω_f . However, as the free vibration (transient part) dies out over time, only the forced frequency dominates the remaining steady-state part. When there is no exciting signal, the signal dies out gradually, which causes the decay of the signal to zero due to the transfer of the energy to the water. This switching-off behavior is characterized only by ω_r , ζ .

The driven damped harmonic oscillator model attempts to develop a better understanding of the ultrasonic transducer. The disk, which represents the transducer's active element, can be described by both models depicted in Figure 3.5. During resonance, the series resonant circuit R_s , L_s , C_s shown in Figure 3.5.b (also called motional branch) forms a damped harmonic oscillation and resonates in a similar way to the mechanical model shown in Figure 3.5.a. Therefore, it is possible to compare the two models and use the electrical parameters (inductance, capacitance, and resistance) to represent the mechanical parameters (mass, stiffness, and damping) [25]. Hence, some mechanical and electrical properties such as material density, elastic mechanical parameters, piezoelectricity, and dielectricity define the values of the motional components. The impact of the parallel capacitance shown in the electrical model is explained in more detail in the next section.

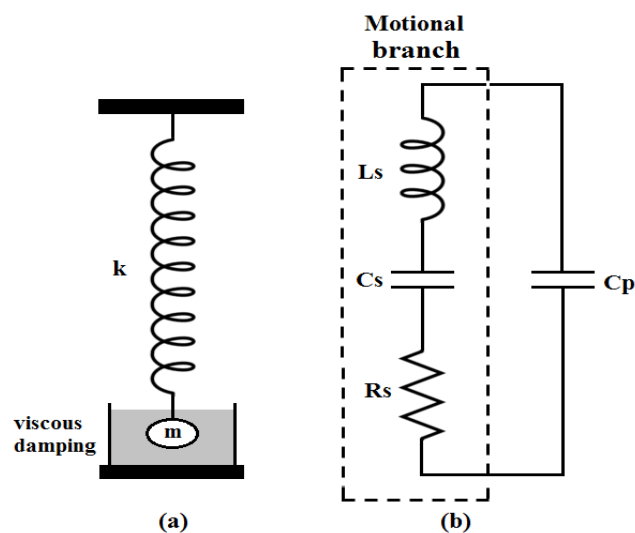


Fig. 3.5: Equivalent models of the piezoelectric element:
(a) mechanical model, (b) Butterworth-Van Dyke electrical model

For sinus excitation, the basic description of the damped externally driven oscillator is provided by the following second order differential harmonic equation:

$$\frac{d^2x(t)}{dt^2} + 2\zeta\omega_r \frac{dx(t)}{dt} + \omega_r^2 x(t) = F \sin(\omega_f t), \quad (3.2)$$

where:

$F = F_0/m$ is the applied external force F_0 divided by m ,

m is the mass,

ω_f is the angular forced frequency of the sinus burst,

d is the viscous damping coefficient,

k is the system stiffness coefficient,

$\zeta = \frac{d}{2\sqrt{km}}$ is the damping coefficient, and

$\omega_r = \sqrt{\frac{k}{m}}$ is the angular transducer resonance frequency.

The mechanical displacement is analogous to the electrical charge that can be used to reformulate the previous differential Equation (3.2). The summary of the equivalent quantities between the mechanical and electrical models is presented in Table 3.1 [34].

<i>Electrical</i>	<i>Mechanical</i>
Charge Q	Displacement x
Current $I = dQ/dt$	Velocity v
Applied voltage V	Applied force F_0
Resistance R_s	Friction c
Inductance L_s	Mass m
Capacitance C_s	Spring compliance $C = 1/k$

Table 3.1: Comparison of equivalent electrical and mechanical resonant circuits

According to Table 3.1, Equation (3.2) of the mechanical motion can be rewritten as:

$$\frac{d^2Q(t)}{dt^2} + 2\zeta\omega_r \frac{dQ(t)}{dt} + \omega_r^2 Q(t) = \frac{V}{L_s} \sin(\omega_f t), \quad (3.3)$$

where:

V is the amplitude of the applied voltage,

R_s , L_s , and C_s are the parameters of the piezoelectric disk,

$\zeta = \frac{R_s}{2} \sqrt{\frac{C_s}{L_s}}$ describes the damping coefficient, and

$\omega_r = \frac{1}{\sqrt{L_s C_s}}$ is the transducer serial resonance angular frequency.

Assuming $\zeta < 1$ (underdamped harmonic oscillator), the complete solution of Equation (3.3) is given by Equation (3.4). Generally, this function can be divided into two parts: the solution of the homogeneous differential equation with a zero right side giving the transient response, and the particular solution of the non-homogeneous equation as the answer to the externally applied voltage:

$$Q(t) = Q_h(t) + Q_p(t). \quad (3.4)$$

The homogeneous solution of this equation is given by:

$$Q_h(t) = A_h e^{-\zeta \omega_r t} \sin(\omega_d t + \theta), \quad (3.5)$$

where ω_d is the damped natural angular frequency, equal to $\omega_d = \omega_r \sqrt{1 - \zeta^2}$, and the constants A_h and θ are dependent on the initial conditions.

The particular solution, the forced or stationary solution, is given by:

$$Q_p(t) = A_p \cos(\omega_f t - \emptyset). \quad (3.6)$$

A_p and \emptyset can be determined simply if we use the complex form of the differential Equation (3.3), which can be written as:

$$\frac{d^2 Q(t)}{dt^2} + 2\zeta \omega_r \frac{dQ(t)}{dt} + \omega_r^2 Q(t) = \frac{V}{L_s} e^{i\omega_f t}. \quad (3.7)$$

Using Moivre's formula, and $Q(t) = A_p e^{i(\omega_f t - \emptyset)}$, one can write:

$$(\omega_r^2 - \omega_f^2) A_p + 2i\zeta \omega_r \omega_f A_p = \frac{V}{L_s} (\cos \emptyset + i \sin \emptyset). \quad (3.8)$$

By dividing the previous equation into real and imaginary parts, we end up with the following equations that correspond to the amplitude A_p and the phase \emptyset , respectively:

$$A_p = \frac{V}{L_s \sqrt{(\omega_r^2 - \omega_f^2)^2 + (2\zeta \omega_r \omega_f)^2}}, \quad (3.9)$$

$$\emptyset = \tan^{-1} \frac{2\zeta \omega_r \omega_f}{\omega_r^2 - \omega_f^2}. \quad (3.10)$$

The amplitude of the forced oscillations depends on the difference between the forced frequency¹ of the applied voltage and the resonance frequency of the piezoelectric disk. The damping coefficient has a strong influence on the maximum amplitude reached when both forced and resonance frequencies are similar. Figures 3.6 and 3.7 show the typical behavior of the amplitude and the phase, respectively, when realistic parameters are applied.

Regarding the amplitude response shown in Figure 3.6, a Gaussian type distribution around the resonance point can be observed when realistic parameters are applied, especially for the damping coefficient. Considering the main goal of this work, which is reducing the TTD-jitter and TTD-offset, this illustration clearly demonstrates the strategy which has to be applied: If both transducers are driven using a forced frequency, which is in the direct vicinity of their resonance points, good SNR in the receiving part can be expected. In this work, the recommended range is ± 500 kHz or approximately 10% of the resonance frequency.

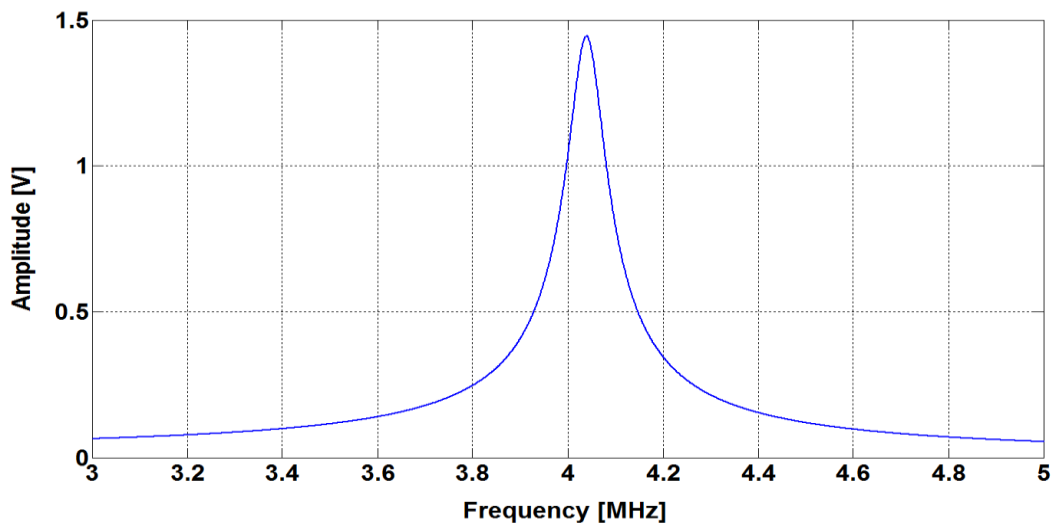


Fig. 3.6: Amplitude of a driven damped harmonic oscillator at $\zeta = 0.02$ and $f_r = 4.05$ MHz

Regarding the phase response shown in Figure 3.7, it can be observed that the phase shift between the excitation and the mechanical response of the transducer is constant and depends only on the difference " $\omega_r - \omega_f$ ". It can be also observed in Figure 3.7 that the phase tends either towards 0° or towards 180° at frequencies away from the resonance frequency. This feature would allow to derive a reliable measurement method because in

¹ Also called the driving frequency.

these two parts of the phase frequency response the phase shifts are quite steady and no longer depend on the transducer parameters. From this observation it can be directly deduced that the temperature dependence of the transducer parameters effects does not influence the measurements (outside the well-known relationship of the speed of sound versus temperature). Yang Bo [19], who applied this idea, reported an approximately 200 ps peak-to-peak TTD-jitter and -185.3 ps TTD-offset measured at no-flow conditions due to drastically reduced SNR.

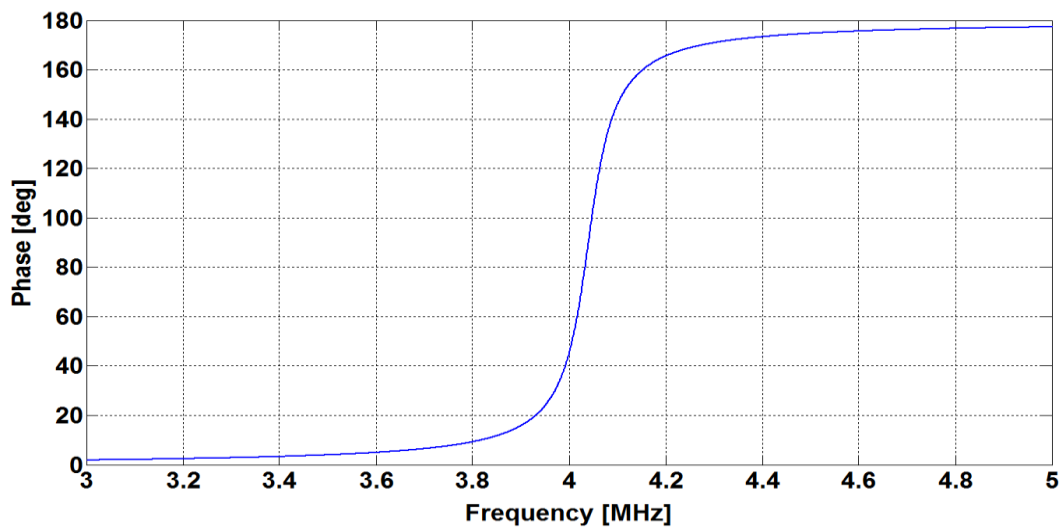


Fig. 3.7: Phase of a driven damped harmonic oscillator at $\zeta=0.02$ and $f_r=4.05$ MHz

3.5. Butterworth-Van Dyke Model

The comparison of the mechanical and electrical models shown in Figure 3.5 shows that the difference between the two models is given by the parallel capacitance C_p , which is inherent in a transducer where metal electrodes are separated by a disk. With regards to the experimental setup presented in Figure 3.13, the function generator which can be represented by a voltage source with output resistance ($\approx 50 \Omega$) is added to the total electrical excitation circuitry (Figure 3.8). The transmitter transducer is connected to this voltage source via an external resistance (R_1) of a typical value of 200Ω . In the case of simultaneous excitation (Figure 4.1), two resistances R_1 and R_2 are used. The total symmetry of the two electrical circuits can never be assumed. The values of R_1 and R_2 can be different, and also the material parameters of the two disks are clearly not identical. This difference in the two resistances does not cause a systematic TTD-offset error as long as both directions are symmetric in terms of impedance.

The harmonic model, which is independent of either single or simultaneous excitation, does not take into account the parallel capacitance C_p . Only the motional branch of the transducer's electrical model (Figure 3.5.b) can be represented by the harmonic oscillator model.

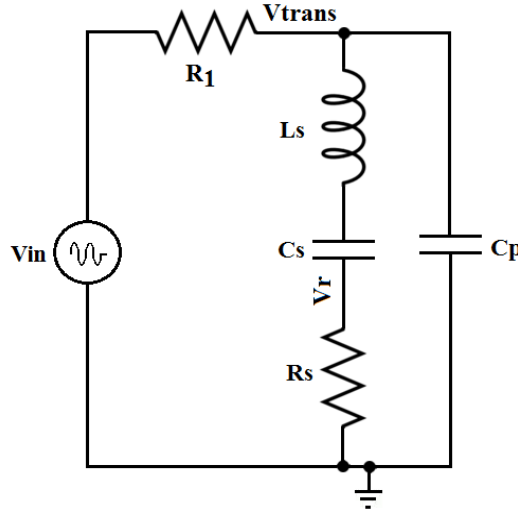


Fig. 3.8: Simulation circuit using the transducer electrical model

Regarding the "Vtrans" node, the AC analysis of the electrical circuit shown in Figure 3.8 results in the frequency response magnitude and phase plots shown in Figures 3.9 and 3.10, respectively. Hence, these results show a different behavior when compared to the harmonic model findings depicted in Figure 3.6 and 3.7. Therefore, due to the parallel capacitance C_p , the AC simulation results obtained with the transducer's electrical model (Figures 3.9 and 3.10) clearly demonstrate a restricted similarity compared to the findings obtained with the harmonic oscillator model (Figures 3.6 and 3.7). However, the analytic evaluation of the two parallel branches gives a rather complicated amplitude and phase equations (Equations (3.11) and (3.12)) compared to those obtained previously during the evaluation of the harmonic oscillator (Equations (3.9) and (3.10)). Thus, the transfer function V_{trans}/V_{in} of the electrical circuit shown in Figure 3.8 has a magnitude and phase shift, which are respectively given by:

$$A = \frac{\sqrt{(1-L_S C_S \omega^2)^2 + (R_S C_S \omega)^2}}{\sqrt{(1-R_1 R_S C_S C_p \omega^2 - L_S C_S \omega^2)^2 + (\omega((R_1 + R_S) C_S + R_1 C_p - L_S R_1 C_S C_p \omega^2))^2}} \quad (3.11)$$

$$\Phi = \tan^{-1} \frac{R_S C_S \omega}{1 - L_S C_S \omega^2} - \tan^{-1} \frac{\omega((R_1 + R_S) C_S + R_1 C_p - L_S R_1 C_S C_p \omega^2)}{1 - R_1 R_S C_S C_p \omega^2 - L_S C_S \omega^2} \quad (3.12)$$

Moreover, in the transducer electrical model the two parameters ω_r and ζ , which characterize the harmonic oscillator model, are extended to three parameters: ω_r , ζ , and C_p .

The amplitude response over frequency (Figure 3.9) displays following qualitative behavior: At low frequencies, the impedance of the motional branch is extremely high and the voltage "Vtrans" rises with increasing frequency. As the frequency increases, the capacitance C_s in the serial branch lowers the resulting impedance, and therefore the voltage "Vtrans" decreases as well. At the series resonance point the minimum impedance (R_s) is reached. At only slightly higher frequencies (at the parallel resonance point) the inductance dominates the resulting impedance of the motional branch. It resonates with C_p , causing the voltage "Vtrans" to increase. However, as the frequency gets higher, the parallel capacitance prevails so that "Vtrans" tends towards 0 V.

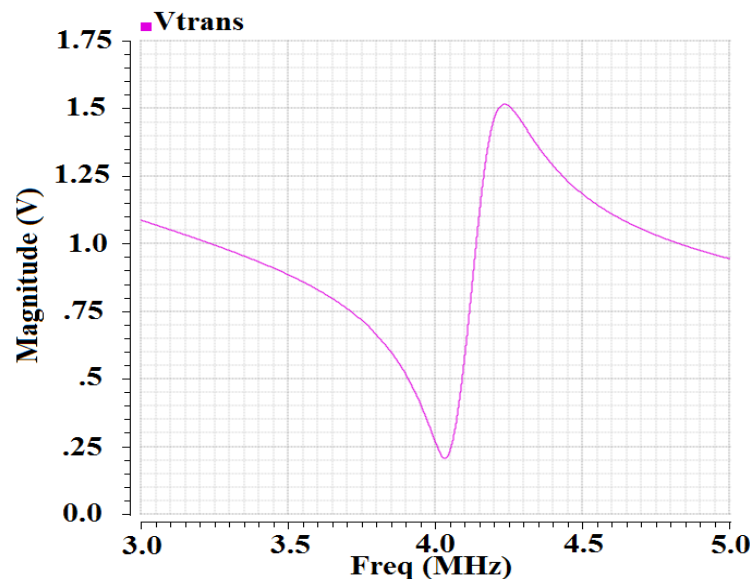


Fig. 3.9: Amplitude response at "Vtrans" node at $f_s = 4.05$ MHz and $f_p = 4.3$ MHz

The phase behavior shown in Figure 3.10 can be easily explained as follows: At low frequencies the resulting transducer impedance is given mainly by the capacitance C_s ; hence, when compared to the excitation phase shift, the phase tends towards -90° . At the point where forced frequency increases and reaches the serial resonance frequency, the effect of inductance and capacitance compensate each other, and the resulting impedance is given only by the resistance R_s , which represents the acoustical losses of the transducer to the surrounding environment and the energy transferred to the water [35]. In this case, the phase tends to 0° , and the equivalent transducer electrical model is simplified to a parallel

connection of R_s and C_p . However, as the frequency gets high, the inductance dominates the resulting impedance of the motional branch, and the phase tries to reach $+90^\circ$. At the operating point where the frequency becomes higher, the influence of C_p cannot be avoided. At this point the phase makes a fast transition from $+90^\circ$ to -90° .

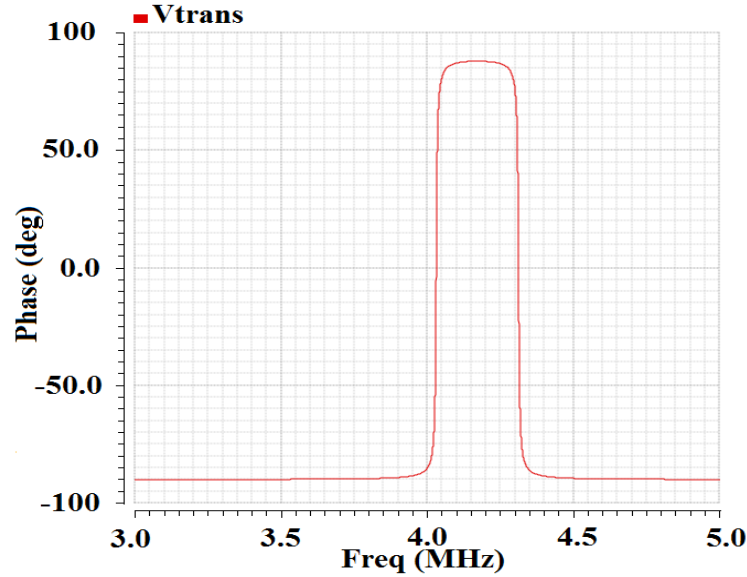


Fig. 3.10: Phase response at "Vtrans" node at $f_s = 4.05$ MHz and $f_p = 4.3$ MHz

Figures 3.9 and 3.10 show that the transducer exhibits two resonance frequencies at which it appears resistive. The first frequency, at which the impedance of the transducer is the smallest, is called series resonance frequency f_s . This resonant first point is created when C_s resonates with L_s . The second frequency, at which the impedance of the transducer is the greatest, is called parallel resonance frequency f_p . This resonant second point is created when L_s and C_s resonate with the parallel capacitor C_p . These two frequencies can be computed as follows:

$$f_s = \frac{1}{2\pi\sqrt{L_s C_s}} \quad (3.13)$$

$$f_p = \frac{1}{2\pi\sqrt{L_s \frac{C_s C_p}{C_s + C_p}}} \quad (3.14)$$

With respect to the last results shown in Figures 3.9 and 3.10, the assumption that the transducer can be modeled as a harmonic oscillator becomes valid only if the voltage over R_s is analyzed instead of "Vtrans" since the acoustic energy transmitted by the transducer to the water is proportional to the energy dissipated in the serial resistance R_s [36]. The

following two figures show the amplitude and the phase at node "Vr", respectively. There is a direct correspondence between the harmonic oscillator responses shown in Figures 3.6 and 3.7 and "Vr" responses presented in Figures 3.11 and 3.12. To sum up, these curves clearly demonstrate that the mathematic modeling based on the driven damped harmonic oscillator can govern the transducer's behavior.

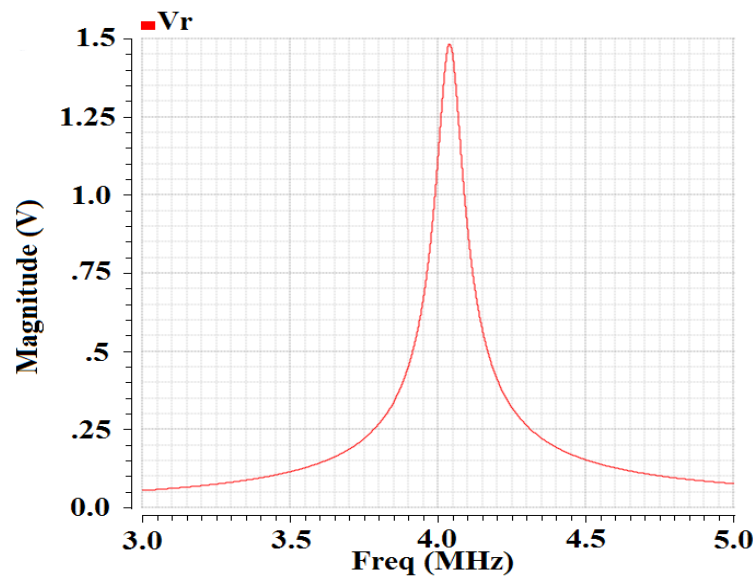


Fig. 3.11: Amplitude response at "Vr" node at $f_s = 4.05$ MHz and $f_p = 4.3$ MHz

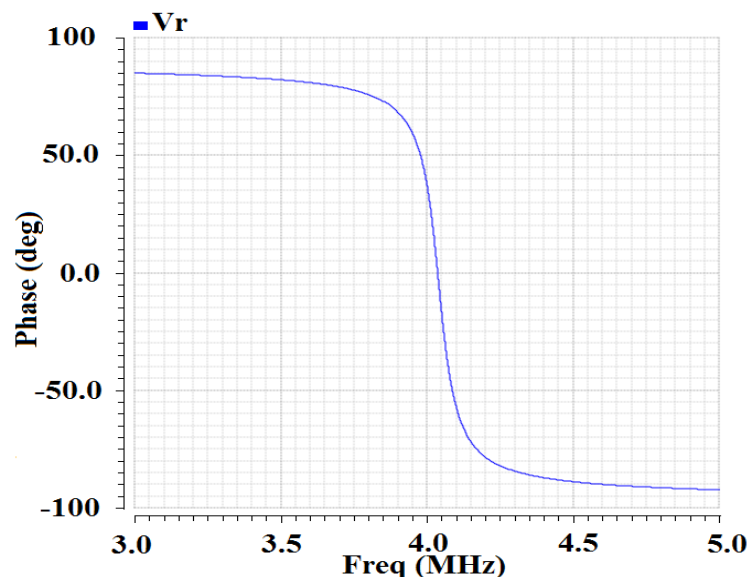


Fig. 3.12: Phase response at "Vr" node at $f_s = 4.05$ MHz and $f_p = 4.3$ MHz

Even under the condition that the magnitude and phase responses at the "Vtrans" node do not demonstrate the behavior of a driven damped harmonic oscillator, the "Vtrans" signal can be separated into three different regions on the basis of the harmonic oscillator

modeling aspects and according to the measured examples depicted in Figures 3.16 and 3.17.

- The first region contains both the homogeneous and the particular solution because the particular solution always represents a sine wave, and any deviations from sinus oscillations are caused by the homogeneous solution.
- The next region is characterized by the pure sinus wave, i.e., the homogeneous solution dies out because of the damping, and the remaining part is presented by the particular solution.
- The last region can be observed if the excitation is switched off. Hence, the homogeneous solution is active. This region is characterized by damped oscillations.

In this work, the transit time difference (TTD) measurements are restricted only to the second region (in further text quiet region or steady-state region). This region is characterized by the pure sinus of the particular solution. In this region the influence of C_p cannot be avoided. Hence, the current through C_p is given by:

$$I_{c_p} = C_p \frac{dV_{c_p}(t)}{dt}. \quad (3.15)$$

For a pure sinus burst, this current can be represented by a sinus oscillation as follows:

$$I_{c_p}(t) = A_1 \cos(\omega_f t + \Phi_1). \quad (3.16)$$

The total current flowing into the two branches of the circuit shown in Figure 3.8 can be calculated as the sum of the current flowing through C_p and the current flowing into the motional branch:

$$I_{serie} + I_{c_p} = A_0 \cos(\omega_f t + \Phi_0) + A_1 \cos(\omega_f t + \Phi_1) = A_2 \cos(\omega_f t + \Phi_2), \quad (3.17)$$

where,

$$A_2 = \sqrt{(A_0 \cos(\Phi_0) + A_1 \cos(\Phi_1))^2 + (A_0 \sin(\Phi_0) + A_1 \sin(\Phi_1))^2}, \quad (3.18)$$

$$\Phi_2 = \tan^{-1} \frac{A_0 \sin(\Phi_0) + A_1 \sin(\Phi_1)}{A_0 \cos(\Phi_0) + A_1 \cos(\Phi_1)}. \quad (3.19)$$

The influence of the parallel capacitance on the second region, which is characterized by the particular solution of forced oscillation, results in a simple phase shift. Hence, instead

of ϕ_0 , a slightly changed value ϕ_2 can be detected. The amplitude undergoes a similar change. Since the transit time difference is computed as the phase difference between the two received signals², the changes of the amplitude do not affect the measurement accuracy.

3.6. Transmitted and Received Signals Modeling

Numerical solutions of the motion equations are obtained using Matlab in order to emulate the measured transmitted and received signals. These waveforms are subsequently compared to the experimentally measured ones. The measurement principle used in the experiments is shown in Figures 3.13 and 3.14. The transducer T_{R1} is excited through the resistance R by a sinusoidal burst in order to generate an ultrasonic signal that can be received by the second transducer T_{R2} after traveling through the water within the distance that separates the two transducers.

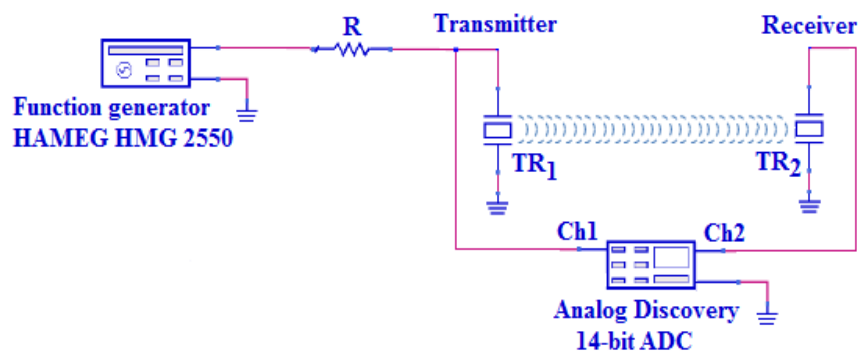


Fig. 3.13: Experimental setup used to generate and detect the ultrasonic waves

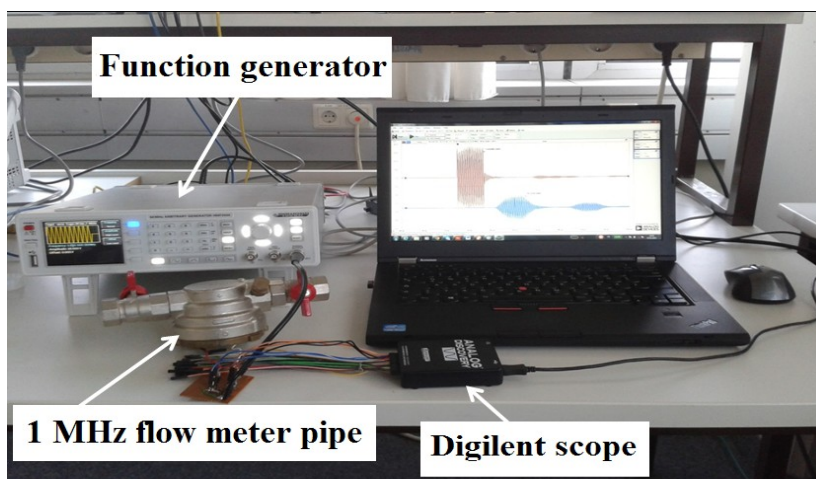


Fig. 3.14: The experimental setup

² For further details see Chapter 4.

Figure 3.15 shows a screenshot of Digilent Analog Discovery digital oscilloscope displaying the transmitted and received signals measured with 1 MHz flow meter pipe. Assuming that the sound velocity at ambient temperature is 1500 m/s, the sound wave traveling time calculated for an ultrasonic path length between T_{R1} and T_{R2} of $L \approx 49.5$ mm is about 33 μs .

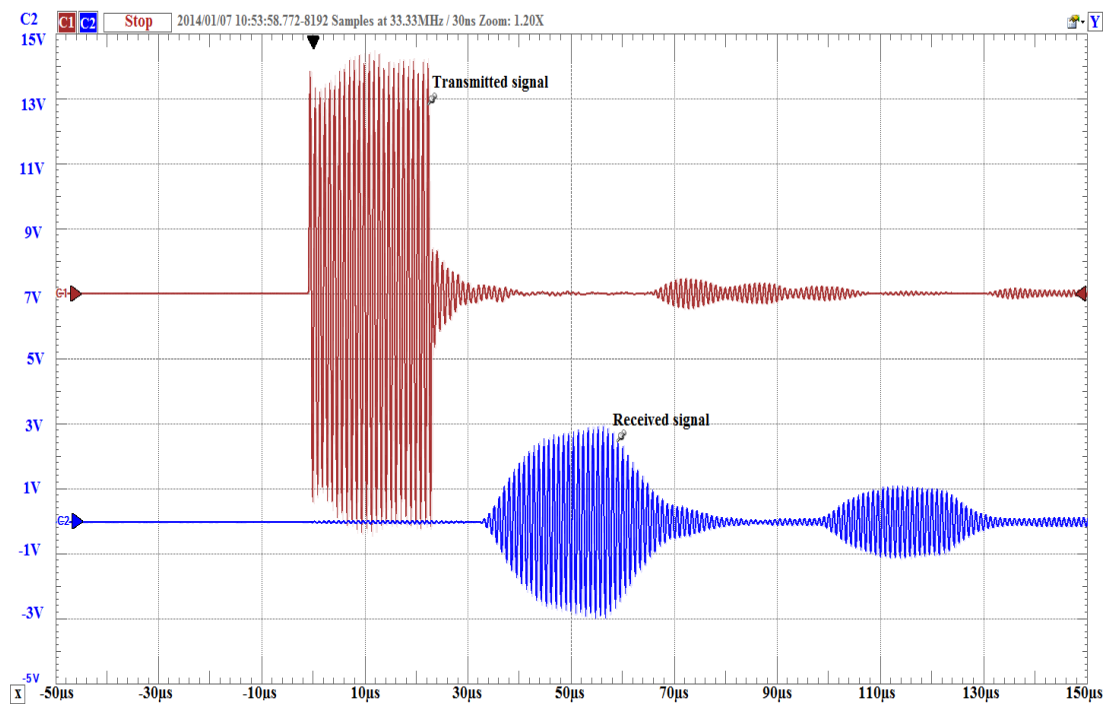


Fig. 3.15: A screenshot of the transmitted and received waveforms

The two channel measured waveforms demonstrate a loss in the amplitudes between transmission and reception. The 1 MHz flow meter pipe shows that the ultrasonic received signal is attenuated by a factor of 2.5 compared to the transmitted signal, whereas for the 4 MHz flow meter pipe the attenuation factor becomes nearly 10 (Figure 3.22).

3.6.1. Transmitter

From the modeling point of view, the transmitted signal can be divided into two parts. The first part is characterized by the fact that the homogeneous and the particular solution are both active. The second part is provided only by the homogeneous solution since the excitation is switched off. Hence, the signal dies off gradually since there is no driving force. According to our measurements, the decay of the amplitude lasts about 10 to 15 periods.

Regarding the particular and the homogeneous solution (Equations (3.5) and (3.6), respectively), three parameters - transducer resonance frequency ω_r , damping coefficient ζ , and the angular driving frequency ω_f - are used in order to emulate the transmitter signal. Figure 3.16 shows the simulated as well as the measured transmitted waveforms for 27 periods of uniform sinusoidal applied voltage. The simulation is performed at a damping coefficient $\zeta = 0.05$, a resonance frequency $f_r = 1$ MHz ($f_r = 2\pi/\omega_r$), and a forced frequency $f_f = 1$ MHz ($f_f = 2\pi/\omega_f$), whereas the measured signal is obtained at $f_f = 1$ MHz. The second example shown in Figure 3.17 is obtained by changing only the forced frequency f_f from 1 MHz to 1.1 MHz for the simulated and for the measured signals.

The differences caused by the parallel capacitance can be observed, especially at the beginning when the excitation starts and in the moment when the excitation is switched off. It can be seen that the blue and red curves look very similar outside the switching-on and -off behavior. A 10% change in the driving frequency provides a remarkable difference in the shape between the two waves depicted in Figures 3.16 and 3.17.

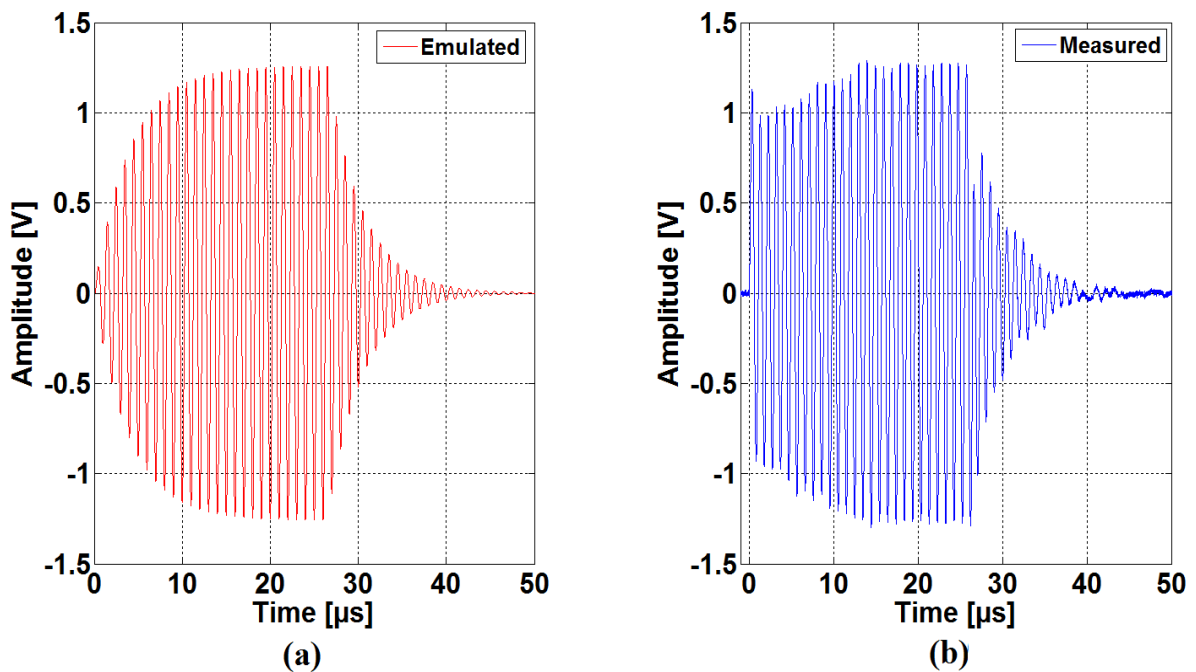


Fig. 3.16: Transmitter response for a 1 MHz flow meter pipe and $L = 49.5$ mm at $f_f = 1$ MHz: (a) emulated waveform, (b) measured waveform

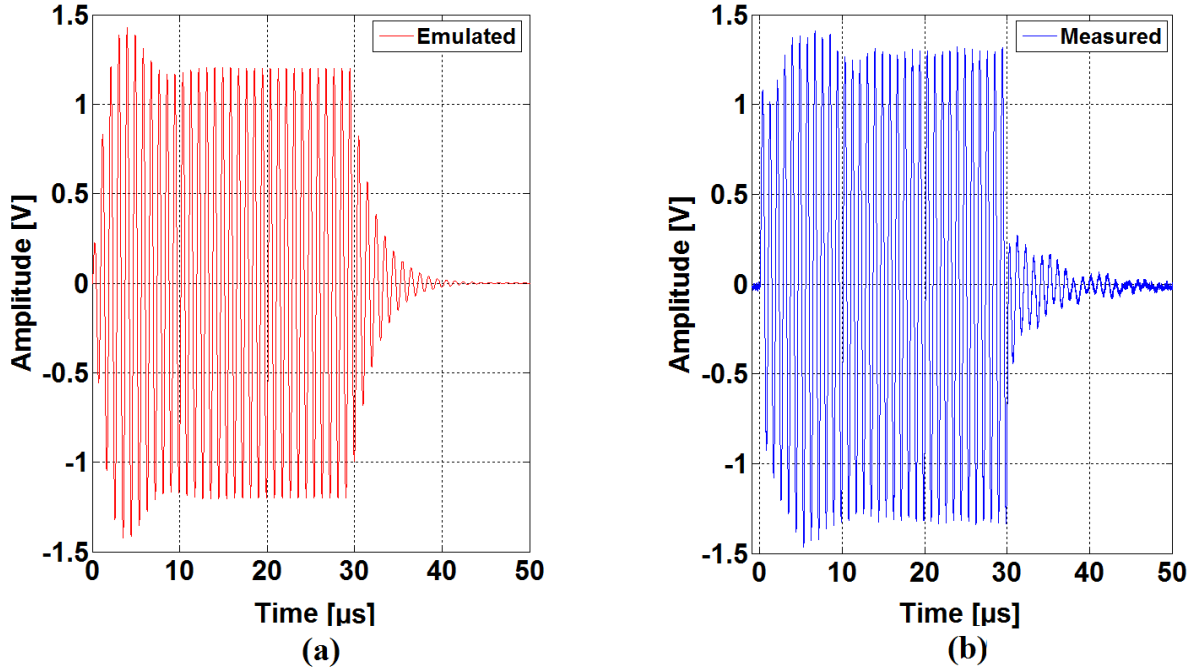


Fig. 3.17: Transmitter response for a 1 MHz flow meter pipe and $L = 49.5$ mm at $f_f = 1.1$ MHz: (a) emulated waveform, (b) measured waveform

3.6.2. Receiver

Assuming that the transmitted signal, which is directed towards the second transducer, is defined by the complete solution of Equation (3.4) (the homogeneous and the particular solutions), this complete solution is used to replace the second part of the second order differential harmonic equation (Equation (3.3)). The following equation can be used to emulate the receiver waveforms:

$$\frac{d^2 Q(t)}{dt^2} + 2\zeta_2 \omega_{r2} \frac{dQ(t)}{dt} + \omega_{r2}^2 Q(t) = A_h e^{-\zeta_1 \omega_{r1} t} \sin(\omega_d t + \theta) + A_p \cos(\omega_f t - \phi). \quad (3.20)$$

According to the numerical solution of Equation (3.20) obtained using Matlab, five parameters are now used in order to emulate the ultrasonic receiver signal: two parameters of each of the two transducers $\omega_{r1,2}$, $\zeta_{1,2}$, and the angular forced frequency ω_f . Hence, the receiver waveform is characterized by two intervals. During the first time interval, the external force is given by " $Q_h(t) + Q_p(t)$ ", while during the second interval the external force is given by only $Q_h(t)$. Figure 3.18 shows the result of the simulated receiver results achieved for the parameter values $\zeta_1 = 0.01$, $\zeta_2 = 0.02$, $f_{r1} = 1.01$ MHz, $f_{r2} = 1.02$ MHz. The external force is activated at the same frequency of 1 MHz for 33 cycles for both simulated and measured signals. The shapes of both waveforms look very similar. The measured

curve shows a difference at the end after roughly $103 \mu\text{s}$, where the first reflected signal already approaches the received signal, causing interference between both signals.

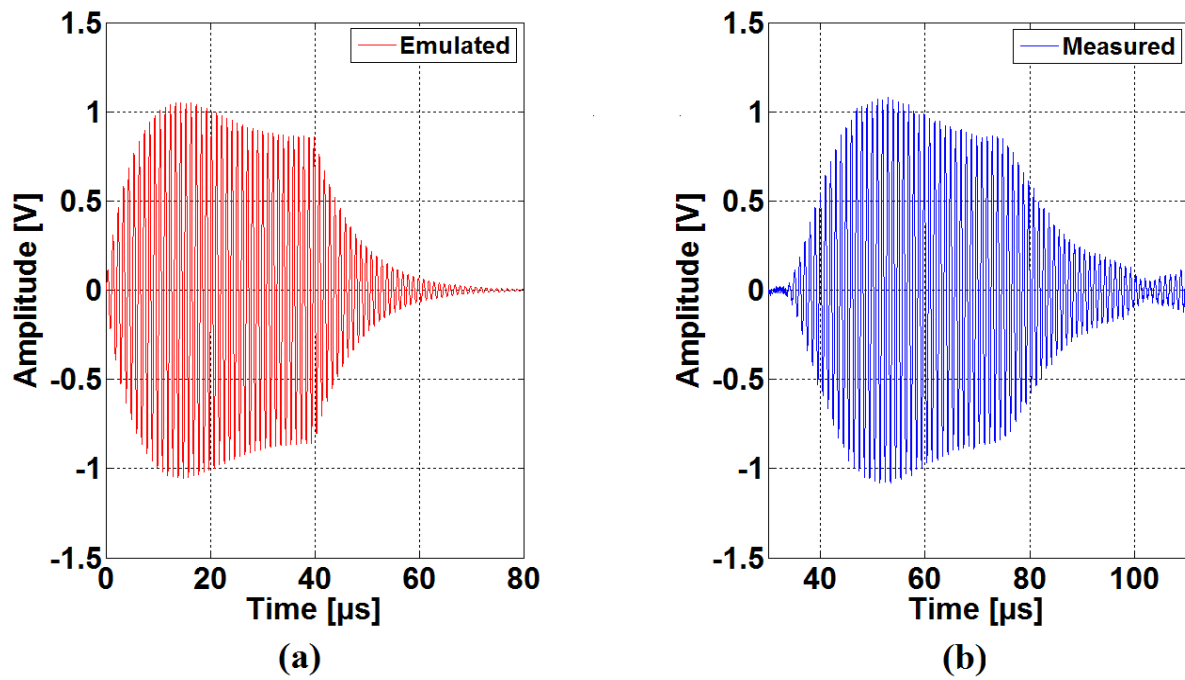


Fig. 3.18: Receiver response for a 1 MHz flow meter pipe and $L = 49.5 \text{ mm}$ at $f_f = 1 \text{ MHz}$: (a) emulated waveform, (b) measured waveform

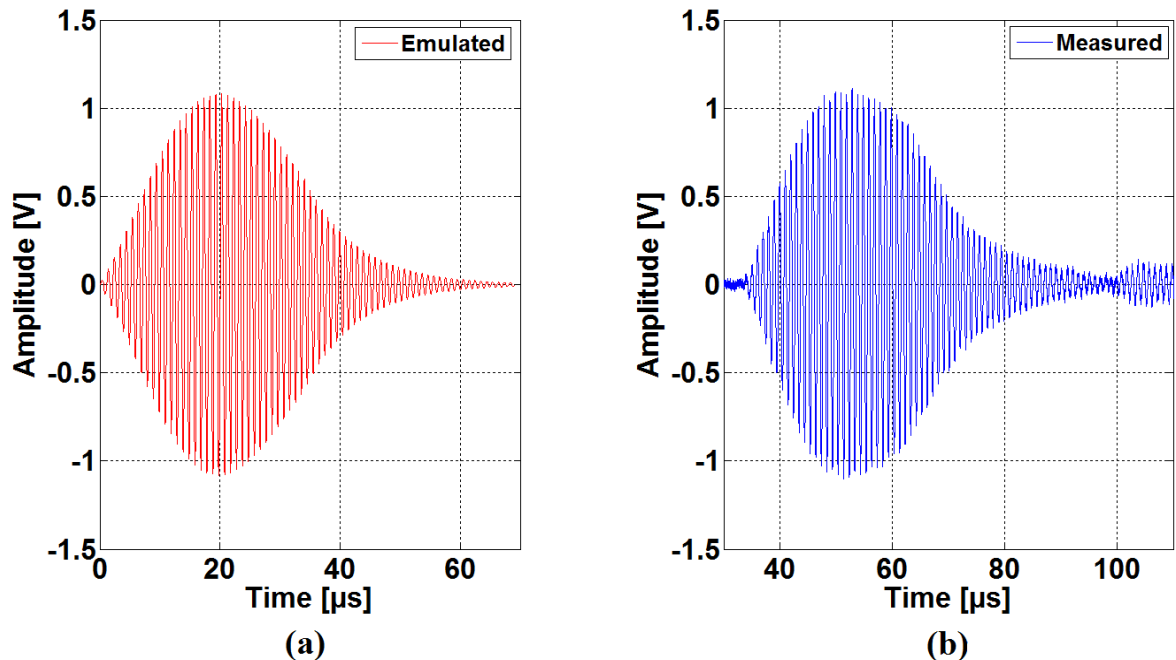


Fig. 3.19: Receiver response for a 1 MHz flow meter pipe and $L = 49.5 \text{ mm}$ at $f_f = 1.02 \text{ MHz}$: (a) emulated waveform at $\zeta_1 = 0.01$, $\zeta_2 = 0.018$, $f_{r1} = 1 \text{ MHz}$ and $f_{r2} = 1.02 \text{ MHz}$ (b) measured waveform

By comparing the measured receiver and transmitter signals, it can be deduced that the switch-on and the switch-off behavior of the excitation, which creates spikes in the ultrasonic transmitted signals, is no longer seen in the received ones. Therefore, in contrast to the transmitter, the receiver is activated and deactivated rather smoothly. The flowing of the current over C_p does not produce any signal spikes since the ultrasonic transmitter signal impacts the receiver transducers more or less continuously. The influence of C_p is correspondingly small.

In summary, the model of the harmonic oscillator is found to be the most effective to describe and analyze the measured curves. The different physical waveforms in Figures 3.16 to 3.19 can be easily emulated by an appropriate choice of three parameters (the transmitter transducer parameters ω_r , ζ , and the angular driving frequency ω_f) in the case of the transmitted signal, and five parameters (the two transducers parameters $\omega_{r1, 2}$, $\zeta_{1, 2}$, and the angular forced frequency ω_f) in the case of the received signal. Obviously, the requirement specified previously - an analytical description of the resulting signals - is fulfilled by modeling the piezoelectric transducer as a driven damped harmonic oscillator.

3.7. Quiet Region Aspect

After the decay of the transient part of the ultrasonic signal, the resulting signal is characterized by a constant phase, uniform amplitude, and a frequency which matches the forced frequency. Hence, the mathematic representation of this signal is given by the particular solution equation³. As mentioned previously, the evaluation of the measured curves has to be restricted to this "quiet" time interval. Therefore, it becomes necessary to analyze quantitatively the influence of the homogeneous solution (transient response): what is the minimum number of cycles required in a burst excitation to make sure the transient region dies off completely and the steady-state is reached? This can be determined by estimating the frequency variation through the transmitted or the received signals using consecutive zero-crossings. The good agreement between the emulated and the measured curves (Figures 3.16 - 3.19) allows to use of the former ones to perform the frequency variation estimation. Figure 3.20 illustrates the frequency variation, which is performed on the basis of the emulated transmitter signal example for $f_f = 1.02$ MHz, $\zeta = 0.05$, and $f_r = 1$ MHz, and using the analysis of the zero-crossings.

³ See Equation (3.6).

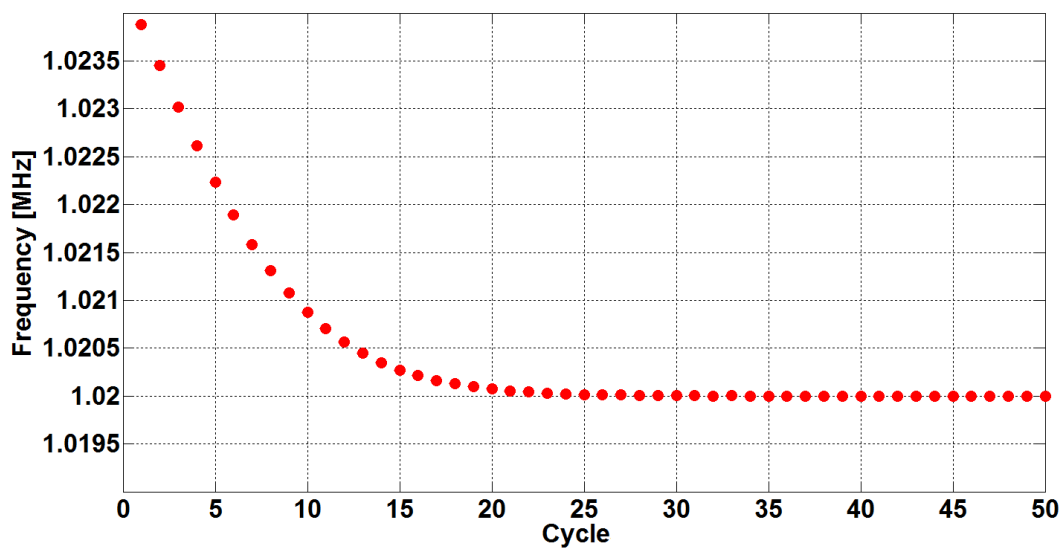


Fig. 3.20: Frequency variation through the transmitted signal

The zero-crossings are calculated by the linear interpolation between every pair of successive positive and negative signal values and their corresponding time on the x-axis. As a result, the homogeneous solution or the resonance effect dies out after about 25 periods, which allows the transducer to reach the so-called quiet region or the steady-state region [37]. In order to achieve high accuracy of less than 20 ps peak-to-peak TTD-jitter and TTD-offset of zero, the TTD measurements are carried out only within this steady-state region⁴.

It can be deduced from the results reported in Figure 3.20 that the transducer must be excited by a burst of more than 25 cycles in order to generate enough measurement points in the quiet region parts of the ultrasonic signals, i.e., typically 50 to 70 periods of excitation. The number of the allowed excited cycles is strictly limited by wave reflections generated by the other transducer on the opposite side of the pipe. This problem becomes more serious when the excitation of the two transducers is done simultaneously and the ultrasonic path length is between 5 and 8 cm. Then, the number of cycles is limited to only about a half of the sound wave traveling time. However, when a single excitation is used to excite the transducers, the number of cycles is limited to about a sound wave traveling time since the transmitted and the received signals are acquired from different scope channels.

In order to reach a minimum TTD-jitter and TTD-offset in the receive mode, the transducer has to recover from the transmit mode and achieve a state where it becomes completely

⁴ See Section 4.5 of Chapter 4 for further discussion.

calm after passing the transient part, where free vibration is still valid. Therefore, it is necessary either to extend the pipe length or to use a pair of transducers with a sufficiently high resonance frequency. For a 1 MHz flow meter pipe and within a typical distance of about 5 cm, the number of periods is limited to roughly 20. However, a 4 MHz flow meter pipe allows 4 times more periods. In this work, we chose to switch from 1 MHz to the 4 MHz flow meter pipes (Figure 2.2), where typically a sinus burst of 70 cycles is used for excitation.

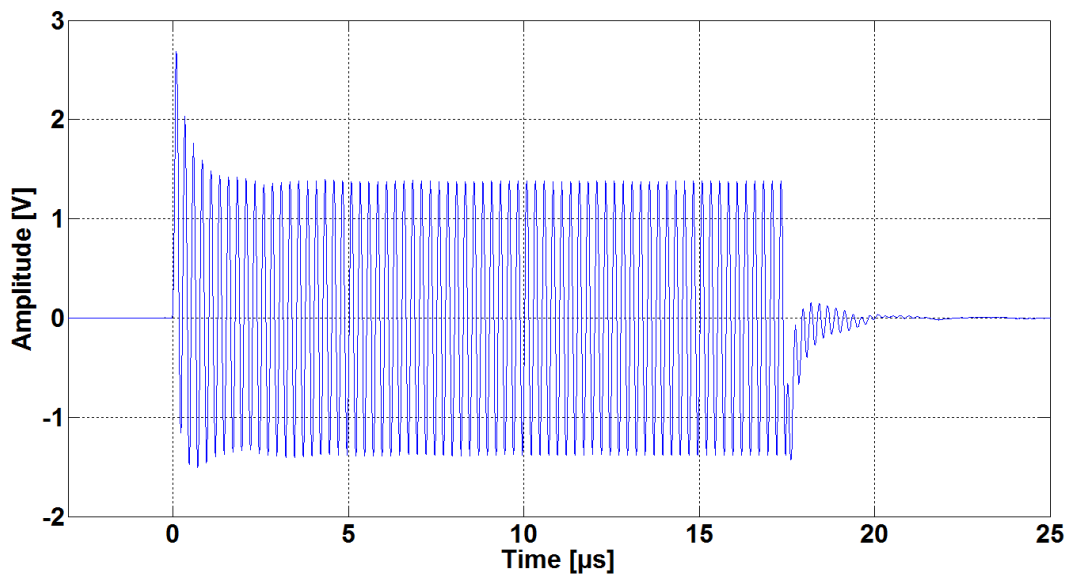


Fig. 3.21: Measured transmitted signal of the 4 MHz flow meter pipe

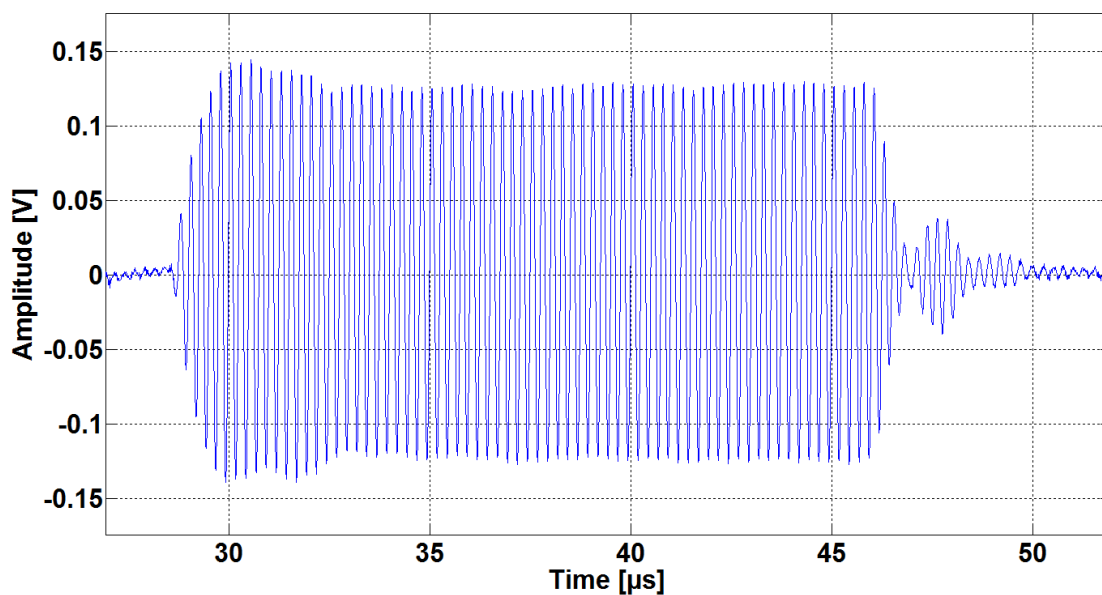


Fig. 3.22: Measured received signal of the 4 MHz flow meter pipe

3.8. Characteristic Frequencies of Piezoelectric Transducer

As mentioned in Section 3.5, there are two frequencies which characterize the piezoelectric transducer impedance: the series and the parallel frequencies. In order to estimate the frequencies which characterize the 4 MHz transducer pair located in the 4 MHz flow meter pipe used in our experiments, a variation of transmitter voltages VTD_1 and VTD_2 in both directions with respect to the driving frequency is obtained experimentally using the measurement setup shown in Figure 3.13 and the 4 MHz flow meter pipe. The amplitude voltages are estimated in the steady-state region of transmitted signals in both directions using least square sine-fitting. This experiment result (Figure 3.23) shows the same general characteristics when compared to the simulated magnitude response of the electrical model of the transducer shown in Figure 3.9. The piezoelectric series resonance frequency corresponds to the minimum impedance of the transducer (minimum amplitude in Figure 3.23), and the parallel resonance frequency corresponds to the maximum impedance of the transducer (maximum amplitude in Figure 3.23). The transducer is protected by its high impedance in order to transmit the maximum energy to the water. The maximum voltage results from the fact that the driver sends a minimum of energy to the transducer, thus the current over R_s (Figure 3.8) becomes minimal.

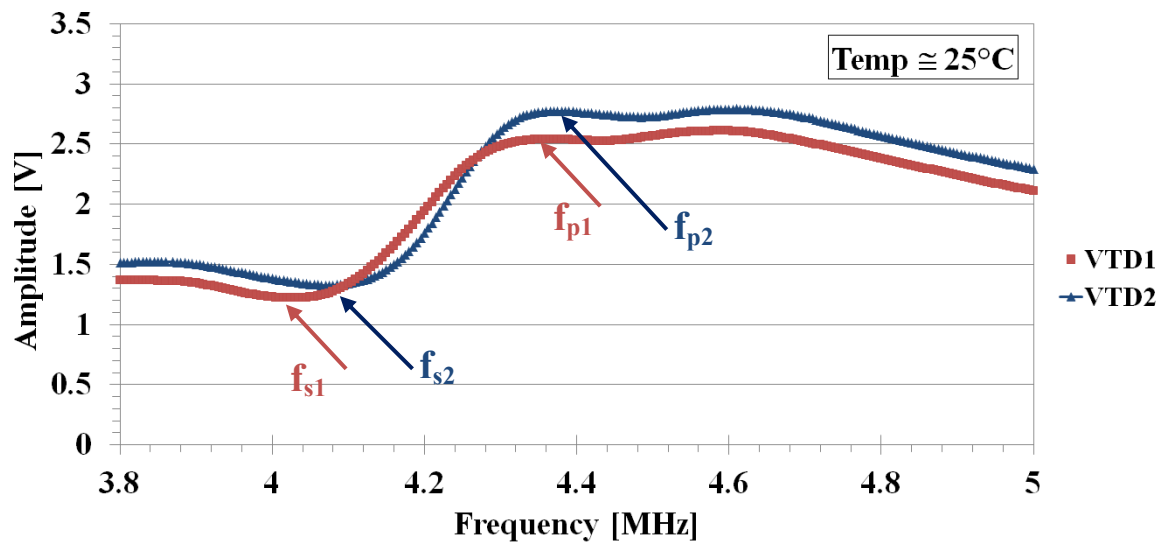


Fig. 3.23: Measured transmitter voltages versus driving frequency, performed at ambient temperature

Chapter 4

Determination of Transit Time Difference

4.1. Introduction

The transducer model based on the driven damped harmonic oscillator model shown in Chapter 3 allows an accurate description of the behavior of a piezoelectric transducer. The free oscillation of the transducer dies out when it is excited by a burst of a sufficient number of cycles in order to allow the transducer to reach a steady-state. We take advantage of this phenomenon - the dying out of the transient region - to measure indirectly the transit time difference (TTD) by computing the phase difference between the steady-state region of received signals in the upstream and downstream directions. Many factors significantly influence the upstream and downstream transit times, such as water viscosity, temperature-dependent transducer parameters, and the speed of sound c , which is related to the compressibility K and the density ρ of water by the following equation:

$$c = \frac{1}{\sqrt{K \cdot \rho}}. \quad (4.1)$$

All these factors impose great challenges to develop a new methodology for achieving high measurement accuracy with reduced TTD-jitter and compensated TTD-offset at no-flow conditions and within a temperature range from room temperature to 80°C.

The first part of this chapter introduces the experimental setup for measuring the TTD, followed by the description of the transmission and reception electronics associated with the transducers.

The second part of the chapter describes the methodology applied to compute the TTD.

4.2. Experimental Setup for Measuring the TTD

The operational principle of the system used in the experiments is illustrated in Figure 4.1. As mentioned previously in Chapter 3, in order to allow the receiving transducer to reach a steady-state where both amplitude and frequency are settled, a sinusoidal burst of 70 cycles generated over a time period of 100 ms by a function waveform generator (Hameg HMF 2550) is used to drive the two transducers (TR_1 and TR_2) simultaneously through the resistances R_1 and R_2 . These transducers convert electrical excitation into a mechanical wave. The driving frequency of the burst is selected near the resonance frequencies of both transducers in order to achieve the maximum output vibration with an enhanced SNR.

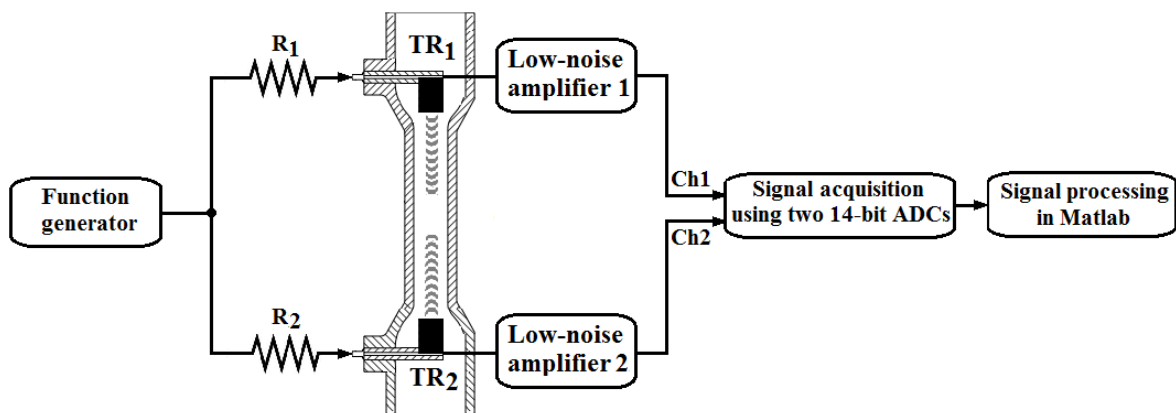


Fig. 4.1: Block diagram of the experimental setup for measuring the TTD

Figure 4.2 shows a picture that was taken while performing the measurements.

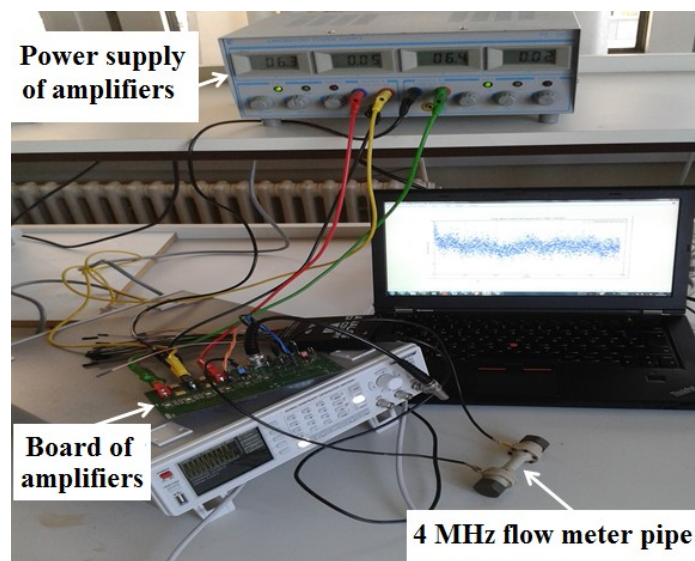


Fig. 4.2: Experimental setup for measuring the TTD

In order to eliminate the high starting jitter, which is caused by triggering and recording ultrasonic signals from both directions separately (sequentially), we rely on the simultaneous (synchronous) excitation approach. This means that the common synchronized clock of the dual channel digital oscilloscope (Digilent Analog Discovery) is used to trigger and acquire signals from both directions. Hence, we eliminate any differential delay time between the two input channels.

As shown in Figure 4.3, the sound waves are received simultaneously by both transducers after a traveling time that is proportional to the distance between the transducers ($L = 42.2$ mm). The received signals are attenuated due to the loss or absorption of acoustical energy by the medium [34]. Therefore, we use two low-noise operational amplifiers (OPA2846ID), shown in Figure 4.1, in order to increase the signal levels. The amplified signals are acquired by the digital oscilloscope, which has two 14-bit channels with a sampling rate of 50×10^6 Samples/s per channel. The samples are saved in comma-separated values (CSV) data format and imported to the computer (PC). An embedded (PC) software algorithm written in Matlab handles the automatic TTD measurement repetition, providing all necessary programs to control the function generator and digital oscilloscope.

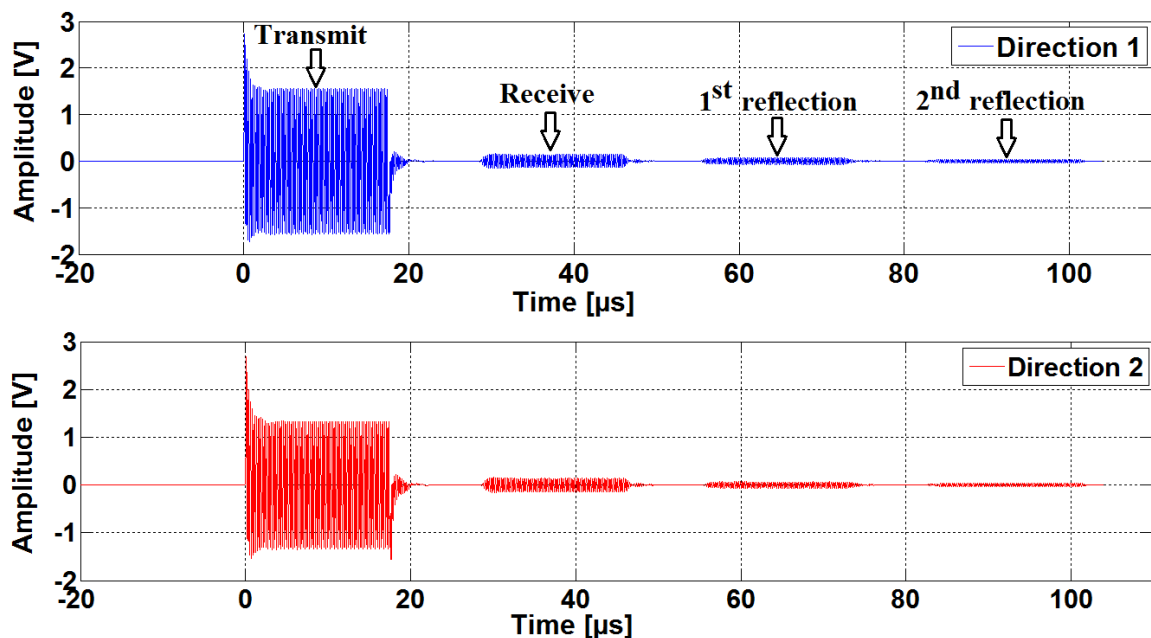


Fig. 4.3: Acquired ultrasonic signals in both directions
(measured using a 4 MHz driving frequency)

4.3. Methodology for the Calculation of TTD

The TTD can be deduced from the phase difference between the steady-state parts of the received signals in the upstream and downstream directions by estimating the two phases with the least squares sine-fitting algorithm of Matlab (see Figure 4.4) [19] [38]:

$$\varphi_{up} = 2\pi f t_{up}, \quad (4.2)$$

$$\varphi_{down} = 2\pi f t_{down}, \quad (4.3)$$

where φ_{up} and φ_{down} are the phase shifts between the received and transmitted signals measured in the steady-state regions (see Figure 4.5) in the upstream and downstream direction, respectively. In the quiet region, the received signal frequency f matches the forced frequency of the exciting signal. Therefore, the TTD can be computed as follows:

$$\varphi_{up} - \varphi_{down} = 2\pi f (t_{up} - t_{down}). \quad (4.4)$$

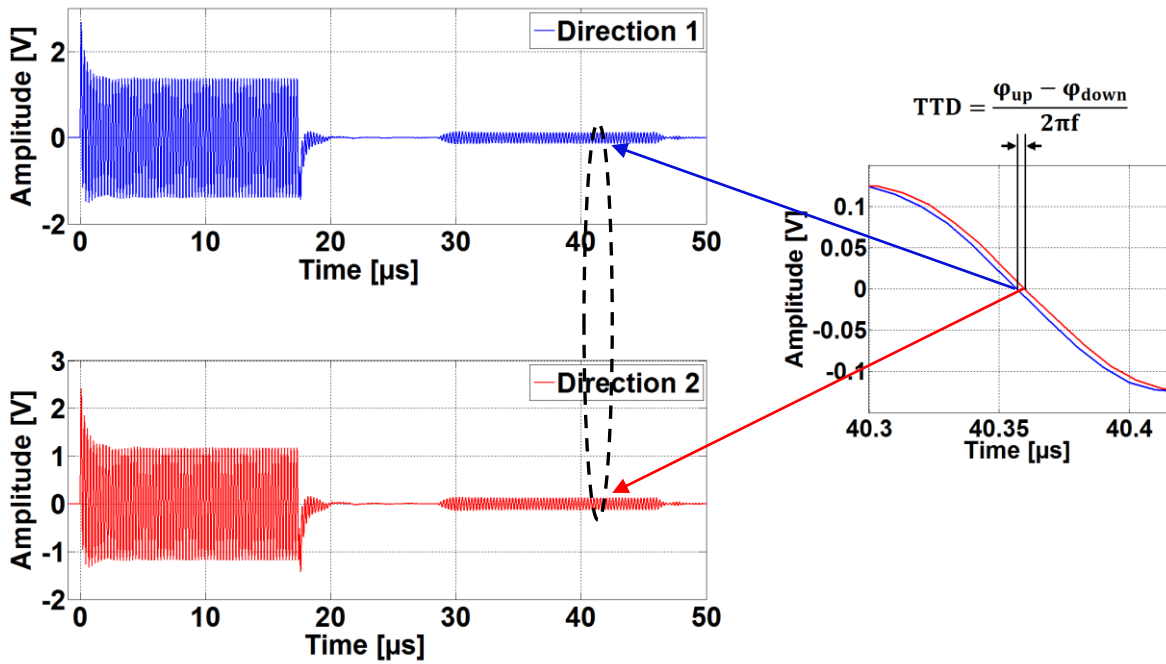


Fig. 4.4: Phase difference between the steady-state region of received signals in both directions

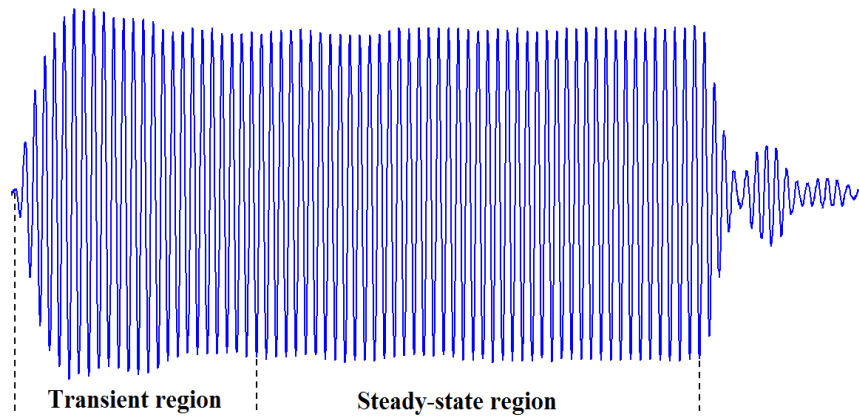


Fig. 4.5: Response of the 4 MHz transducer to the incident ultrasonic wave

Assuming that the phase shifts between the electric and acoustic signals on both transducers for transmitted signals are φ_{t1} , φ_{t2} and φ_{r1} , φ_{r2} for received signals, the total calculated phase difference (φ_T) between the signals recorded from both directions is given by [19]:

$$\varphi_T = \varphi_{t1} + 2\pi f t_{up} + \varphi_{r2} - \varphi_{t2} - 2\pi f t_{down} - \varphi_{r1}. \quad (4.5)$$

Since t_{up} and t_{down} are the same at no-flow conditions according to [7] and [19] under electro-acoustical reciprocal operation, in which $\varphi_{t1} + \varphi_{r2} = \varphi_{t2} + \varphi_{r1}$, the phase difference between the upstream and downstream directions can be compensated. Such operation requires that the equivalent electrical impedances of the electronics and transducers are equal in both directions. Therefore, under this condition the unmatched transducers are no longer the only reason for the TTD-offset drift produced at no-flow conditions. The dissymmetry between the two directions signal paths (in terms of the electrical impedances of the electronics and transducers used in the meter), which mainly causes the TTD-offset.

4.4. Least Squares Sine-Fitting

The least squares sine-fitting (LSSF) is a very accurate method to estimate all three parameters - amplitude, phase, and frequency - that characterize a digitized sinusoidal signal sampled at a well-defined sampling rate [39]. The sine-fitting technique is used as a filter and can significantly reduce noise such as the ADC quantization noise [40]. This procedure is very often used to recover distorted and noisy signals in tests and measurements [41-45]. A three-parameter sine-fit algorithm is used for a reasonable estimation of amplitude, phase, and frequency of each recorded sample. Assuming that the data of n samples has been saved, the fitted function is given by:

$$x(n) = A \sin(2\pi f t_n + \varphi), \quad (4.6)$$

where A and φ are the amplitude and the phase of the signal, respectively, f is the driving frequency, and t_n is the discrete-time vector.

The sum of squares of the error between these three extracted parameters and the measured data is given by:

$$\epsilon = \sum [x(n) - A \sin(2\pi f t_n + \varphi)]^2. \quad (4.7)$$

The algorithm chooses successive values of A , f , and φ to minimize ϵ , taking into account the signal-to-noise-and-distortion ratio [41] [45].

4.5. Estimation of the Quiet Region

As mentioned before, accurate phase estimation from the acquired recorded data is performed in the quiet parts of received signals. As shown in Figure 4.6.b, relatively high random fluctuations in voltage occur in the region between the transmitted and received signals, which can influence measurement accuracy. Such voltage fluctuations arise due to insufficient time, which leads to a complete decay of the transmitted signal to zero before the arrival of the received signal due to simultaneous excitation. In the case of single excitation, the transmitted and the received signals are acquired from different scope channels, as shown in Figure 4.7. It demonstrates that only a few millivolts typical noise floor of the digital oscilloscope is observed before the start of the transmitted signal and the arrival of the received signal (Figure 4.7.a and 4.7.c). This also shows that in our chosen technique the higher voltage noise arise due to the proximity of the transmitted and received signals in the same channel.

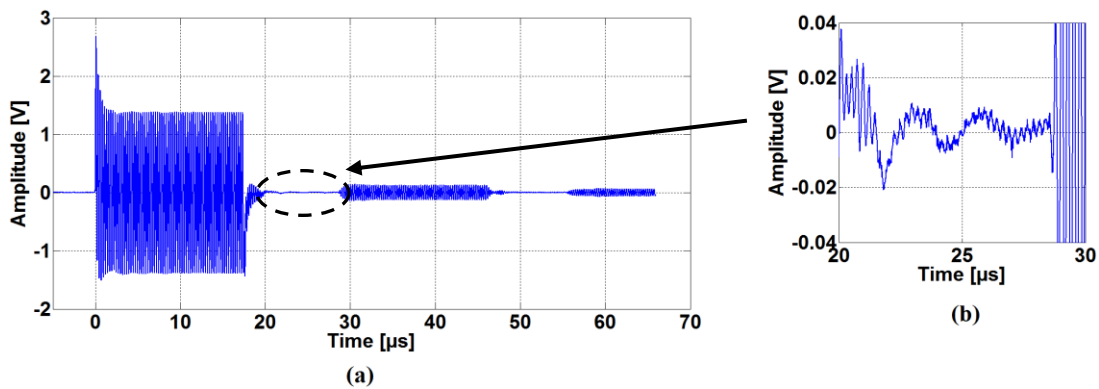


Fig. 4.6: Voltage fluctuations in the region between the transmitted and received signals measured at simultaneous excitation

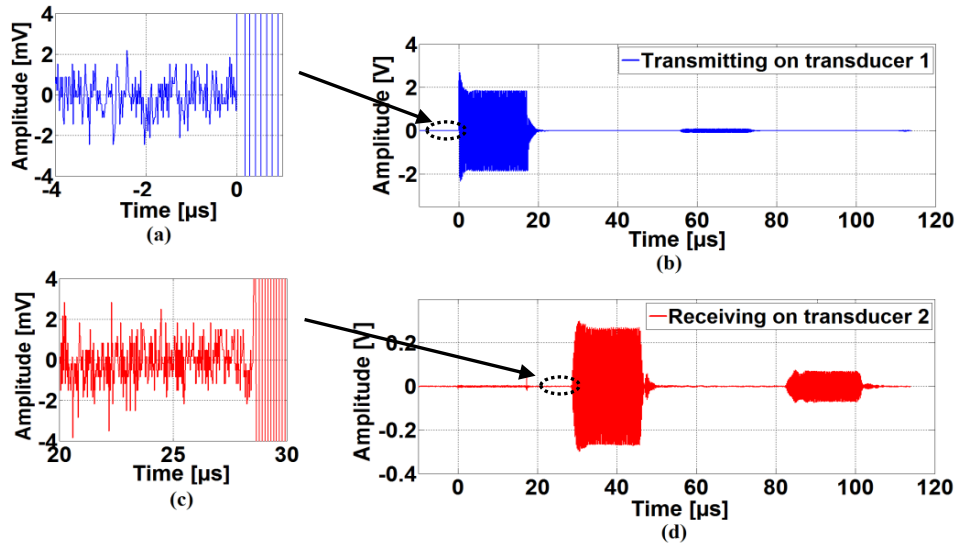


Fig. 4.7: Noise of the oscilloscope measured at single excitation

In order to protect the phase measurement interval from these voltage fluctuations, the transducer should be excited for a sufficiently long period of time. Figures 4.8 and 4.9 show the results of the cycle-by-cycle time delay of the transmitted and received signals, respectively. These results are calculated through the estimation of phase shifts of the 70 periods between the electric and acoustic signals on both transmitting and receiving transducers in both directions by using sine-fitting. These results show that after 50 cycles of excitation the two transmitted and received signals look more steady and the transient region (free oscillation of the transducer) has completely died out. Therefore, on the basis of these results we decided to use the last 20 periods to extract sine-fitting parameters in all our experiments.

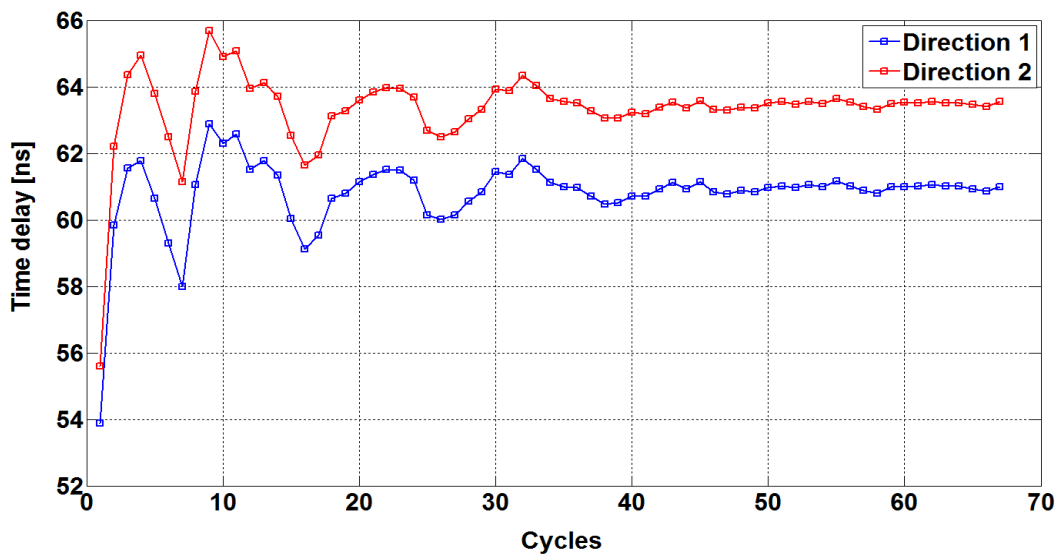


Fig. 4.8: The cycle-by-cycle time delays of both transmitted signals in both directions

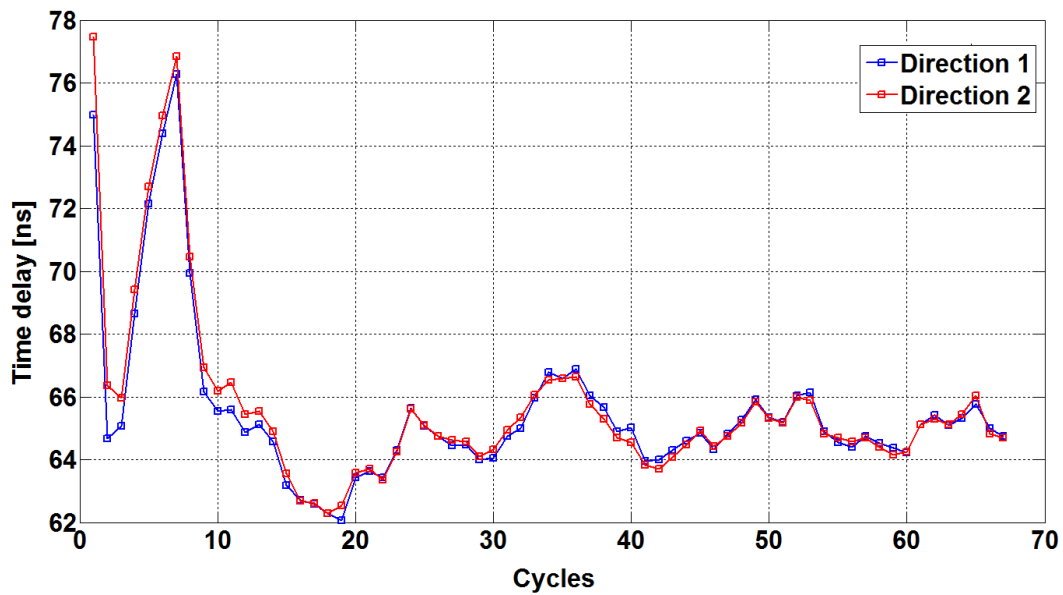


Fig. 4.9: The cycle-by-cycle time delays of both received signals in both directions

4.6. Algorithm for Computing the TTD

The main components of the algorithm used for estimating the phase and computing the TTD are shown in Figure 4.10. A sine-fitting technique is used to reduce the error in the phase estimation. This technique estimates the sine wave that best fits the recorded samples of the last 20 cycles of signals received from both directions. The algorithm used for computing the TTD value performs the following steps:

- Read the recorded data saved in CSV format.
- The DC offset correction is performed to remove it from the acquired signal. This correction is done by computing the mean voltage value of all recorded voltage samples, which is then subtracted from each data voltage sample.
- An estimation of both frequencies of sine waves from the recorded sampling data is performed by using the least squares sine-fitting algorithm of Matlab. This estimation is carried out in the steady-state parts of received signals in upstream and downstream directions.
- An estimation of amplitude and phase, which characterize the digitized sinusoidal signals, is performed by using the previously obtained mean value of the fitted frequencies.
- Calculate the difference between the two fitted phases.
- Calculate the TTD.

In order to control the shape of the curve, the upper and lower bounds of the estimated parameters (amplitude, phase, and frequency) that characterize the digitized sinusoidal is introduced. For instance, the amplitude has bounds $[0, 5]$, the phase has the bounds $[-\pi, \pi]$. With this construction in place, the fitted curve accurately extracts parameters from the measured data, especially the two phases that are used to calculate the transit time difference.

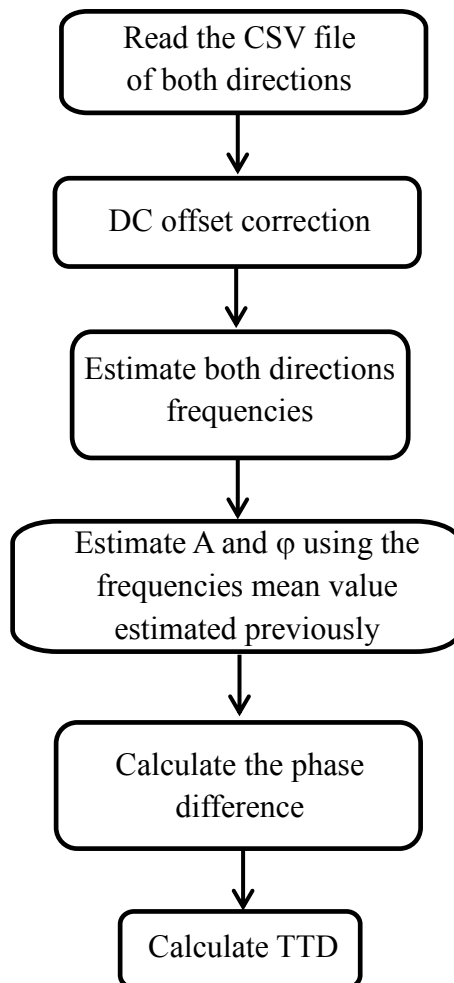


Fig. 4.10: Flowchart for computing the TTD

Chapter 5

TTD-jitter Reduction

5.1. Introduction

The purpose of sampling and digitizing the transmitted and received ultrasonic signals is to perform advanced signal processing and accurately extract the transient time difference (TTD). The continuous signal waveform is defined on the basis of a set of time-discrete samples over a specified period of time. However, clock jitter causes uncertainty in the sampling time during the data acquisition of ultrasonic waves. This leads to random fluctuations in the corresponding amplitude. Therefore, the recorded data are corrupted by noise and distortion. As the TTD is computed on the basis of a finite set of sampled data, such uncertainties in the sampling time produce random fluctuations of TTD measurements, known as the TTD-jitter.

The TTD-jitter in flow measurement has a huge impact on its accuracy. It can be experimentally evaluated by repeatedly performing the same measurement and using the same measurement setup under the same conditions.

This chapter investigates the TTD-jitter noise and its impact on the accuracy of flow meter measurement results. The approaches used in order to mitigate the TTD-jitter are also presented here.

5.2. The Effect of Sampling Jitter on TTD

In the sampling-process, the sampling time uncertainty (also called the sampling time jitter⁵) is the random fluctuations in time location of a given waveform sample. Correspondingly, this uncertainty in sampling time introduces errors in the amplitude of the ultrasonic signal. As illustrated in Figure 5.1, for a given sine wave of period T and peak-to-peak amplitude V_{pp} the sampling time jitter Δt causes a change in the measured value equal to $\Delta V = V_{pp} \pi \Delta t / T$ [46]. This contributes to the increase of the TTD-jitter. In the present application, the TTD-jitter refers to the dispersion of the measured TTD around the mean value (zero for no-flow). The latter is assumed to be a stationary Gaussian noise, which means that the standard deviation does not change over time. The TTD-jitter is thus defined by the mean value and the standard deviation.

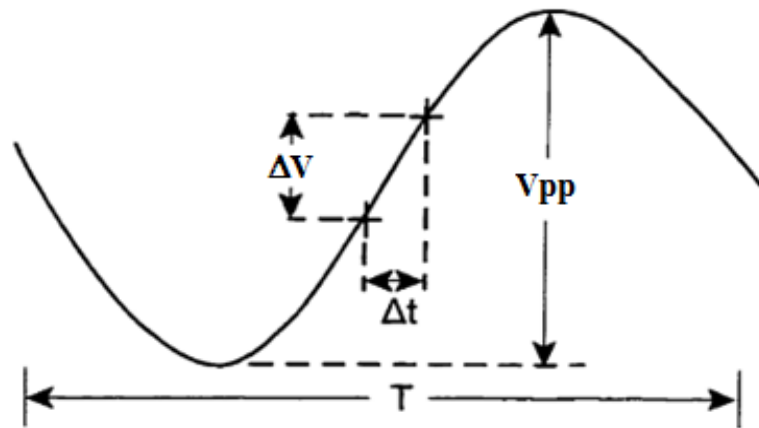


Fig. 5.1: Effect of the sampling jitter on measured value

Typically, the transducers are excited by a sinus burst of 70 cycles at 4 MHz frequency. The experimental results in Figure 5.2 show the last 19 periods of a transmitted signal superimposed upon each other. Figure 5.2.b shows a magnification of Figure 5.2.a. Interestingly, this figure shows that for consecutive periods of a measurement, the zero-crossings jump from one period to the next period statistically around the zero point. The Gaussian (or normal) probability distribution function can be used to statistically characterize the maximum time deviation of the periods around the zero point caused by the sampling time jitter. The maximum time deviation of the 19 consecutive periods around the zero point is about 374 ps, which corresponds to 6 the standard deviations ($\sigma = 62.4$ ps). Note that the standard deviation result is obtained by evaluating 19 time data

⁵Not to be confused with the TTD-jitter.

samples around the zero point shown in Figure 5.2.b applying the probability density function. The time deviation of the periods increases with increasing number of time data samples.

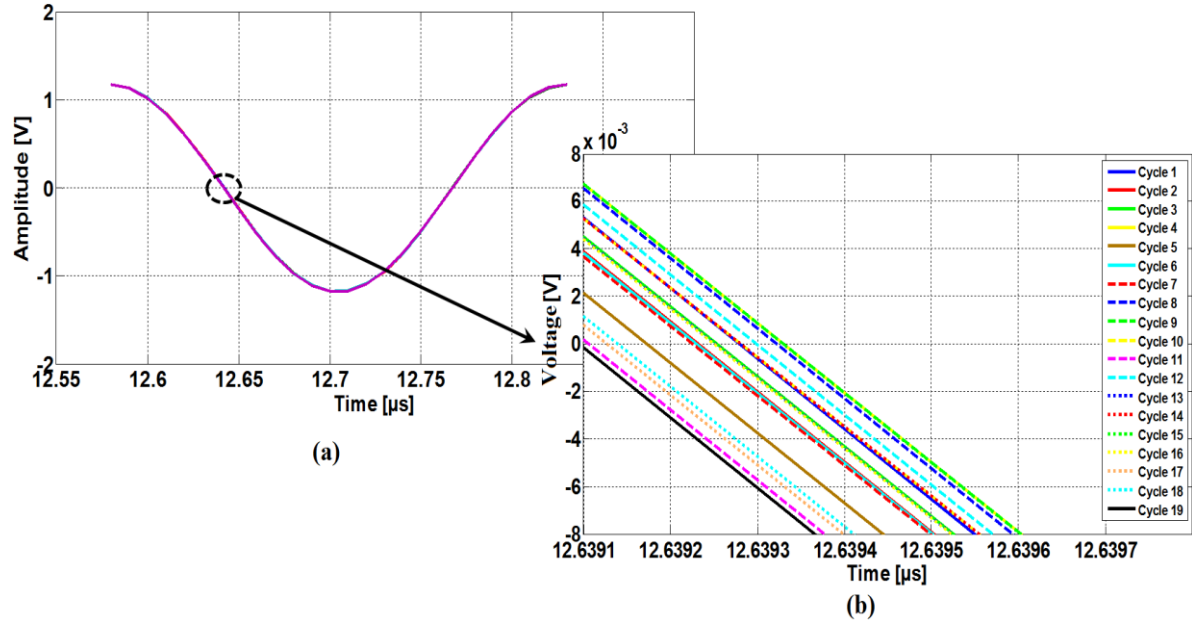


Fig. 5.2: Time deviation of the periods around the zero point:

(a) the last 19 periods of the transmitted signal superimposed upon each other,

(b) a magnified around the zero point

5.3. Sources of TTD-jitter

The TTD-jitter noise arises from many sources which contribute to the measurement uncertainty. These sources are uncorrelated and may originate from anywhere in the signal path from transmitting to receiving waveforms. Some of these sources are dedicated to the electronics associated with the transducers such as [39]:

- transmitter waveform phase noise or driving frequency instability of the transmitted signal due the function generator
- jitter in the sampling instance that may occur due to imperfect sample-and-hold circuit synchronization
- crosstalk between the cables
- irregularities in the transmission medium.

Other noise sources such as the effects of the side lobes also contribute to the TTD-jitter. As shown in Figure 5.3, most of the acoustic energy is transmitted perpendicularly from the piezoelectric disk. The main lobe is the lobe containing maximum sound pressure. This

lobe is calculated by finding the angle at which the sound pressure is halved [47]. The acoustic wave directivity⁶ is temperature-dependent [48], especially at the side lobes level, which increases from low temperature to high temperature. This can enhance the level of reverberation in the measuring pipe, producing undesired echoes acting as noise. This noise may corrupt the signal along the signal path, causing errors in the measured transit time.

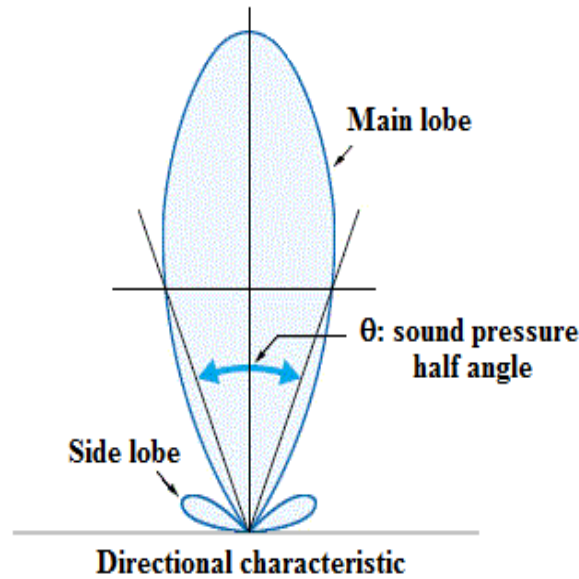


Fig. 5.3: An example of a sound directivity pattern [47]

5.4. TTD-jitter Reduction Technique

Since the recorded data of the received waveform are sampled with 50 MS/s, each period in the steady-state region contains around 13 sample points. The sine-fitting applied approach adjusts Equation (4.6) to the set of the recorded sampling data in order to extract the characterized parameters of the trace, namely its amplitude, phase, and the frequency. The following equation, obtained from Equation (4.4), is applied to compute the TTD using the upstream and downstream extracted phases (φ_{up} , φ_{down}):

$$TTD = \frac{\varphi_{up} - \varphi_{down}}{2\pi f}. \quad (5.1)$$

The precision to which the TTD is determined can be influenced by two parameters: the amplitude of the received signal and the number of the samples used in the fitting algorithm. Concerning the first parameter, there is a clear correlation between the TTD-

⁶ The acoustic directivity describes how the pressure of a sound wave is transmitted from a transducer.

jitter level and the amplitude of the received signal in the quiet region. In other words, the obtained TTD has a jitter that depends on the input dynamic range of the acquisition system. This is optimized by adjusting the gain of the two amplifiers (Figure 4.1), aiming to cover most of the input range of the ADC. The results shown in Figure 5.4 (carried out at room temperature, no-flow condition, $N = 250$ fitted samples, and different receiver voltages⁷ V_{RD1} and V_{RD2}) suggest that the increase of the voltage headroom in both directions reduces the TTD-jitter.

The used ADC has 14-bit resolution and an input full-scale range of ± 2.5 V⁸. The least significant bit (LSB) voltage can be expressed as:

$$V_{LSB} = \frac{V_{FSR}}{2^{N_{bit}-1}}, \quad (5.2)$$

where N_{bit} is the ADC's resolution in bits and V_{FSR} is the full-scale voltage range of the ADC. According to Equation (5.2), the ADC has a voltage resolution V_{LSB} of about 300 μ V. The dynamic range of data acquisition system (DR), which is the ratio of the maximum input voltage V_{FS} ⁹ (signal amplitude) to the minimum voltage V_{LSB} , can be expressed as:

$$DR[dB] = 20 * \log\left(\frac{V_{FS}}{V_{LSB}}\right). \quad (5.3)$$

Figure 5.5 illustrates the measurement precision (represented by the standard deviation) versus the dynamic range of the acquisition system. Note that the standard deviations are calculated from TTDs of 50 captured ultrasonic waveforms. It can be deduced on the basis of these results that high dynamic range of the acquisition system can be achieved using a high gain amplifier to cover the input full-scale range voltage ($V_{FSR} = 5$ V) of the ADC, which results in very low TTD-jitter.

⁷ The amplitude voltages V_{RD1} and V_{RD2} are estimated in the quiet region of both directions of received signals using sine-fitting

⁸ According to the datasheet of the used ADC (AD9648) [49], it achieves SINDR of 74.3 dB, SNR of 75.4 dB, and ENOB of 12-bit at 9.7 MHz.

⁹ V_{FS} refers to the full-scale sine wave of the received signal in the quiet region.

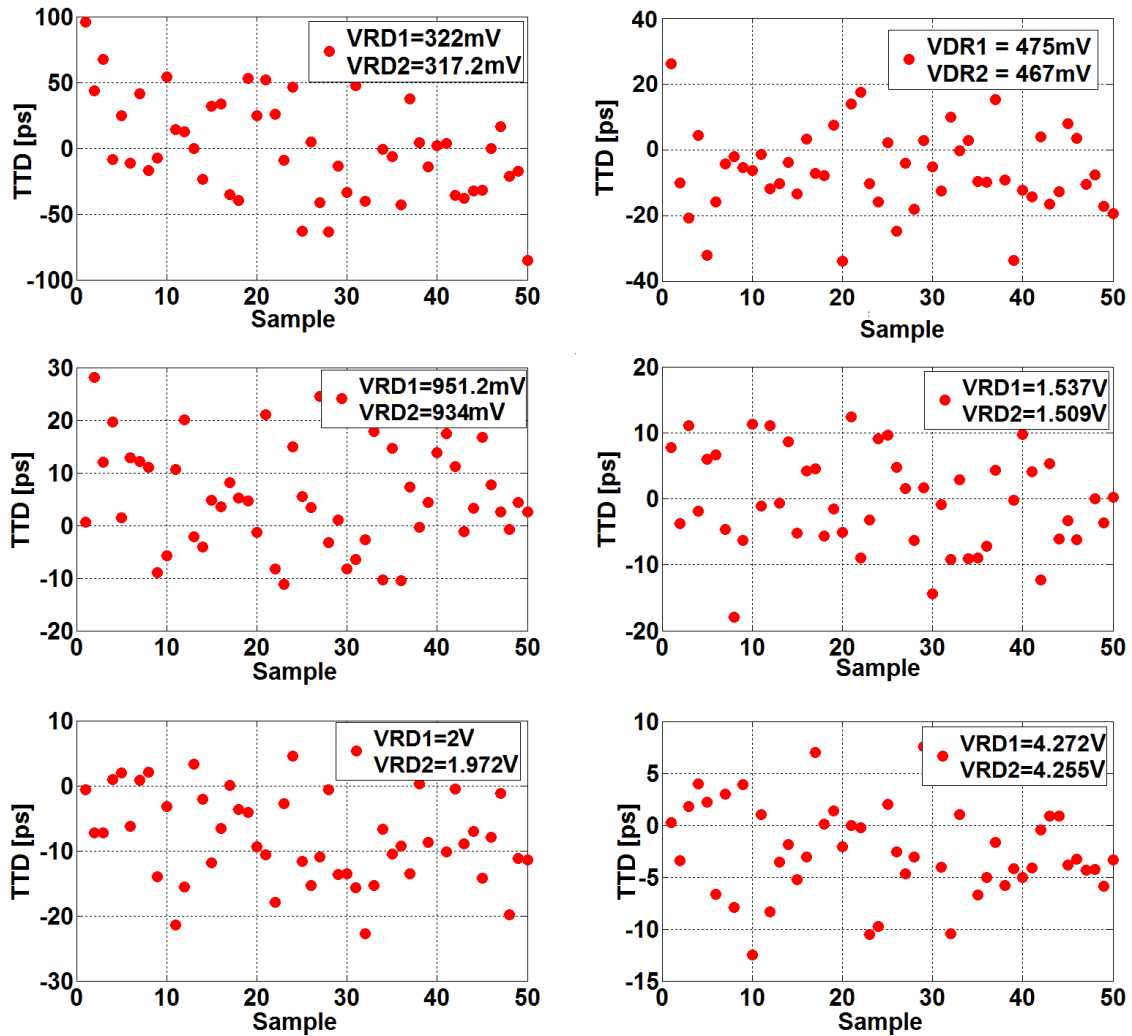


Fig. 5.4: TTD measured at different receiver amplitudes

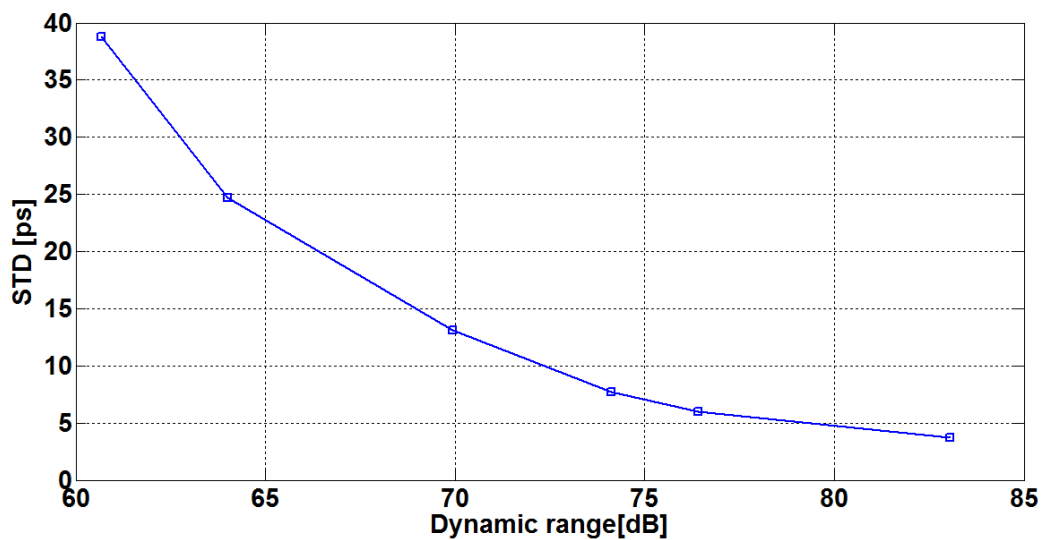


Fig. 5.5: The standard deviation of the transit time difference (TTD) versus the dynamic range of the acquisition system (N = 250 fitted samples)

As mentioned previously, the TTD-jitter can also be reduced by increasing the number of the signal samples that are used to adjust the sine-fitting parameters. Since the noise present at each sampling sequence is uncorrelated, a given number of samples N reduces the timing jitter values by a factor of \sqrt{N} (according to the averaging principle). This can mathematically be expressed as:

$$\sigma_{\bar{x}} = \frac{\sigma}{\sqrt{N}}, \quad (5.4)$$

where $\sigma_{\bar{x}}$ is the standard deviation error of the TTD (after averaging), σ is the standard deviation of the TTD, and N is the size of the samples.

Figure 5.6 depicts a single TTD measurement carried out at room temperature and no-flow conditions for different numbers of the fitted samples.

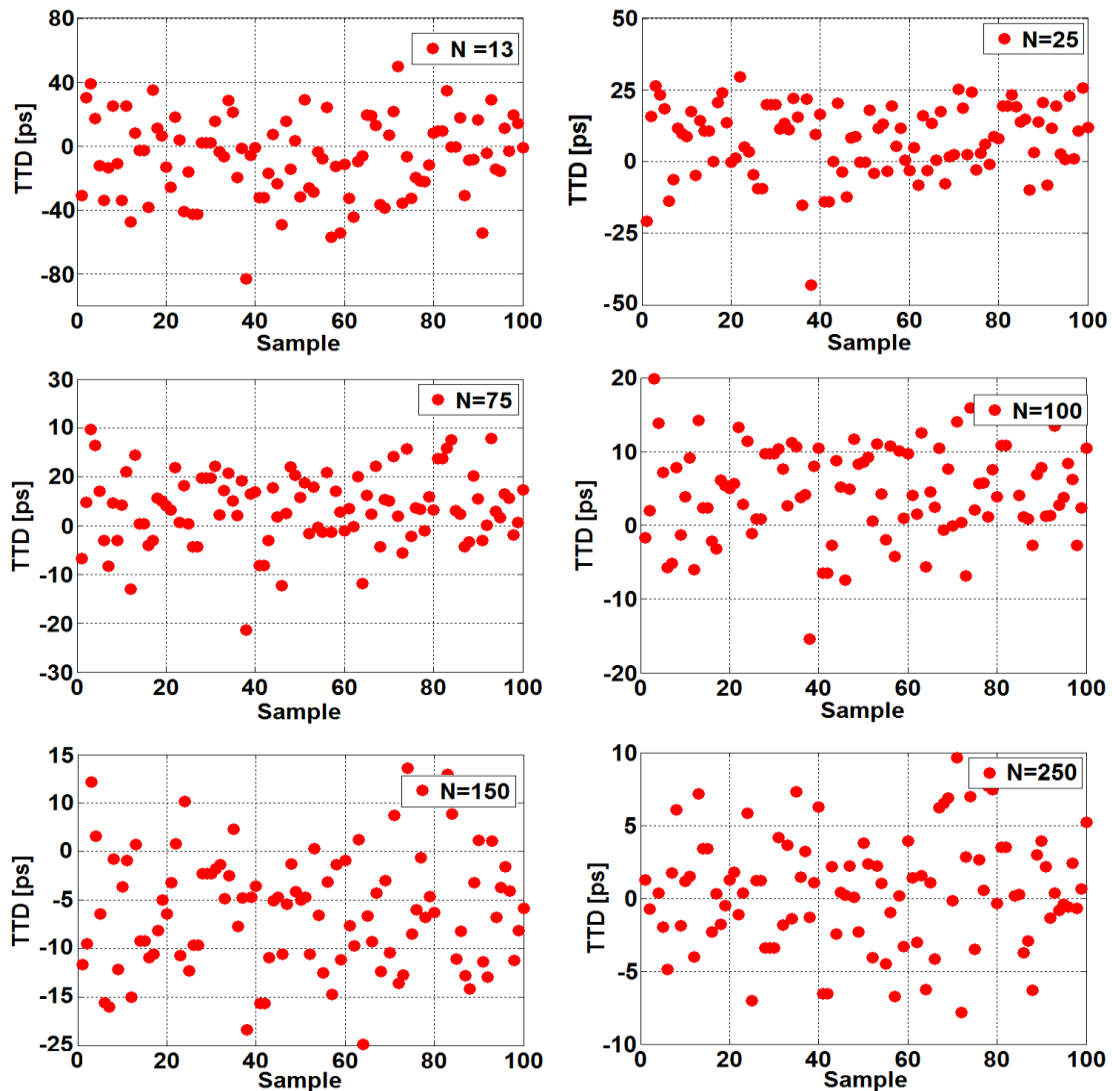


Fig. 5.6: TTD results measured at different numbers of fitted samples (N)

Figure 5.7 illustrates the measured TTD standard deviation (STD) versus the number of fitted samples as well as the theoretical limits estimated using Equation (5.4). It can be deduced on the basis of these results that the measured TTD-jitter exhibits the same behavior as the calculated one. In other words, as the number of samples increases, the standard deviation of the measured TTD decreases according to Equation (5.4).

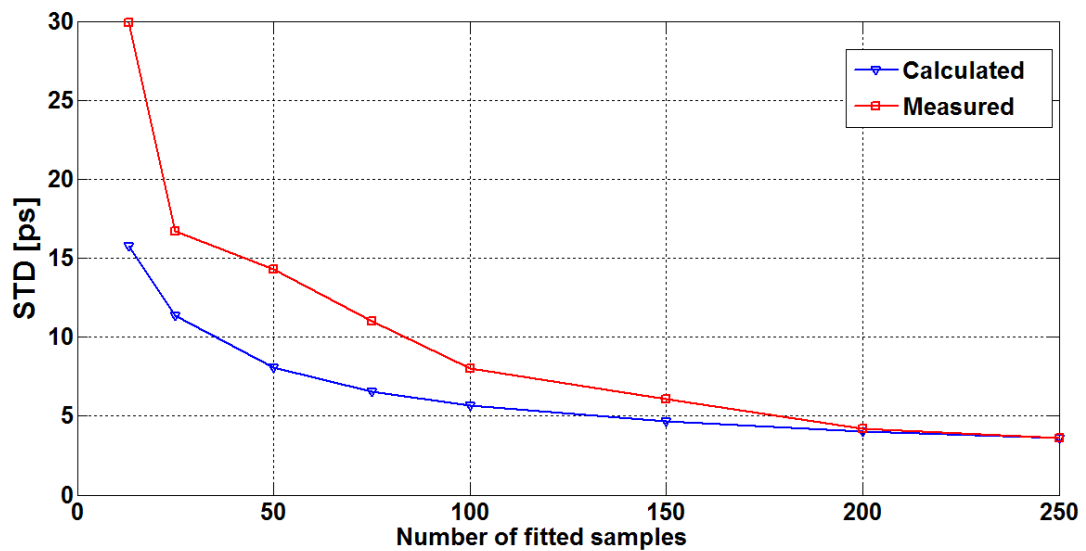


Fig. 5.7: The standard deviation of TTD versus the number of fitted samples (N)

Chapter 6

TTD-offset Cancellation

6.1. Introduction

As described previously, in the ideal case when there is no flow in the measuring pipe the upstream and downstream transit times should be identical. However, in reality this is not the case as there are many factors that prevent the ultrasonic signals (see Section 4.1) from reaching the receivers after exactly the same traveling time. Hence, any deviation of the measured transit time difference (TTD) from zero at no-flow conditions is referred to as a TTD-offset. This TTD-offset, which limits the minimum measured flow, presents a serious drawback in high accuracy measurements. Therefore, it is worthwhile to develop a theoretical analysis which provides a better understanding of the TTD-offset sources and their contributions in order to develop a measurement strategy that allows effective TTD-offset compensation.

6.2. Sources of TTD-Offset

In water flow meter applications, the environment temperature inside the measuring pipe may vary from ambient temperature to 80°C. This leads to a variation of the transducer's resonance frequency, which cannot withstand the change of the operating temperature [19] [50-52]. However, according to the harmonic oscillation model¹⁰, if a pair of transducers has different resonance frequencies, then the phase difference between the two steady-state parts of the received signals is different from zero as well. Figure 6.1 shows an example of two phase responses versus the driving frequency. This two plots of phase responses are obtained from the phase equation of the particular solution of a damped driven harmonic oscillator (Equation 3.10) for two transducers with different resonance frequencies (for this example, the resonance frequencies are $f_{r1} = 4$ MHz and $f_{r2} = 4.05$ MHz for the first

¹⁰ The analytic modeling of the piezoelectric transducer disk described in Chapter 3.

transducer and the second transducer, respectively). The difference between these two phases is shown in Figure 6.2, where it can be observed that within the resonance frequency range the phase difference is significantly different from zero. Thus, the zero flow error can drift according to the temperature changes, which can cause significant TTD-offset.

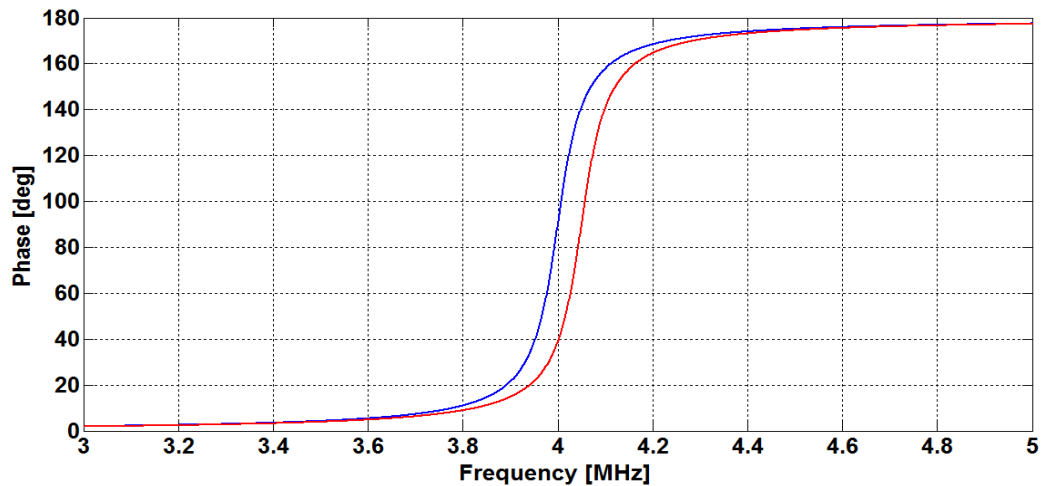


Fig. 6.1: Phase response versus driving frequency for two different transducers

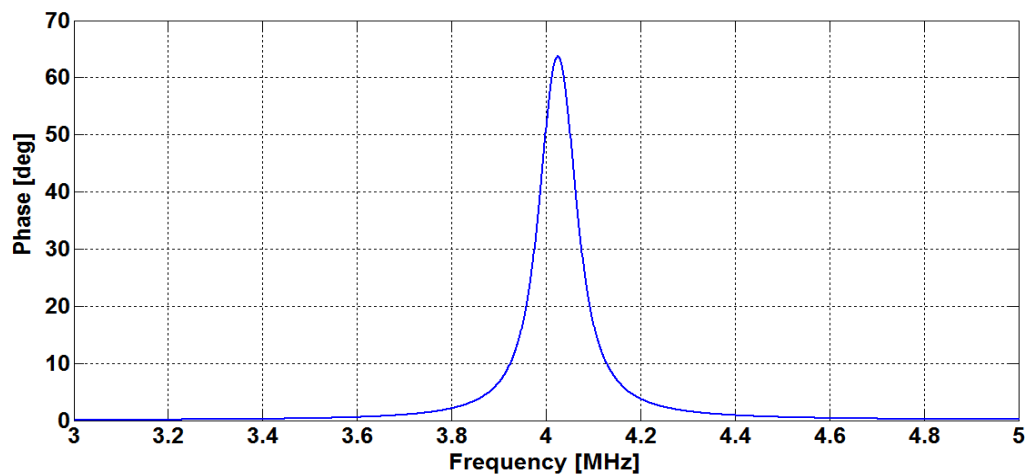


Fig. 6.2: Phase difference response versus driving frequency

6.3. The Impact of Temperature on the Transducer Resonance Frequencies

In order to predict what effect temperature changes have on the series and parallel resonance frequencies of the 4 MHz transducer pair, the variation of transmitter voltages (VTD_1 and VTD_2) with respect to the driving frequency is investigated experimentally (see Section 3.8). The experiment allows to obtain an approximate determination of both frequencies by estimating the maximum and the minimum transmitter amplitudes

measured at different temperatures. This experiment is carried out by exciting the transducers with a sinus burst of 70 cycles at a specified frequency in the range between 3.8 MHz and 5 MHz. The results illustrated in Figures 3.23, 6.3, and 6.4 demonstrate the variation of transmitter voltage amplitudes in both directions measured at ambient temperature ($\cong 25^\circ\text{C}$), 60°C , and 80°C , respectively, with respect to the driving frequency. Note that the measuring pipe is heated using a thermostat. It can be deduced from the obtained results that the frequency at which the amplitude becomes minimal (minimum impedance) is close to series resonance frequency f_s , whereas the frequency at which the amplitude becomes maximal (maximum impedance) is close to the parallel resonance frequency f_p . However, because the parameters of the two transducers are not identical, the variation of both amplitudes is also not identical. The temperature dependence of the resonance frequencies of the pair of 4 MHz transducers is summarized in Table 6.1.

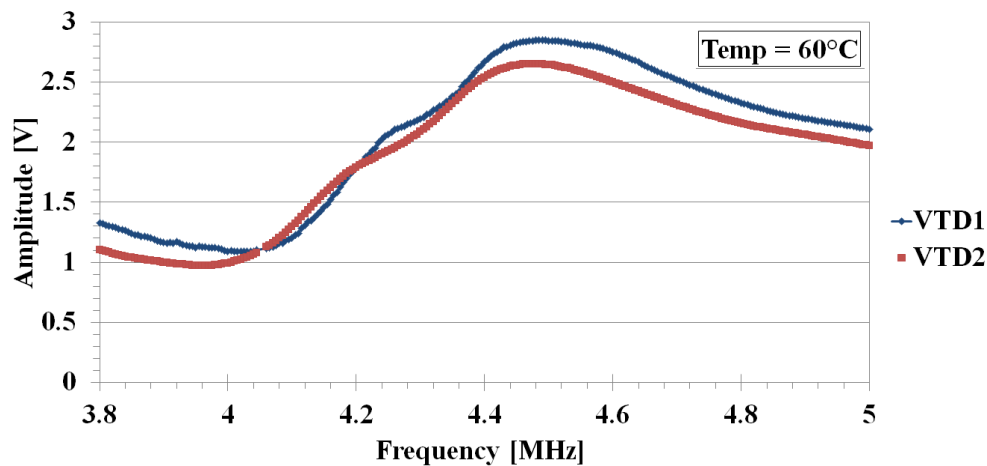


Fig. 6.3: Transmitter voltages versus driving frequency measured at 60°C

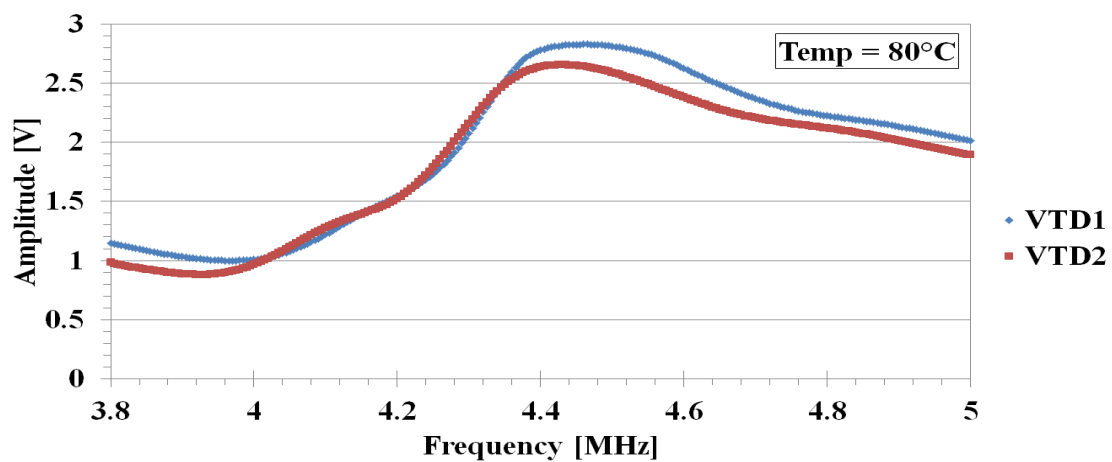


Fig. 6.4: Transmitter voltages versus driving frequency measured at 80°C

Temperature [°C]	Resonance frequency [MHz]			
	Transducer 1		Transducer 2	
	f_s	f_p	f_s	f_p
25°C	4.02	4.615	4.01	4.595
60°C	4	4.49	3.96	4.475
80°C	3.97	4.465	3.925	4.43

Table 6.1: The dependence of resonance frequencies on temperature

As shown in Figure 6.5, the series f_s and the parallel f_p resonance frequencies of the used transducer pair decrease as the temperature goes up. Regardless of the mismatch between transducers, the variation of the resonance frequency with the operating temperature range can cause a dissymmetry between the two directions of the ultrasonic signal paths. Thus, the temperature variation of the medium is the main reason for the zero flow TTD-offset drift.

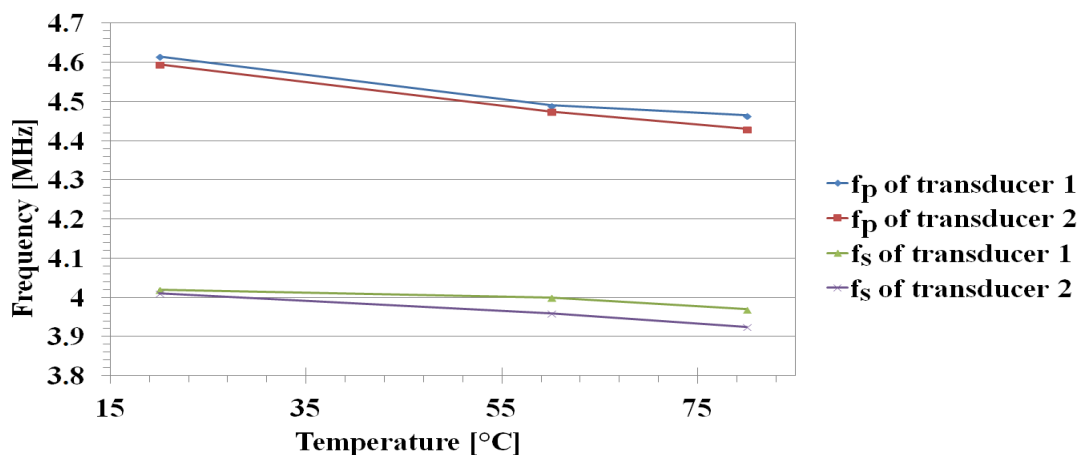


Fig. 6.5: The effect of temperature on the transducer resonance frequencies

6.4. Zero Flow TTD-offset Correction

As mentioned before, in order to eliminate the possibility that the meter detects a false flow under no-flow conditions, the upstream and downstream transit times should ideally be the same, although this may not be the case unless special precautions are taken. Due to the fact that every flow direction exhibits a slightly different electrical impedance compared to the other, there is a dissymmetry between upstream and downstream signal paths [7]. This effect provides a different amount of currents flowing through R_1 and R_2 (see Figure 4.1), and causes different amplitudes in the upstream and downstream transmitted signals. Figure 6.6 shows the result of the measurement carried out at room temperature and

no-flow conditions. Both transducers are excited with the same sinus burst at 4 MHz forced frequency. The plotted curves show that the measured difference between the two amplitudes of the transmitted signals is about 250 mV.

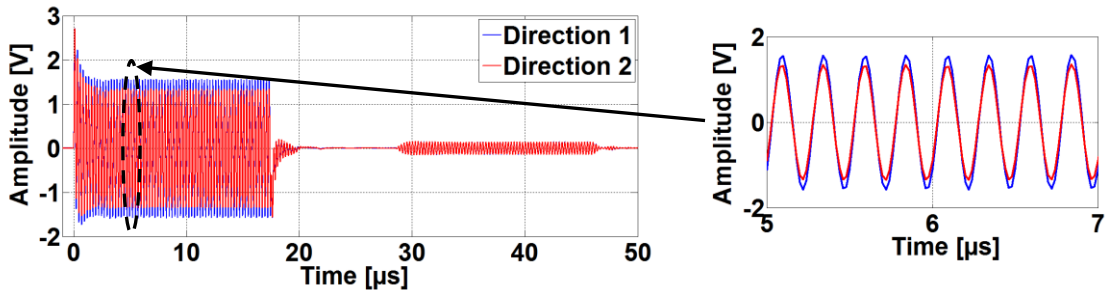


Fig. 6.6: Acquired ultrasonic signals in the upstream and downstream directions (measured at 4 MHz driving frequency)

By computing the phase shifts ϕ_{t1} and ϕ_{t2} between the excitation and the sound wave on both transducers for transmitted signals, a delay time difference of -2.4 ns is obtained between transmitted signals in both directions. This relatively high starting delay time difference can be explained by upstream and downstream unmatched electrical impedance values, which lead to the difference between the two transmitter amplitudes (of about 250 mV). The 250 mV transmitter amplitude difference shown in Figure 6.6 results in about 150 ps zero flow TTD-offset.

In order to effectively eliminate TTD-offset at no-flow conditions, it is necessary to match the upstream and downstream electrical impedance of both transducers and their associated electronic to reach a highly symmetrical signal paths. According to the literature [25], the electrical impedance of a transducer can be controlled by a driving frequency. We have used this feature to eliminate the electrical impedance mismatch between both directions because a well-matched upstream-downstream signal path reduces the transmitter amplitude difference and results in a very small zero flow TTD-offset.

By changing the sinus burst frequency from 4 MHz to 4.19 MHz, the 150 ps zero flow TTD-offset measured previously is substantially reduced to less than 5 ps (Figure 6.7). Moreover, comparing the amplitudes of the transmitted signals depicted in Figures 6.6 and 6.7, it can be observed that the difference between the two transmitter amplitudes is reduced from 250 mV measured at 4 MHz to less than 15 mV, which is achieved by exciting the transducers at 4.19 MHz driving frequency under the previously mentioned

conditions. In addition, the delay time difference of -2.4 ns achieved between transmitted signals in both directions at 4 MHz is reduced to -664 ps at 4.19 MHz driving frequency. Therefore, choosing an appropriate driving frequency within the resonance frequency range of the transducer is the key to cancel the long-term drift of the TTD caused by temperature variations.

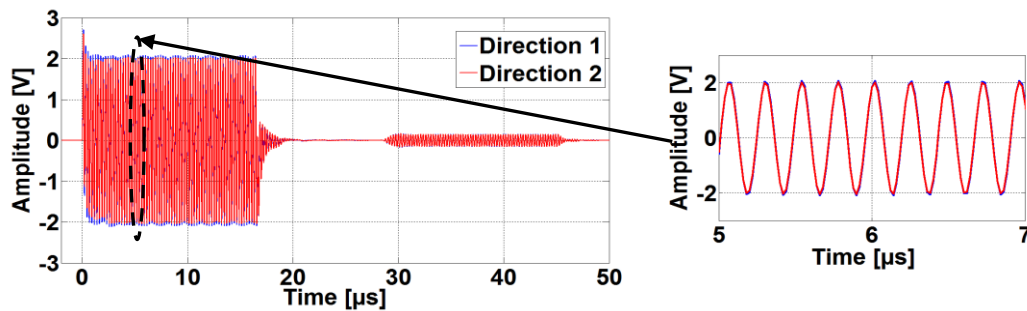


**Fig. 6.7: Acquired ultrasonic signals in the upstream and downstream directions
(measured at 4.19 MHz driving frequency)**

Figure 6.8 shows TTD measurement results obtained in a driving frequency range from 4 MHz to 5 MHz with 5 KHz step variation at room temperature and no-flow conditions. The result shows that within the resonance frequency range of the two transducers TTD-offset compensation can be achieved at 4.185 MHz driving frequency. Figures 6.9 and 6.10 represent the same measurements as before carried out at 60°C and 80°C temperature, respectively, and they clearly show that these TTD-offsets compensation are achieved at different driving frequencies (about 4.095 MHz for 60°C and about 4.075 MHz for 80°C) due to the fact that the resonance frequency of the transducer is changing as a function of temperature as well.

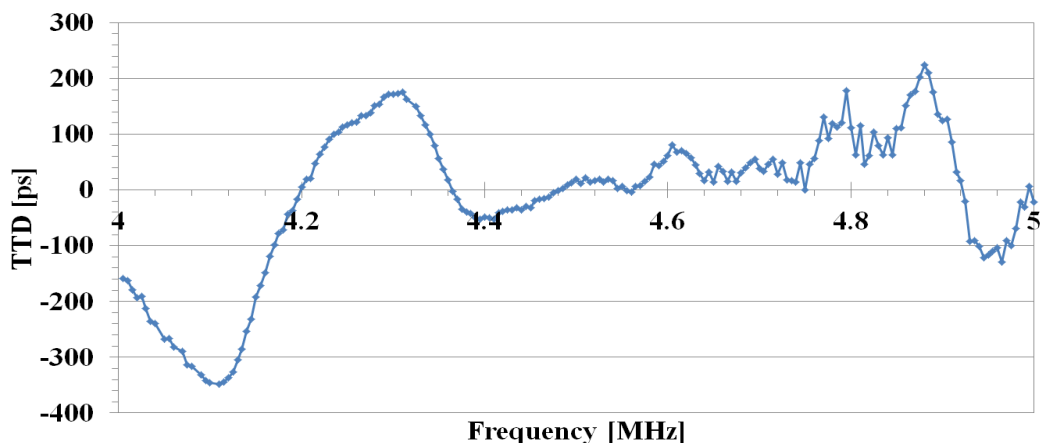


Fig. 6.8: TTD versus driving frequency measured at ambient temperature

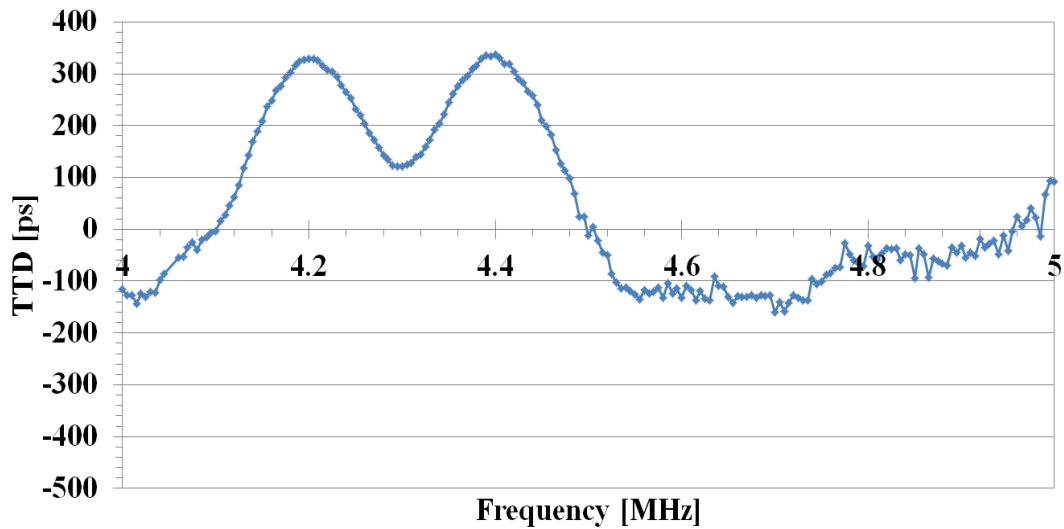


Fig. 6.9: TTD versus driving frequency measured at 60°C

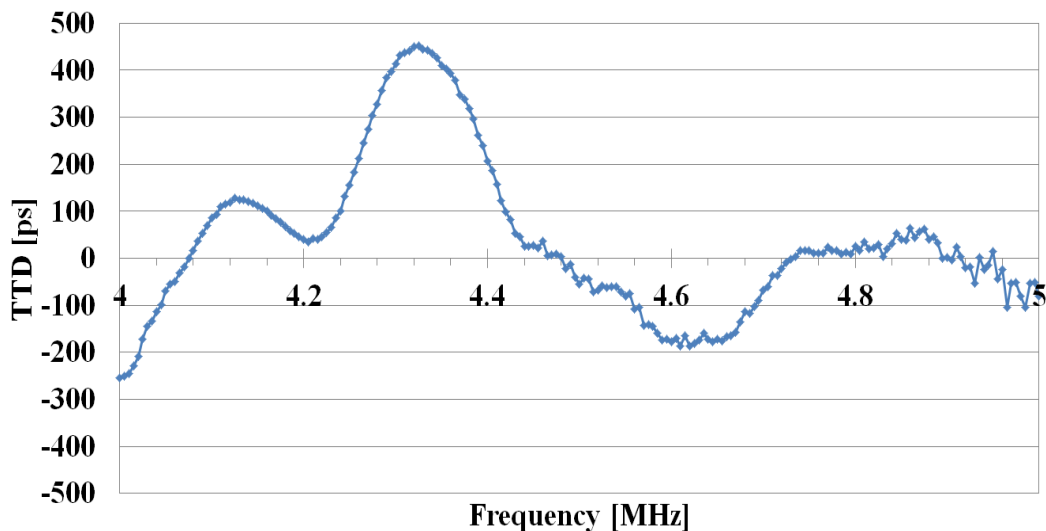


Fig. 6.10: TTD versus driving frequency measured at 80°C

To sum up, for a successful TTD-offset compensation it is necessary to adopt the two following strategies:

- Offline TTD-offset calibration must be performed in the manufacturing process in order to provide a table with driving frequencies and their corresponding temperature within a temperature range from ambient temperature to 80°C.
- Online TTD-offset calibration must be performed with control algorithms that use adequate driving frequency suitable to compensate the TTD-offset according to the measured temperature inside the measuring pipe.

6.5. Temperature Dependence of the TTD-offset Calibration

As mentioned before, choosing an appropriate driving frequency can drastically reduce the zero flow TTD-offset. To attain automatic compensation, one needs to accurately set a suitable driving frequency to eliminate the TTD-offset caused by the temperature variation inside the pipe. In order to ensure repeatability or precision of the driving frequency used to compensate the TTD-offset, several experimental measurements are performed over three months at four randomly chosen temperatures (35°C, 60°C, 70°C, and 80°C). These experiments have led to the results illustrated in Figures 6.11 and 6.12, where the heating up and cooling down of the pipe is done by means of a thermostat. As it can be seen in Figure 6.11, the first experiment starts by adjusting the temperature inside the pipe to 35°C; the calibration of the TTD-offset to zero is reached at 4.153 MHz driving frequency. While maintaining the same driving frequency, the heating up of the pipe to 80°C increases the TTD-offset to about 270 ps. By changing the driving frequency from 4.153 MHz to 4.075 MHz, the TTD-offset is calibrated once again to nearly zero value. The cooling down of the pipe from 80°C back to 35°C at the same driving frequency decreases the TTD-offset to about -320.3 ps, while the TTD-offset reaches again zero at the same starting excitation frequency (4.153 MHz) since in that moment the measured temperature inside the pipe is again 35°C. The relatively high measured TTD-jitter that can be seen clearly in the measured plots, especially at 35°C, can be explained by the fact that a full-scale voltage range of the ADC is not reached completely. This happens because the received signal attenuation is normally proportional to the viscosity of the water, which decreases with increasing temperature. Therefore, the gain of the amplifier is controlled by four resistances (see Figure 7.1) in order to bring the received signal to a level that is high enough to resist the attenuation that it will be subjected to.

The same setup is used to perform the second experiment, apart from the fact that the maximum reached temperature is 60°C instead of 80°C. It can be seen from Figure 6.12 that heating up and cooling down the pipe from 35°C to 60°C and from 60°C to 35°C, respectively, provides TTD-offset values that vary between -220.3 ps and 338.8 ps.

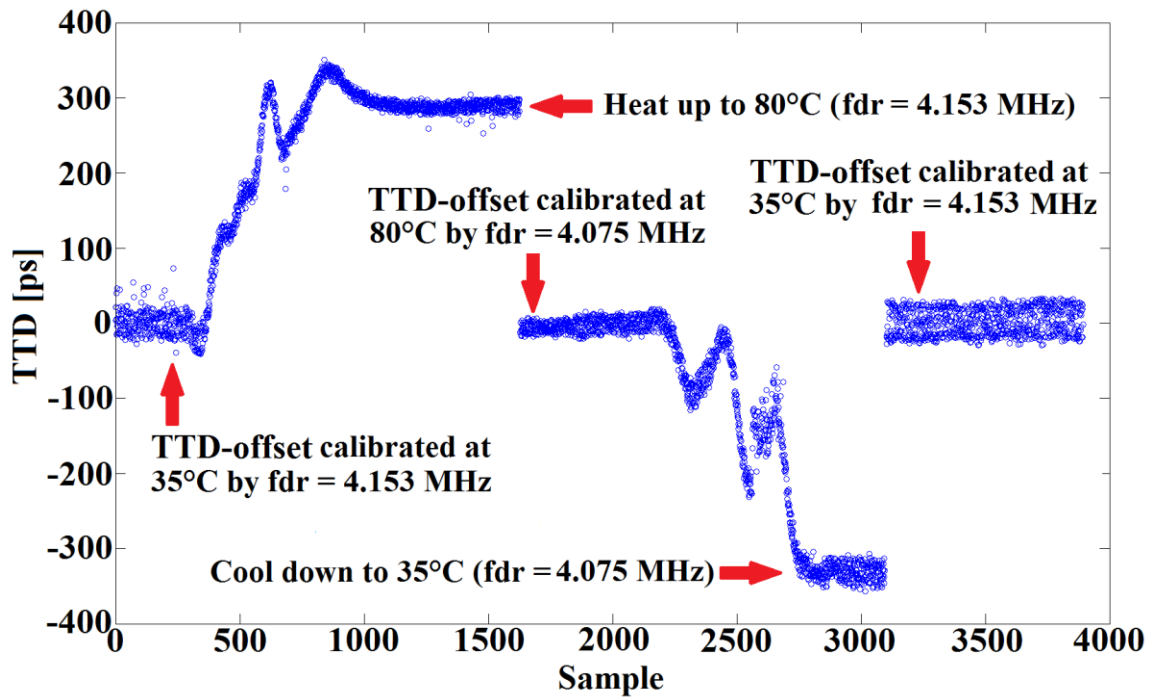


Fig. 6.11: TTD measurements performed over a temperature range from 35°C to 80°C

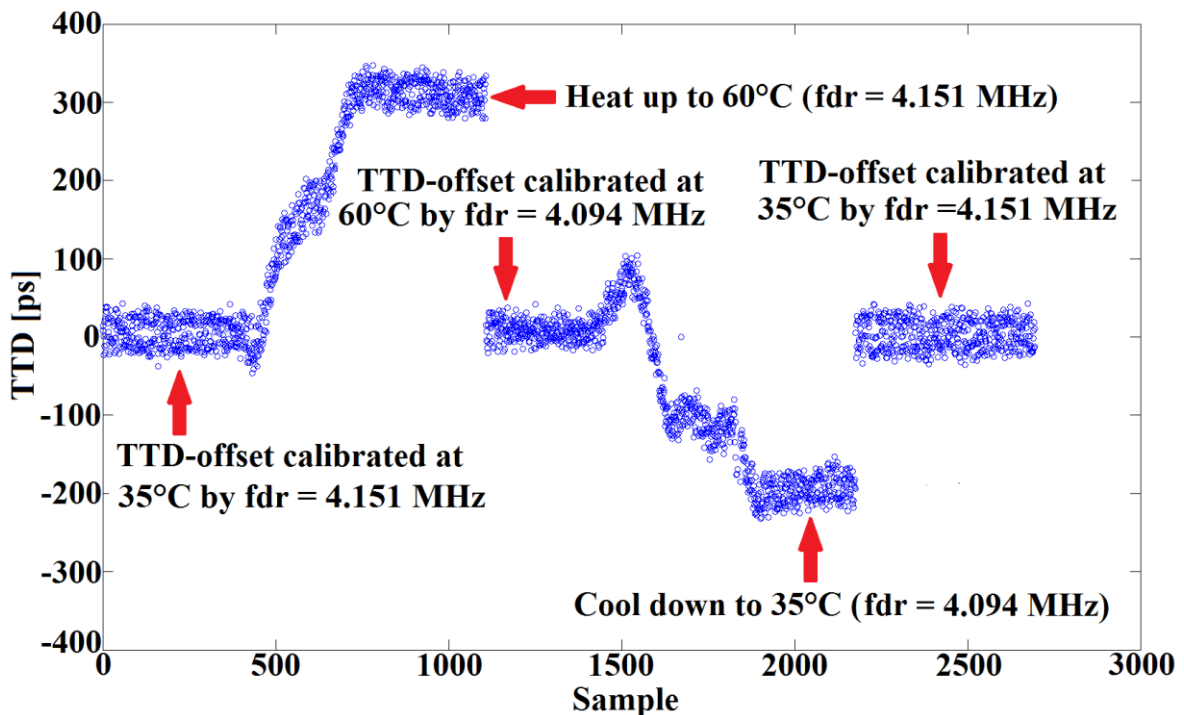


Fig. 6.12: TTD measurements performed over a temperature range from 35°C to 60°C

The results showing the temperature dependence of the driving frequency are obtained in five measurements carried out over a three-month period (see Table 6.2 and Figure 6.13).

Taking in consideration the suppression of the zero flow error, it can be noticed that the driving frequency at which the two transducers are excited is strongly influenced by the temperature. Therefore, we have shown that there is a clear, simple, stable, and reliable relation between the required excitation forced frequency and temperature.

Note that the measured driving frequencies with respect to the temperature reported in Table 6.2 change from one pair of the transducers to the other.

<i>Temperature [°C]</i>	<i>Driving frequency [MHz]</i>				
	<i>1st measurement</i>	<i>2nd measurement</i>	<i>3rd measurement</i>	<i>4th measurement</i>	<i>5th measurement</i>
35°C	4.152	4.153	4.151	4.154	4.152
60°C	4.098	4.098	4.097	4.096	4.097
70°C	4.088	4.089	4.088	4.087	4.085
80°C	4.076	4.073	4.073	4.072	4.071

Table 6.2: Temperature dependence of the driving frequency

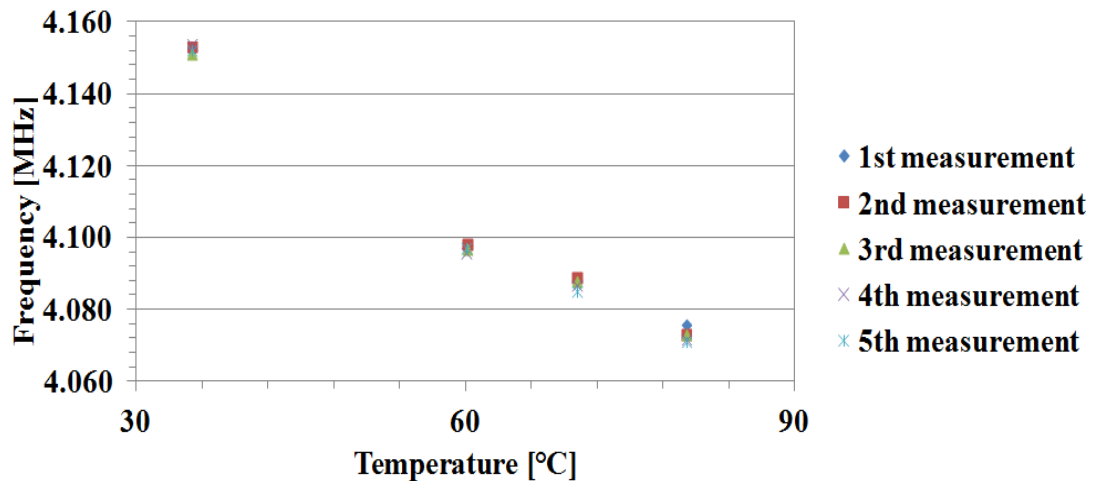


Fig. 6.13: Temperature dependence of the driving frequency used for the zero flow TTD-offset compensation

Chapter 7

Results and Analysis

7.1. Introduction

In this chapter, we demonstrate a practical application of the developed measurement methodology described in the previous chapter. Hence, the electronic system design introduced in Chapter 4 and the software algorithm used for signal processing are described in more detail. Afterwards, the experimental results are presented and analyzed. This analysis allows to highlight the robustness of TTD-jitter reduction and TTD-offset correction methodologies, developed in this thesis. Note that all measurement results reported in this chapter are performed at no-flow conditions within a specified temperature range from ambient temperature to 80°C

Figure 7.1 illustrates the electronic instrumentation system utilized to perform the ultrasonic measurement with significantly improved accuracy. The designed electronics and the software algorithm written in Matlab are capable of handling automatic measurement repetition, providing all control sub-programs, namely, the control of the function generator and analog discovery device.

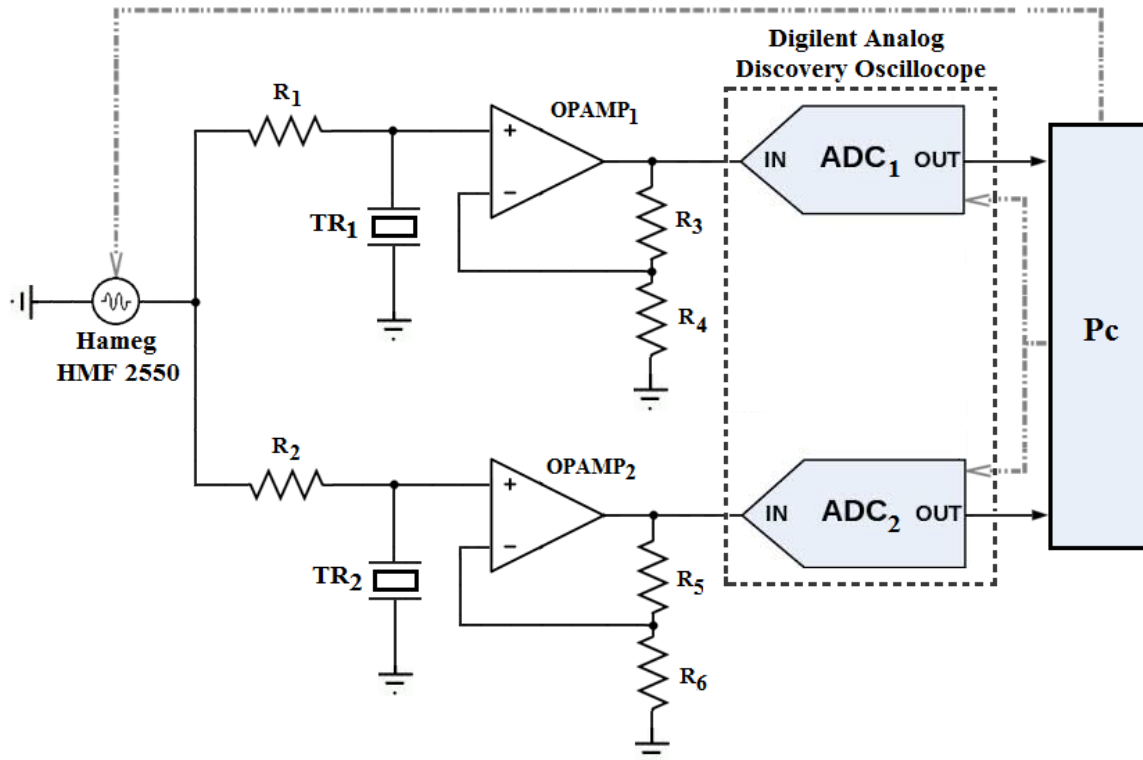


Fig. 7.1: Block diagram of the experimental setup

7.2. Hardware Design

The hardware elements of the experimental setup presented in Figure 7.1 are:

- An arbitrary waveform generator, which generates a sinusoidal burst of a finite number of cycles in order to excite the transducers.
- A pair of 4 MHz transducers located in the flow meter pipe, which are capable of transmitting and receiving an ultrasonic signal.
- DC source to power the low-noise amplifiers, which are used to amplify the voltage levels of the two received signals. Amplifiers gain is controlled by four resistors R_3 , R_4 , R_5 , and R_6 in order to reach 5 V full-scale voltage of the ADC.
- Digital oscilloscope, which has dual-channel, 14-bit ADCs for digital signal acquisition.
- An embedded (PC) software algorithm written in Matlab handles automatic TTD measurement repetition.
- Additionally, the flow meter pipe is put in a water bath with a thermostat to regulate the temperature of the transducers at given levels, assuming that the temperature of the transducer can be considered to be the same as the temperature of still water filling in the pipe.

7.3. Software Algorithm

Completely automatic measurement process is achieved through the developed software algorithm, which is used to automate manual tasks such as the configuration of the function generator and the digital oscilloscope to output the desired signal and save numerical data, respectively. The algorithm is also used to compute TTD and compensate the TTD-offset error if necessary. This automatic procedure is summarized in Figure 7.2, and it mainly consists of the following four sub-algorithms:

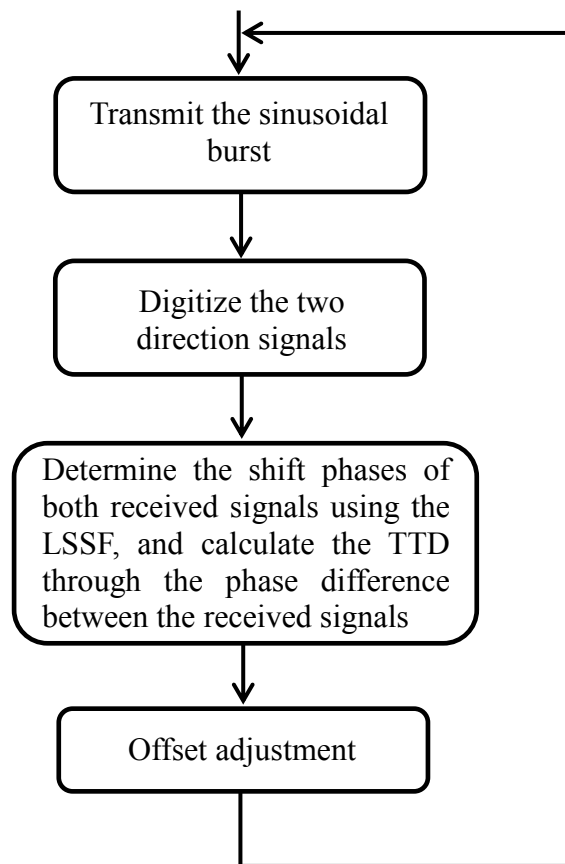


Fig. 7.2: Flowchart of the automatic measurement repetition

- A sub-algorithm controls the arbitrary waveform generator in order to generate sinusoidal burst.
- A sub-algorithm controls the two 14-bit ADCs in order to digitize the upstream and downstream signals.
- The sub-algorithm described in Section 4.6 is used to compute the TTD. The proposed method described in Chapter 5 is applied to attain reduced TTD-jitter.
- The last sub-algorithm is used to check whether the TTD-offset tends towards zero value or not.

- If the TTD-offset is not approximately equal to zero, the adjustment of the TTD-offset to zero is performed by choosing an appropriate excitation frequency (see Section 6.5), which is capable of avoiding the TTD-offset error.

7.3.1. Transmission of the Sinusoidal Burst

A sinusoidal burst of 70 cycles simultaneously excites the two transducers over a time period of 100 ms at a driving frequency of 4 MHz (17.5 μ s burst length) after the power up of the system. The automatic configuration of the arbitrary waveform generator is performed using the algorithm shown in Figure 7.3. The transmission procedure starts by opening the serial port so that the communication between the PC and the function generator can be enabled. All burst signal parameters (function, amplitude, frequency, the number of cycles, and period) must be specified in the program in order for them to be sent to the function generator through the serial port.

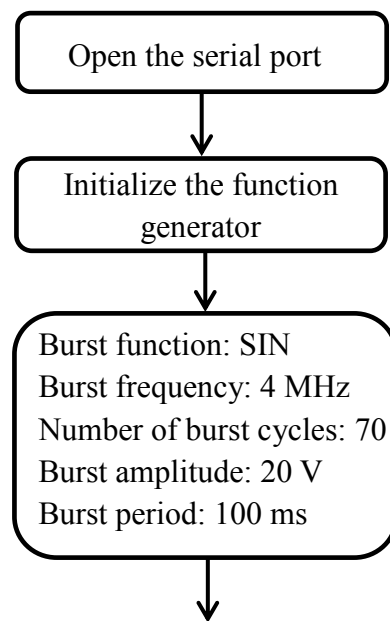


Fig. 7.3: Configuration of the function generator

7.3.2. Digitizing the Two Direction Signals

The two 14-bit ADCs of the digital oscilloscope operate up to 100 MHz maximum sampling rate. The trigger controls enable us to capture a stable waveform to be digitized and saved into a file containing numerical data regarding time and amplitude. One of the channels is used as a trigger source, where the trigger level and slope controls provide the

basic trigger point definition. Therefore, the slope control, which determines whether the trigger point is on the rising or the falling edge of the indicated signal, must be indicated in the control software algorithm depicted in Figure 7.4 in such a way that the system can deliver direct digital signals via the two integrated USB powered ADCs. The capture of a single-shot waveform is controlled by triggering; thereafter, the performed acquisitions are transferred to the PC in CSV format via USB with the maximum sample storage length of 8192 samples in order to be processed in Matlab.

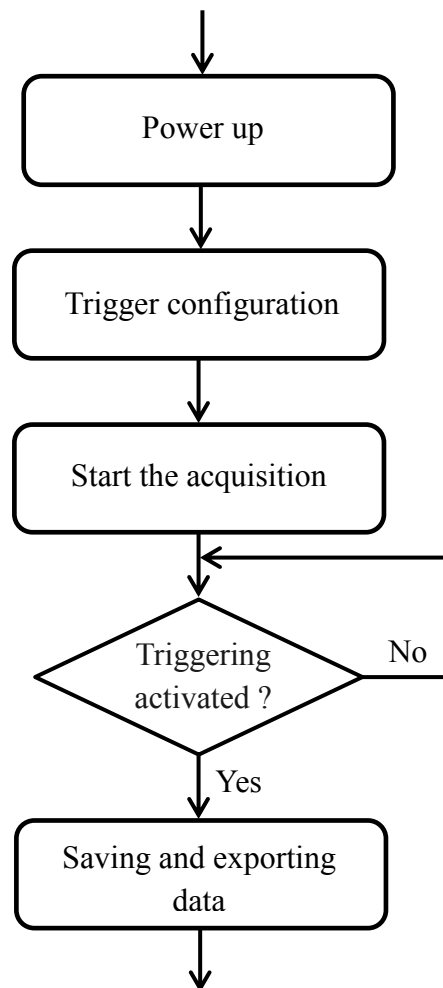


Fig. 7.4: The acquisition of both direction signals

7.3.3. TTD-Offset Cancellation Algorithm

The TTD-offset compensation strategy presented in Chapter 6 can be accomplished automatically by using an algorithm. This compensation is done with respect to the temperature of the medium around the transducers (see Section 6.5) in order to extract the required driving frequency that corresponds to the temperature of the medium (Table 6.2) so that the TTD-offset error can be compensated. Choosing of the correct driving

frequency can be done accurately by first determining the temperature of the water inside the measuring pipe. The measurement software system includes a conceptual TTD-offset compensation algorithm depicted in Figure 7.5, which allows continuous detection and compensation of the zero flow TTD-offset error.

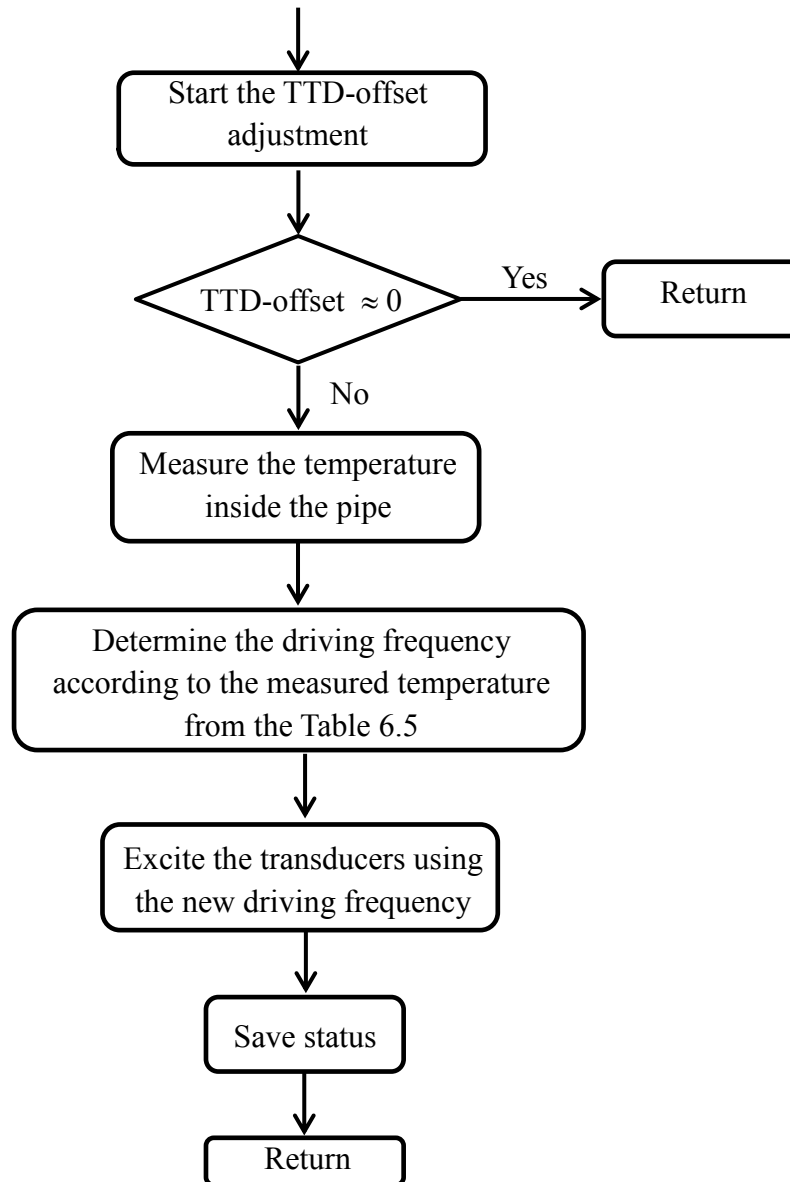


Fig. 7.5: Compensation of the TTD-offset

The TTD-offset compensation algorithm is executed immediately after computing the TTD. This algorithm starts by comparing the obtained TTD value to zero. If the TTD-offset is almost equal to zero, the new status information (driving frequency) is stored in the PC buffer to be used to excite the transducers again (i.e., it is the return to the transmission of the sinusoidal burst sub-algorithm). However, if the TTD-offset is different from zero, the adjustment of the TTD-offset must be performed by choosing the correct

driving frequency that corresponds to the measured water temperature around the transducers. This driving frequency, which can be used as new transmission frequency, is obtained from Table 6.2. Thereafter, the new driving frequency is stored and used to excite the transducers (i.e., it is the return to the transmission of the sinusoidal burst sub-algorithm).

7.4. TTD-offset Compensation Evaluation

In order to evaluate the offset compensation described in Chapter 6, the measurements are carried out using a 4 MHz flow meter pipe at no-flow conditions. As mentioned above, the two received signals are sampled at 50 MS/s, around 13 samples per period. Since the TTD-jitter can be reduced by a factor of \sqrt{N} (see Section 5.4), the TTD value is evaluated on the basis of 250 samples taken from the last 20 cycles in the steady-state region for both received signals. For each measurement setup, the TTD is computed several times with a repetition rate of about 1.6 s. Figure 7.6 shows that at 35°C when the transducers are excited at 4 MHz driving frequency, the average value of TTD-offset is approximately -370 ps and the value of peak-to-peak TTD-jitter is 30 ps. The TTD-jitter measurement precision, which refers to the standard deviation, is about 6 ps. The standard deviation is calculated from TTDs of 250 captured ultrasonic waveforms. In order to check the validity of our TTD-offset cancellation method, the first chosen 4 MHz frequency is changed to 4.153 MHz according to Table 6.2, considering that the temperature inside the measuring pipe is 35°C. Therefore, the measured -370 ps TTD-offset value is reduced to almost zero as shown in Figure 7.7.

Since the dynamic range of the acquisition system considerably influences TTD-jitter performance, it is necessary to use controllable gain amplifiers in order to reach the maximum amplitude of the received signal and therefore to cover input full-scale range voltage ($V_{FSR} = 5V$) of the ADC. However, as expected, the two voltage amplitudes measured in the quiet region of both received signals increase along with the temperature due to the fact that the viscosity of water decreases as the temperature goes up. This can be deduced from the results shown in Figure 7.8. This test is performed by changing the temperature of the thermostat from 80°C to 35°C.

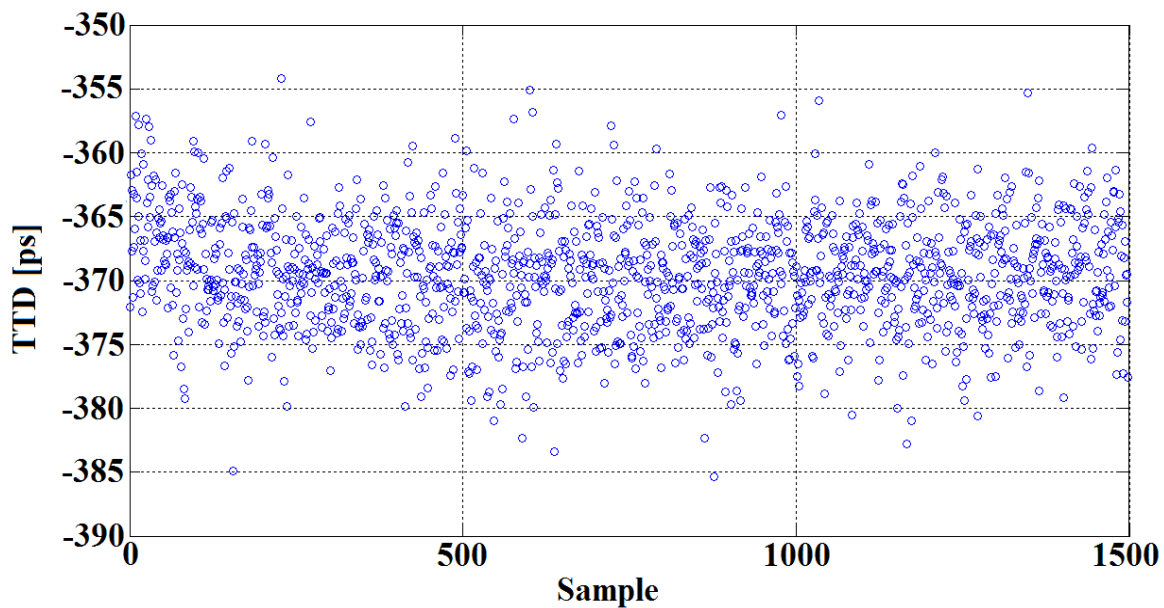


Fig. 7.6: Uncompensated zero flow TTD-offset measured at 35°C

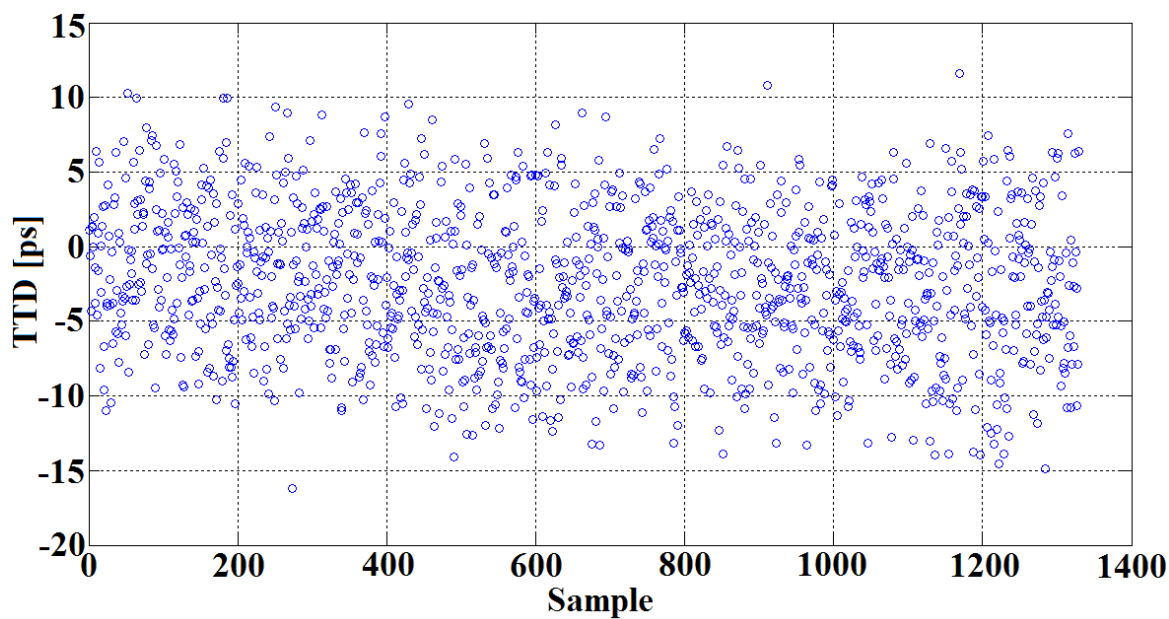


Fig. 7.7: Compensated zero flow TTD-offset measured at 35°C

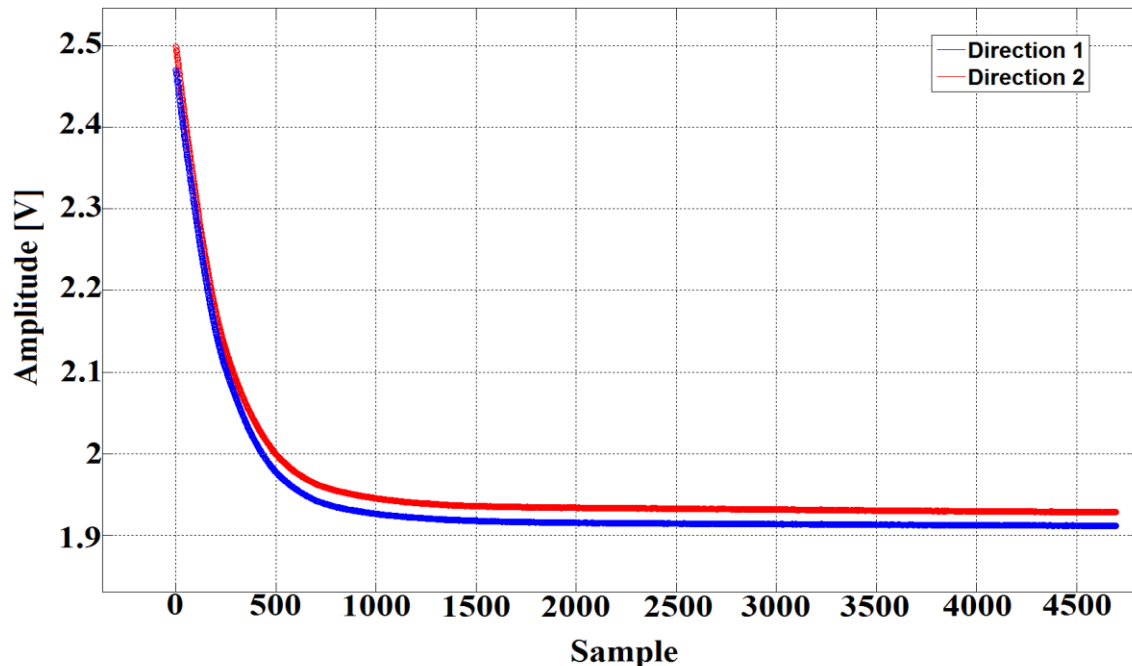


Fig. 7.8: Two received amplitudes measured over a temperature range from 80°C to 35°C

7.5. The Effect of Temperature on TTD-offset Measurements

Since the temperature is the main cause of the TTD-offset, additional TTD measurements are carried out at different temperatures (ambient temperature, 60°C, and 80°C), always using the 4 MHz flow meter pipe. The first result is illustrated in Figure 7.9, where the TTD measurements are performed continuously over 6 hours at ambient temperature, and the zero flow TTD-offset is adjusted only at the beginning by applying a driving frequency of about 4.180 MHz. In this result, the deviation from zero of the TTD-offset value is less than 50 ps over the whole measurement time. This is due to about 3 to 6°C variation of the ambient temperature during the measurement period.

Under the same conditions as shown in Figure 7.9, experimental measurements are performed at differently-regulated temperatures. Figures 7.10 and 7.11 depict the TTD measurements performed at 60°C and 80°C, respectively. According to Table 6.2, the TTD-offset cancellation is reached by setting the driving frequencies to 4.098 MHz at 60°C and 4.075 MHz at 80°C. As mentioned previously (see Section 7.4), the relatively high peak-to-peak TTD-jitter of 30 ps measured at 35°C can be explained by the fact that the received signals are not amplified enough to cover the dynamic range of the of the acquisition system. However, the peak-to-peak TTD-jitter is reduced to 20 ps and 15 ps when

measured at 60°C and 80°C, respectively. This is due to the fact that the received signal attenuation is proportional to the viscosity of the water, which decreases with increasing temperature as shown in Figure 7.8. The standard deviation (calculated from TTDs of 250 captured ultrasonic waveforms) of the TTD-jitter decreases from 6 ps at 35°C to 4 ps at 80°C.

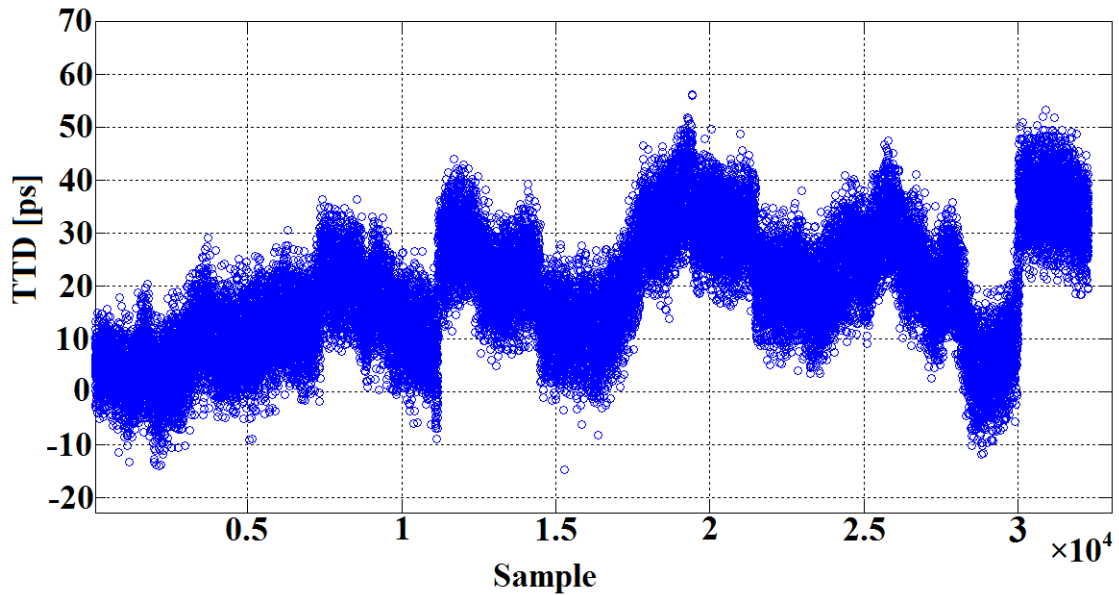


Fig. 7.9: TTD measurements performed over six hours at ambient temperature

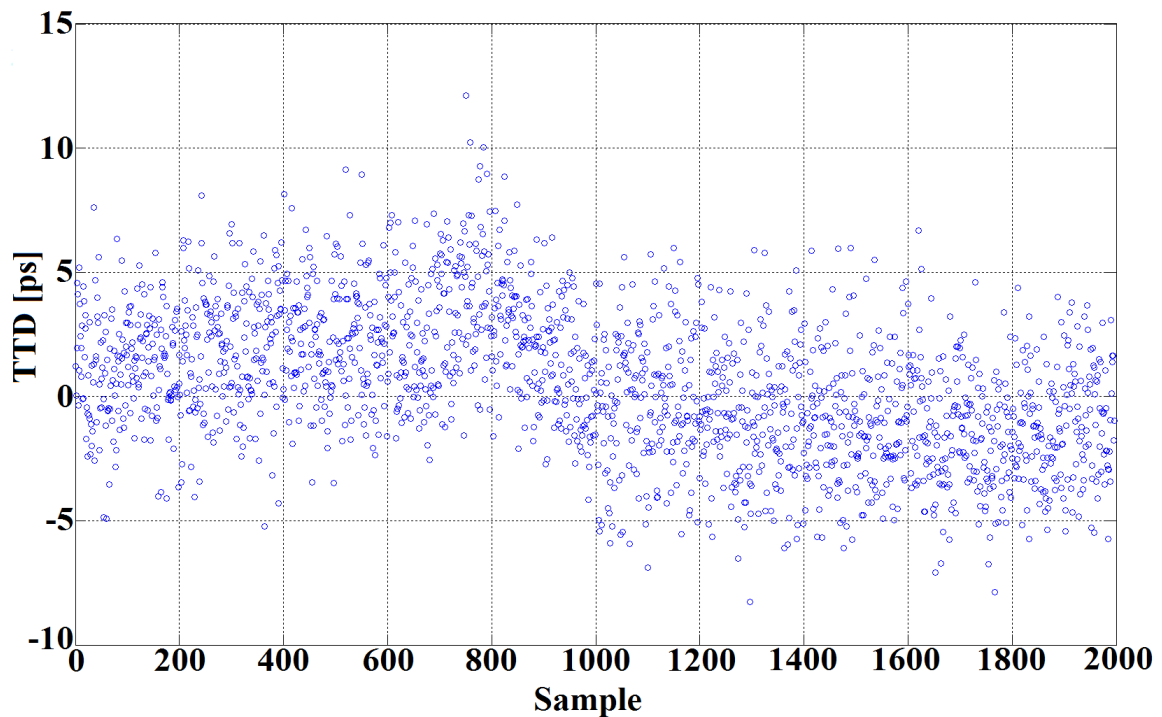


Fig. 7.10: TTD measurements performed at 60°C

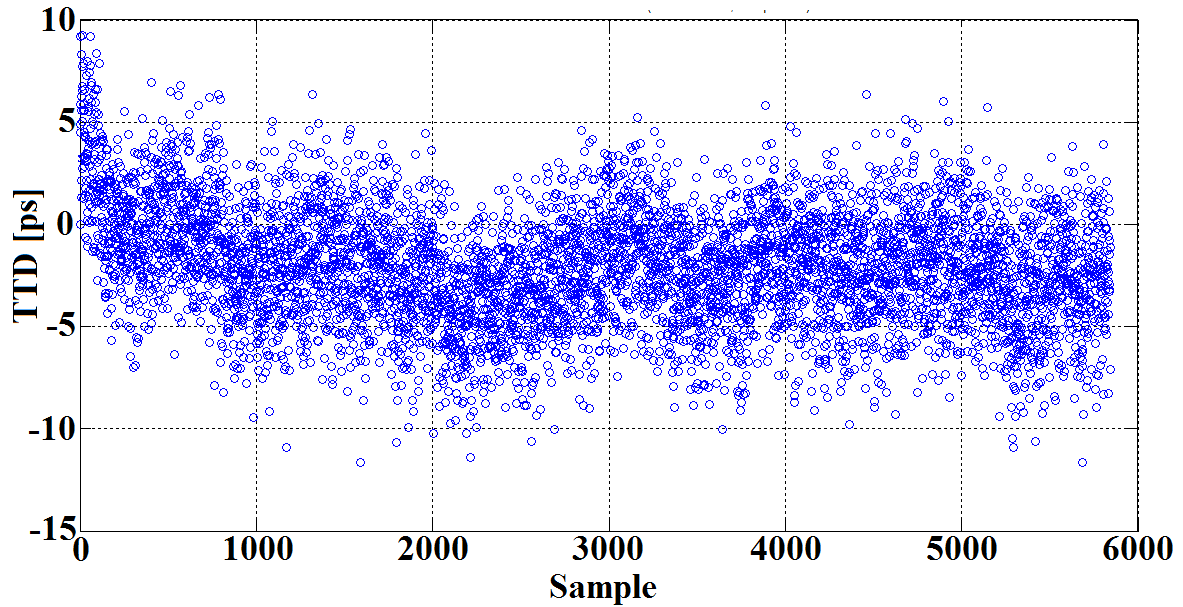


Fig. 7.11: TTD measurements performed at 80°C

7.6. Discussion

The transducers suffer from variations in their characteristic parameters such as static capacitance, electrical impedance, and resonance frequency that is temperature dependent, as demonstrated by the experimental measurements shown in Section 6.3. Furthermore, the exact value of the transducer working resonance frequency depends on the input impedance when the transducer acts as a transmitter and on the output impedance when the transducer acts as a receiver. On the other hand, under the same input or output impedance conditions the variation of the temperature changes the transducer resonance frequency as well. The validity of the proposed methodology is checked by evaluating the variation of the transducer's resonance frequencies and the driving frequency, which is used to adjust the TTD-offset with respect to the temperature changes (Figures 6.5 and 6.13). These results show that an increase in the temperature leads to a decrease in the resonance frequency of the transducer and the driving frequency at which the TTD-offset can be compensated. Moreover, the long-term stability of the driving frequency used to adjust the TTD-offset error has been experimentally proved at four different temperatures. As shown in Table 6.2, the variation of the driving frequency, which is used to compensate the TTD-offset, is less than 4 Hz at the same temperature of the medium around the transducers.

Chapter 8

Conclusion

The main goal of this thesis is to improve the performance accuracy of the ultrasonic transit time flow meters. This work also provides a detailed description of the theoretical development and the experimental validation of the ultrasonic system and develops a new water flow measurement approach that solves the TTD-jitter and TTD-offset problems raised by the ultrasonic flow meters. The thesis starts with a proposal for the analytic modeling of the piezoelectric transducer disk. This proposal was borrowed from damped driven harmonic oscillator theory. By investigating the amplitude and phase responses of the voltage across the resistive element of the transducer's electrical model, which represents the energy transferred to the water, it is found that the harmonic oscillator model is highly suitable to effectively capture the electrical behavior of the piezoelectric transducer disk, the most critical part of the ultrasonic water flow meter.

The numerical solution of the second order differential equation of damped harmonic forced system includes the transient or the homogeneous solution and the steady-state or the particular solution. This steady-state can be reached only by exciting the transducer for a sufficiently long time period. We have deduced through these solutions that the accuracy of the flow meter can be further improved if we rely on the particular solution instead of the homogeneous one. This steady-state part of the signal is characterized by a fixed amplitude, a phase shift, and a frequency that matches the driving frequency. Therefore, the TTD is measured as the phase difference between the received signals in both directions. Furthermore, the phase shifts on both transducer for the received signals are estimated in the steady-state parts of the signals using the least square sine-fitting, which filters out all the noise related to the signal digitization carried out by the two 14-bit ADCs.

The second development established through this work is the TTD-jitter reduction approach, which considerably enhances TTD-jitter performance. As it can be inferred from the experimental results, the standard deviation of the TTD-jitter is reduced drastically by using the sine-fitting technique. Furthermore, the system accuracy is carried out one step further by exploring two techniques, namely, employing low-noise amplifiers to improve the acquisition system dynamic range and using an adequate number of samples in a specific time interval (steady-state region).

Another achievement of this study is the extension of the TTD-jitter reduction technique to TTD-offset cancellation, which also degrades the ultrasonic flow meters. A novel approach to the problem has been developed to cancel the long-term zero flow TTD-offset drift caused by temperature variations. This approach is based on the principle that continuously adjusting the driving frequency nearby the resonance working area of the transducers reduces the zero-flow TTD-offset to zero. The TTD-offset dependence of the forced frequency finds a simple explanation in the theory of the oscillator: if the forced frequency is in the range between the respective resonance frequencies, a slight shift of the frequency produces an increase or a decrease in the amplitudes of the transmitted acoustic waves. Choosing a correct forced frequency according to the temperature of the medium can adjust the amplitude of the transmitted signals and compensate the TTD-offset. The robustness of the zero flow TTD-offset cancellation methodology is experimentally validated in harsh conditions, such as high temperatures (up to 80°C).

Bibliography

- [01] M. Sc. Yaoying Lin, “Signal processing and experimental technology in ultrasonic flow measurement”, Ph.D. dissertation, Duisburg Univ., Essen, 2004.
- [02] J. Yoder, “Ultrasonic flow meters in the energy measurement spotlight”, *Pipeline and Gas J.*, vol. 236, no. 7, pp. 20-28, Jul. 2009.
- [03] M. Kupnik, A. Schröder, and P. O’Leary, “Adaptive pulse repetition frequency technique for an ultrasonic transit-time gas flow meter for hot pulsating gases”, *IEEE. Sensor J.*, vol. 6, no. 4, pp. 906-615, Aug. 2006.
- [04] J. Berribi, “Self-diagnosis techniques and their applications to error reduction for ultrasonic flow measurements”, Ph.D. dissertation, Luleå Univ., Sweden, 2004.
- [05] J. Reyes, and A. Acevedo, “Simulation and experimental validation of a transit time in an ultrasonic gas flow meter using air”, in *Proc. conf. IEEE. ANDESCON*, Bogota, Colombia, Sep. 2010, pp. 1-6.
- [06] P. Lunde, M. Vestrheim, B. Reidar, S. Smorgrav, and A. K. Abrahamsen, “Reciprocity and its utilization in ultrasonic flow meters”, in *Proc. 23rd Int. North Sea Flow Measurement Workshop*, Tønsberg, Norway, Oct. 2005, pp. 18–21.
- [07] P. Lunde, M. Vestrheim, B. Reidar, S. Smorgrav, and A. K. Abrahamsen, “Reciprocal operation of ultrasonic flow meters: criteria and applications”, in *Proc. Conf. IEEE Ultrasonics Symp.*, New York, USA, Oct. 2007, pp. 381–386.
- [08] S. Ballantine, “Reciprocity in electromagnetic, mechanical, acoustical, and interconnected systems”, in *Proc. Inst. Radio Engrs.*, New Jersey, USA, vol. 17, no. 6, Jun. 1929, pp. 929-951.
- [09] W. R. MacLean, “Absolute measurement of sound without a primary standard”, *Acoust. Soc. Am. J.*, vol. 12, Jul. 1940, pp. 140-146.
- [10] L. L. Foldy, and H. Primakoff, “A general theory of passive linear electroacoustic transducers and the electroacoustic reciprocity theorem. I”, *Acoust. Soc. Am. J.*, vol. 17, Oct. 1945, pp. 109-120.

-
- [11] E. M. McMillan, "Violation of the reciprocity theorem in linear passive electromechanical systems", *Acoust. Soc. Am. J.*, vol. 18, Oct. 1946, pp. 344-347.
- [12] L. L. Foldy, and H. Primakoff, "A general theory of passive linear electroacoustic transducers and the electroacoustic reciprocity theorem. II", *Acoust. Soc. Am. J.*, vol. 19, Jan. 1947, pp. 50-58.
- [13] R. J. Bobber, "General reciprocity parameter", *Acoust. Soc. Am. J.*, vol. 39, no.4, Apr. 1966, pp. 680-687.
- [14] F. V. Hunt, "The analysis of transduction and its historical background", 2nd ed., Harvard Univ. Press, Acoust. Soc. Am., New York, 1982.
- [15] J. Hemp, "Improvements in or relating to ultrasonic flow meters", Patent UK2017914 A, 1979.
- [16] M. L. Sanderson, and J. Hemp, "Ultrasonic flow meters – a review of the state of the art", in *Proc. Conf. on advances in flow measurement techniques*, Warwick Univ., UK, Sep. 1981, pp. 157-178.
- [17] J. Borg, "On electronics for measurement systems", Ph.D. dissertation, Dept. Elect. Eng., Luleå Univ., Sweden, 2010.
- [18] J. Borg, J. Johansson, J. V. Deventer, and J. Delsing, "Reciprocal operation of ultrasonic transducers: experimental results", in *Proc. Conf. IEEE Ultrasonics Symp.*, New Jersey, USA, Oct. 2006, pp. 1013-1016.
- [19] Y. Bo, C. Li, and L. Yupin, "Forced oscillation to reduce zero flow error and thermal drift for non-reciprocal operating liquid ultrasonic flow meters", *Flow Meas. Instr. J.*, vol. 22, Aug. 2011, pp. 257–264.
- [20] F. M. Birleanu, "Design of RPA representation spaces for the analysis of transient signals", Ph.D. dissertation, Grenoble Univ., France, 2006.
- [21] M. L. Sanderson, and H. Yeung, "Guidelines for the use of ultrasonic non-invasive metering techniques", *Flow Meas. Instr. J.*, vol. 13, Aug. 2002, pp. 125–142.
- [22] W. D. Barber, J. W. Eberhard, and S. G. Karr, "A New Time Domain Technique for Velocity Measurements Using Doppler Ultrasound", *IEEE. Trans. Biomedical Eng.*, vol. BME-32, no. 3, pp. 213-229, Mar. 1985.
- [23] Y. Bo, and C. Li, "High-speed and precise measurement for ultrasonic liquid flow metering based on a single FPGA", in *Proc. Conf. IEEE Instr. Meas. Techno.*, Singapore, May 2009. pp. 309–312.

-
- [24] N. C. Temperley, "Optimisation of an Ultrasonic Flow Meter Based on Experimental and Numerical Investigation of Flow and Ultrasound Propagation", Ph.D. dissertation, New South Wales Univ., Australia, 2002.
- [25] H. D. Al-Budairi, "Design and analysis of ultrasonic horns operating in longitudinal and torsional vibration", Ph.D. dissertation, Glasgow Univ., Scotland, UK, 2012.
- [26] C. Rosen, B. Hiremath, and R. Newnham, "Piezoelectricity", American Institute of Physics, New York, USA, 1992.
- [27] "IEEE Standard on Piezoelectricity", The Institute of Electrical and Electronics Engineers, Inc., New York, USA, 1988.
- [28] P. Acevedo, and I. S. Domínguez, "Simulation of an Ultrasonic Transducer for Medical Applications Using the Finite Element Method", *Mater. Sci. Eng. J.*, vol. 7, Aug. 2015, pp. 293-297.
- [29] J. Kocbach, "Finite Element Modeling of Ultrasonic Piezoelectric Transducers", Ph.D. dissertation, Bergan Univ., Norway, 2000.
- [30] D. R. Franca, C. K. Jen, and Y. Ono, "Contrapropagating Ultrasonic Flow meter Using Clad Buffer Rods for High Temperature measurement", *Dynamic System Measurement and Control. J.*, vol. 133, no. 1, Jan. 2011, pp. 7-13.
- [31] G. Kossoff, "Effects of Backing and Matching on the Performance of Piezoelectric Ceramic Transducers", *IEEE Trans. Sonics and Ultrasonic*, vol. 13, no. 1, Mar. 1966, pp. 20-30.
- [32] M. Goldfarb, and N. Celanovic, "Modeling Piezoelectric Stack Actuators for Control of Micromanipulation", *IEEE Control Systems J.*, vol. 17, no. 3, Jun. 1997, pp. 69-79.
- [33] F. Wein, "Topology Optimization of Smart Piezoelectric Transducers", Ph.D. dissertation, Erlangen-Nürnberg Univ., Germany, 2011.
- [34] J. David, and N. Cheeke, "Fundamentals and Applications of Ultrasonic Waves", CRC Press LCC, Montreal, Qc, Canada, 2002, ch. 2, pp. 14-38.
- [35] J. M. Friedt, and É. Carry, "Introduction to the quartz tuning fork", *Am. Phys. J.*, vol. 75, No. 5, May 2007, pp. 415-422.
- [36] J. Ramon, G. Hernandez, and J. Bleahey, "Low-Cost, Wideband Ultrasonic Transmitter and Receiver for Array Signal Processing Applications", *IEEE Sensors J.*, vol. 11, no. 5, May 2011, pp. 1284-1292.

- [37] E. Storheim, P. Lunde, and M. Vertrheim, "Diffraction Correction in Ultrasonic Fields for Measurements of Sound Velocity in Gas. Conventional and Alternative Methods", in *Proc. 34th Scandinavian Symposium on Physical Acoustic*, Jan. 30-Feb. 2, 2011, pp. 1–27.
- [38] W. C. Zarnstorff, C. A. Castillo, and C. W. Crumpton, "A phase-shift ultrasonic flow meter", *IRE Trans. Bio-Medical Electronics*, vol. 9, no. 2, Jan. 1962, pp. 199–203.
- [39] F. C. Alegria", Bias of amplitude estimation using three-parameter sine fitting in the presence of additive noise", *Meas. J.*, vol. 42, Jun. 2009, pp. 748-756.
- [40] J. Šaligaa, I. Kollár, L. Michaeli, J. Bušaa, J. Liptáka, and T. Virosztek, "A comparison of least squares and maximum likelihood methods using sine fitting in ADC testing", *Meas. J.*, vol. 46, Dec. 2011, pp. 4362–4368.
- [41] V. Dumbrava, and L. Svilainis, "The Automated Complex Impedance Measurement System", *Electron. Elec. Eng. J.*, vol. 76, no. 4, Mar. 2007, pp. 59-62.
- [42] F. d. Silva, P. M. Ramos, and A. C. Serra, "A new four parameter sine fitting technique", *Meas. J.*, vol. 35, Mar. 2004, pp. 131–137.
- [43] P. M. Ramos, F. D. Silva, and A. C. Serra, "Improving sine-fitting algorithms for amplitude and phase measurements", in *Proc. XVII IMEKO World Congress*, Dubrovnik, Croatia, Jun. 22–27, 2003, pp. 614–619.
- [44] P. M. Ramos, F. d. Silva, and A. Cruz Serra, "Low frequency impedance measurement using sine-fitting", *Meas. J.*, vol. 35, Jan. 2004, pp. 89–96.
- [45] P. M. Ramos, and A. C. Serra, "A new sine-fitting algorithm for accurate amplitude and phase measurements in two channel acquisition systems", *Meas. J.*, vol. 41, Feb. 2008, pp. 135–143.
- [46] P. A. Picot, "Blood Flow Visualization and Flow Rate Estimation with Colour Doppler Ultrasound", Ph.D. dissertation, Western Ontario Univ., Canada, 1997.
- [47] H. Øberg, "Ultrasound sensor for biomedical applications", M.S. thesis, Tromsø Univ., Norway, 2011.
- [48] P. Lunde, K. E. Frøysa, and M. Vertrheim, "GERG Project on Ultrasonic Gas Flow Meters, Phase II", GERG Technical Monograph, Norway, 2000.
- [49] *Analog Devices Data sheet*, Analog Devices, Inc., USA, 2011-2015.
- [50] V. Petkus, A. Ragauskas, and P. Borodicas, "Temperature dependence of a piezoceramic transducer electric impedance", *ULTRAGARSAS J.*, vol. 56, no. 3, 2005, pp. 22–25.

- [51] P. Fletcher-Haynes, "Method and apparatus for correcting temperature variations in ultrasonic flow meters", Patent US5831175, 1998.
- [52] R. J. Hazelden, and K. P. F. Smith, "Improvements in fluid monitoring", Patent WO2004070358, 2004.